

**HYBRID LIGHT EMITTING DIODES  
BASED ON SOLUTION PROCESSED  
POLYMERS, COLLOIDAL QUANTUM DOTS,  
AND COLLOIDAL METAL NANOPARTICLES**

by

Xin Ma

A dissertation submitted to the Faculty of the University of Delaware in partial fulfillment of the requirements for the degree of Doctor of Philosophy in Electrical and Computer Engineering

Spring 2014

© 2014 Xin Ma  
All Rights Reserved

UMI Number: 3631195

All rights reserved

INFORMATION TO ALL USERS

The quality of this reproduction is dependent upon the quality of the copy submitted.

In the unlikely event that the author did not send a complete manuscript and there are missing pages, these will be noted. Also, if material had to be removed, a note will indicate the deletion.



UMI 3631195

Published by ProQuest LLC (2014). Copyright in the Dissertation held by the Author.

Microform Edition © ProQuest LLC.

All rights reserved. This work is protected against unauthorized copying under Title 17, United States Code



ProQuest LLC.  
789 East Eisenhower Parkway  
P.O. Box 1346  
Ann Arbor, MI 48106 - 1346

**HYBRID LIGHT EMITTING DIODES  
BASED ON SOLUTION PROCESSED  
POLYMERS, COLLOIDAL QUANTUM DOTS,  
AND COLLOIDAL METAL NANOPARTICLES**

by

Xin Ma

Approved: \_\_\_\_\_  
Kenneth E. Barner, Ph.D.  
Chair of the Department of Electrical and Computer Engineering

Approved: \_\_\_\_\_  
Babatunde A. Ogunnaike, Ph.D.  
Dean of the College of Engineering

Approved: \_\_\_\_\_  
James G. Richards, Ph.D.  
Vice Provost for Graduate and Professional Education

I certify that I have read this dissertation and that in my opinion it meets the academic and professional standard required by the University as a dissertation for the degree of Doctor of Philosophy.

Signed:

---

Sylvain G. Cloutier, Ph.D.  
Professor in charge of dissertation

I certify that I have read this dissertation and that in my opinion it meets the academic and professional standard required by the University as a dissertation for the degree of Doctor of Philosophy.

Signed:

---

James Kolodzey, Ph.D.  
Member of dissertation committee

I certify that I have read this dissertation and that in my opinion it meets the academic and professional standard required by the University as a dissertation for the degree of Doctor of Philosophy.

Signed:

---

Robert Opila, Ph.D.  
Member of dissertation committee

I certify that I have read this dissertation and that in my opinion it meets the academic and professional standard required by the University as a dissertation for the degree of Doctor of Philosophy.

Signed:

---

Juejun Hu, Ph.D.  
Member of dissertation committee

## ACKNOWLEDGMENTS

Firstly, I would like to thank my advisor Professor Sylvain G. Cloutier for his support, advice and guidance over the past six year on my Ph.D. study. It would simply be impossible for me to complete this thesis without his help.

I would like to thank my thesis committee members Professor James Kolodzey, Professor Robert Opila and Professor Juejun Hu for sharing your valuable time and opinion with me from my thesis proposal to its finishing.

My thanks also go to Professor Doty and Chelsea Haughn in Material Science and Engineering Department. Collaborating with you was a real pleasant and priceless experience. Your time and valuable discussion is the key factor that makes chapter 6 of this thesis possible.

I would also like to thank Dr. Ruiying Hao and Dr. Xuesong Lu for their help and inspiration; Dr. Tim Creazzo and Dr. Elton Marchena for their time helping me get familiar with the cleanroom equipment and sharing with me your near infrared imaging setup; Dr. Chris Kerestes, Kevin Shreve, Dr. Sangcheol Kim and Dr. Yi Wang for their help on cleanroom equipment and maintenance; Dr. Fan Xu for his collaboration and quantum dot synthesis; Jaime Benavides, Dr. Latha Nataraj and Luis Felipe Gerlein for sharing the time in the lab and creating a relax working environment.

In the end, I want to give my special thanks to my family: my grandparents and parents. Thank them for allowing me to leave you for so long to pursuit and fulfill my goals.

## TABLE OF CONTENTS

LIST OF TABLES .....	viii
LIST OF FIGURES .....	ix
ABSTRACT .....	xiv
Chapter	
1 INTRODUCTION .....	1
1.1 Development of Semiconductor LEDs.....	1
1.2 Conductive Fluorescent Polymer Materials .....	4
1.3 Colloidal Quantum Dot .....	10
1.4 LEDs Made from Organic, Quantum Dots and Hybrid Materials .....	19
1.5 Surface Plasmon-Enhanced LEDs.....	28
1.6 Structure of This Thesis.....	30
REFERENCES .....	33
2 EXPERIMENTAL METHOD .....	43
2.1 Materials Used in The Thesis .....	43
2.1.1 Polyfluorene Polymer .....	43
2.1.2 Colloidal PbS Nanoparticles.....	45
2.1.3 Silver Nanoparticle Synthesis.....	49
2.2 Device Structure .....	51
2.2.1 General Device Structure and Design Requirements .....	51
2.2.2 Device Layout .....	54
2.3 Device Fabrication Methods Used in This Thesis.....	54
2.3.1 ITO Deposition and Patterning.....	54
2.3.2 Spin-Coating.....	56
2.3.3 E-beam Evaporation of Al Cathode .....	57
2.4 Material and Device Characterization Method.....	59

2.4.1	UV-Visible Absorption Spectroscopy .....	59
2.4.2	Steady-State Photoluminescence and Electroluminescence Spectroscopy.....	61
2.4.3	Time-Resolved Photoluminescence Measurements .....	63
2.4.4	Transmission Electron Microscopy.....	64
2.4.5	Scanning Electron Microscopy.....	64
2.4.6	Atomic Force Microscopy .....	65
2.4.7	Film Thickness Measurements .....	67
2.4.8	Device PIV Characterization.....	67
2.4.9	Mobility Measurements .....	70
2.4.9.1	Time-of-flight .....	71
2.4.9.2	Charge extraction by linearly increasing voltage (CELIV).....	74
REFERENCES .....		76
3	SOLVENT AND BAKING EFFECT ON POLYMER MORPHOLOGY AND PLED PERFORMANCE.....	80
3.1	Solvent and Baking Effect on Phase Separation in Polymer Blend .....	80
3.2	Solvent and Baking Effect on Polymer Crystalline Structure in Thin Film .....	85
3.3	Conclusion.....	95
REFERENCES .....		96
4	QUANTUM DOT LIGAND EXCHANGE EFFECT IN POLYMER AND QUANTUM DOT HYBRID STRUCTURE.....	98
4.1	Introduction .....	98
4.2	Absorption and Dielectric Constant Change on Cross-Linked Quantum Dot Thin Film.....	100
4.2.1	Experiment .....	100
4.2.2	Result and Discussion.....	100
4.3	Quantum Dot Cross-Linked On Polymer .....	106
4.4	Conclusion.....	114
REFERENCES .....		115
5	HIGH PERFORMANCE HYBRID NEAR-INFRARED LEDS USING PBS COLLOIDAL NANOCRYSTALS .....	118

5.1	Quantum Dot LED Structure Review.....	118
5.2	Polymer/Quantum Dot Blend Hybrid Structure and Its Limitations.....	120
5.3	Bi-Layer Polymser/Quantum Dot Hybrid LED with Ligand Exchange Quantum Dot Solid Thin Films.....	125
5.3.1	Introduction.....	125
5.3.2	Material and Methods.....	128
5.3.3	Hybrid Near-Infrared LED Structure With BDT Linker.....	131
5.3.4	EDT Vs. BDT Cross-Link for LED Application.....	136
5.4	Conclusion.....	143
	REFERENCES.....	145
6	HIGH POLYER-LEDS ENHANCEMENT BY EXCITON-PLASMON COUPLING USING ENCAPSULATED METALLIC NANOPARTICLES.....	149
6.1	Introduction.....	149
6.2	Experimental Method and Device Structure.....	152
6.3	Silver Nanoparticle-Enhanced PLED.....	154
6.4	Conclusion.....	164
	REFERENCES.....	166
7	CONCLUSIONS AND FUTURE PROSPECTS.....	171
	REFERENCES.....	177
	Appendix	
A	CONTRIBUTIONS ASSOCIATED WITH THIS THESIS.....	180
A.1	Journal Publications.....	180
A.2	Conference Publications.....	181

## LIST OF TABLES

Table 1-1:	Comparison of luminous power efficacies for light sources. ....	4
Table 1-2:	Exciton bulk Bohr diameter and bulk material band gap for typical colloidal quantum dot materials. [39].....	14
Table 4-1:	Parameters used in the EMA model. ....	105
Table 5-1:	Comparison of the conductivity, hole- and electron mobilities for EDT- and BDT- treated nanocrystalline films .....	142

## LIST OF FIGURES

Figure 1-1: Description of conjugation in organic polymer.....	6
Figure 1-2: Exciton spatial distribution for Frenkel exciton in organic material and Wannier-Mott exciton in inorganic semiconductor material. ....	9
Figure 1-3: Quantum dot synthesis schema using the flask method. Right panel shows the size growth with increasing synthesis temperature. ....	13
Figure 1-4: Density of states for nano-scale confined materials.....	15
Figure 1-5: Multilayer device structure including all possible functional layers and the typical energy band alignment to achieve the function of each layer used in this structure.....	21
Figure 1-6: Lambert distribution.....	23
Figure 1-7: Conventional hybrid quantum dot device configuration.....	27
Figure 1-8: Four possible device configurations using cross-linked bulk quantum dot layers as the functional material.....	28
Figure 2-1: Polymer molecular structure.....	45
Figure 2-2: Quantum dot TEM and tunable fluorescence spectrum.....	48
Figure 2-3: Organic light emitting device structure.....	52
Figure 2-4: Diagram of the device layout.....	54
Figure 2-5: Denton Vacuum Discovery 18 Sputtering Deposition System.....	55
Figure 2-6: Sketch of spin-coating process.....	57
Figure 2-7: Diagram of e-beam evaporator system.....	59
Figure 2-8: Diffused reflectance absorption measurement setup.....	61
Figure 2-9: Power-current-voltage measurement setup configuration.....	68
Figure 2-10: Standard luminosity function [18].....	69

Figure 2-11: Time-of-flight setup configuration .....	72
Figure 2-12: Transit current profile in time of flight measuremet. ....	73
Figure 2-13: CELIV applied voltage and the correspondingly measured current. ....	75
Figure 3-1: Blended TFB-F8BT polyfluorene-based type-II heterostructures using different solvents. ....	83
Figure 3-2: Bulk heterojunction polymer LED demonstration. ....	84
Figure 3-3: Comparison of the polymer blend film morphology before and after annealing in air at 100 °C measured under AFM. ....	85
Figure 3.4: Molecular structures of the two solvents investigated in this thesis: toluene and chloroform .....	86
Figure 3.5: Polymer blend LED device configuration. ....	87
Figure 3-6: Normalized PL intensity for polymer in solution and solid state thin film made by spin coating, no baking was applied [15]. ....	88
Figure 3-7: Polymer chain morphology in different solvent. ....	89
Figure 3-8: Device performance comparison under different fabrication conditions. ....	90
Figure 3-9: C-AFM date for the four samples in the experiment. ....	91
Figure 3-10: Output power from devices made from the two solvents before and after baking respectively [15]. ....	92
Figure 3-11: Confocal fluorescent microscopy images for the four samples in the experiment. ....	93
Figure 3-12: Conductive AFM measurements on polymer blend thin films fabricated from toluene solution. ....	94
Figure 3-13: Confocal fluorescence of polymer blend thin film fabricated from toluene solution before and after baking. ....	95
Figure 4-1: Schematic demonstration of ligand exchange process. ....	99
Figure 4-2: Quantum dot size determination through absorption peak. ....	101

Figure 4-3: TEM image of quantum dot capped with (a) Oleic Acid, (b) BDT and (c) EDT [11].	101
Figure 4-4: AFM image of as deposited OA capped quantum dot thin film (a), BDT treated single-layer quantum dot thin film (b) and BDT treated quantum dot thin film after 3 circle of layer-by-layer deposition.	102
Figure 4-5: Cross-linked quantum dot thin film morphology.	102
Figure 4-6: Measured and effective medium approximation (EMA) simulated absorption spectra for oleic acid (OA), ethanedithiol (EDT) and benzenedithiol (BDT)-capped quantum dot films.	104
Figure 4-7: Hybrid bi-layer device schematics and the molecular structure of the TFB polymer and oleic acid, ethanedithiol (EDT) and benzenedithiol (BDT) quantum dot ligands.	106
Figure 4-8: Absorption (—) and fluorescence (---) of the hybrid polymer-nanocrystal structure and for stand-alone polymer and quantum dot films.	107
Figure 4-9: Fluorescence of 30 nm-thick TFB polymer films with and without exposure to acetonitrile, hexane, EDT and freshly-prepared BDT solutions.	109
Figure 4-10: Absorption spectra for oleic acid (OA), ethanedithiol (EDT) and benzenedithiol (BDT)-treated quantum dots films by themselves and atop a TFB polymer film.	110
Figure 4-11: Polymer and quantum dot fluorescence under 405nm excitation (a) and 532nm excitation (b) for pristine oleic acid (OA)-capped samples.	112
Figure 4-12: Polymer and quantum dot fluorescence for EDT treated samples under 405nm excitation (a) and 532nm excitation (b), and for BDT treated sample under 405nm excitation (c) and 532nm excitation (d).	113
Figure 5-1: Device configurations in previous near-IR quantum dot LEDs.	119
Figure 5-2: (a) Energy diagram for the materials used in the blend hybrid multilayered LED, (b) the I-V characteristics of blend hybrid device, and (c) the device electroluminescence [9].	122

Figure 5-3: The consequences of quantum-dot incorporation on blended polyfluorene-based film structures.....	123
Figure 5-4: Nanoparticle incorporation reduces polymer chain arrangement in electron-spun nanofibers. ....	125
Figure 5-5: Multi-layered polymer/quantum dot hybrid device structure.....	128
Figure 5-6: TEM images of quantum dots with different sizes.....	131
Figure 5-7: Current-voltage characteristics for the hybrid multilayered LED using a BDT-treated nanocrystalline film and for a TFB polymer-only control device. [26].....	132
Figure 5-8: Electron and hole transporting layer optimization in hybrid device structures. ....	134
Figure 5-9: Hybrid near-IR device performance demonstration.....	136
Figure 5-10: Properties comparison for devices with different quantum dots ligands. PIV characteristics for un-treated, BDT- and EDT- treated nanocrystalline device. ....	138
Figure 5-11: CELIV transient currents measurement results. EDT- (a) and BDT- (b) treated films. ....	139
Figure 5-12: TOF transient current measurements for EDT- and BDT-treated films.....	141
Figure 5-13: Summary of electronic properties of EDT and BDT cross-linked quantum dot thin films. ....	142
Figure 6-1: Surface plasmon-enhanced polymer LED structure.....	155
Figure 6-2: Diffused reflectance absorption of colloidal NPs in the device structure and photoluminescence of the F8BT polymer. ....	156
Figure 6-3: Surface plasmon-enhanced polymer LED and control group devices performances comparison.....	158
Figure 6-4: Ag nanoparticle density optimization for SP enhanced PLED. ....	160
Figure 6-5: AFM images and surface roughness information for Ag nanoparticles spin-coated on polymer film using 0, 1, 3, 5 and 7 mg/ml nanoparticle solutions. [34].....	162

Figure 6-6: (a) Luminance intensity comparison for normal PLED, bilayer Ag NPs PLED and blend Ag NPs PLED. (b) TRPL comparison between a pristine 90nm F8BT film and the same polymer film with monolayer of Ag NPs on top. (c) Demonstration of the SP enhancement mechanism. [33] ..... 162

## ABSTRACT

This dissertation focuses on solution-processed light-emitting devices based on polymer, polymer/PbS quantum dot, and polymer/silver nanoparticle hybrid materials. Solution based materials and organic/inorganic hybrid light emitting diodes attracted significant interest recently due to many of their advantages over conventional light emitting diodes (LEDs) including low fabrication cost, flexible, high substrate compatibility, as well as tunable emission wavelength of the quantum dot materials. However, the application of these novel solution processed materials based devices is still limited due to their low performances. Material properties and fabrication parameters need to be carefully examined and understood for further device improvement.

This thesis first investigates the impact of solvent property and evaporation rate on the polymer molecular chain morphology and packaging in device structures. Solvent is a key component to make the active material solution for spin coating fabrication process. Their impacts are observed and examined on both polymer blend system and mono-polymer device. Secondly, PbS colloidal quantum dot are introduced to form hybrid device with polymer and to migrate the device emission into near-IR range. As we show, the dithiol molecules used to cross-link quantum dots determine the optical and electrical property of the resulting thin films. By choosing a proper ligand for quantum dot ligand exchange, a high performance polymer/quantum dot hybrid LED is fabricated. In the end, the interaction of polymer exciton with

surface plasmon mode in colloidal silver nanoparticles and the use of this effect to enhance solution processed LEDs' performances are investigated.

# Chapter 1

## INTRODUCTION

### 1.1 Development of Semiconductor LEDs

In modern society, light sources are one of the key electronic components used in almost every aspect of human life, from common daily lighting to modern high-technology digital devices. Their application includes but is not limited to general lighting, large screen TV and displays, remote control, telecommunications, portable electrical devices and sensors & imaging technologies. Recently, along the fast development of personal portable digital devices and the increasing demand for low power-consuming devices, light source innovation has attracted more and more research and industry development interests. In today's market for light sources, fluorescent lamps have replaced incandescent light bulbs for general lighting, and have also replaced CRTs (cathode ray tubes) for displays mainly due to their advantages in higher efficiencies, lower surface temperatures and more compact footprints. Still, fluorescent lamps also suffer from several drawbacks like low color temperatures, low color saturations and large bulb sizes, which have limited further development of modern lighting and display technology which requires low power consumption, light weight and ultrathin configurations.

Along with the discovery and understanding of semiconductor materials and their properties, a new kind of light source – the semiconductor light emitting diode (LED) was first reported in 1920s [1]. The semiconductor-based LED is a category of light source working on the mechanism of electron and hole recombination in

semiconductor material. In this process, the electron energy is directly released through the emission of photons; the color of the light source depending on the band-gap of the semiconductor material used in the device. To facilitate carrier injection and confine recombination regions, LEDs usually rely on n-type and p-type semiconductors forming a depletion junction at the interface. During device operation, large densities of electrons are injected from the cathode into the n-type semiconductor while, on the opposite side, large densities of holes are injected from the anode into p-type semiconductor. Electrons and holes meet at the junction's interface where they recombine and emit light. Compared with traditional incandescent light bulbs and fluorescent light sources, semiconductor LEDs have the lowest energy consumptions, smallest sizes, and fastest switching speeds. Their efficiency has overcome fluorescent bulb (90lm/W), and meanwhile, their lifetimes are significantly longer than incandescent and fluorescent bulbs. As the price of semiconductor LEDs was reduced through mass manufacturing, they became widely used as indicators, remote controls (for infrared LEDs), and backlighting in displays, gradually replacing traditional light source in the market. But the high cost and low throughput of epitaxial growth process of inorganic semiconductor LEDs manufacturing is the main drawback that holds their progress in the commercial market for low cost, large area device and display applications. Moreover, the inorganic semiconductor light sources based on III-VI semiconductors are also difficult to integrate into silicon CMOS platforms because of the high lattice mismatch, which can introduce fatal defects into crystalline semiconductor-based LEDs.

In the last decades, novel conductive and highly-fluorescent organic materials and inorganic quantum dot innovation have pushed semiconductor LED into a completely new age. Small organic molecules, conjugated polymers and colloidal quantum dot materials can not only significantly lower the LED fabrication costs, but also offer many advantages including wider color range, ink-jet printability and flexible substrate compatibility, many of which are out-of-reach for crystalline semiconductor-based LED technologies.

The first organic LEDs (OLEDs) fabricated in 1987 used an aromatic small molecule Tris(8-hydroxyquinolino) aluminium (Alq<sub>3</sub>), as the active material to achieve green light emission [2]. In OLEDs, small molecules are generally deposited by thermal evaporation. Compared with solution-based processes, thermal deposition has the advantage of accurate film thickness control and complex multi-layer structure constructability, which are essential to achieve high quantum efficiencies[2,3]. However, this method still requires high-vacuum systems and high-power evaporation procedures for device fabrication. Currently, carefully-designed multilayer structures and doping of phosphorescent materials, which convert non-radiative triplet-states into radiative singlet-states, have pushed OLEDs up to efficiencies as high as 100 lm/W [4], which can compete with many commercial inorganic LEDs and fluorescent bulbs. Table 1-1 summarized the power efficiency of common light sources. Compared with inorganic semiconductor LEDs, OLEDs offer lower fabrication costs and easy adaptability on amorphous silicon TFT backplanes [5]. It is considered to hold great promises for producing ultrathin, ultra lightweight, better color saturation and more efficient displays to replace current LCD (liquid crystal display) technologies for large area screens.

Table 1-1: Comparison of luminous power efficacies for light sources.

Light sources	Incandescent bulb	Fluorescent bulb	Cool White LED	Warm White LED	Organic LED	Polymer LED
Power efficiency (lm/W)	14~17 [6]	50~70 [6]	60~92 [6]	27-54 [6]	70~131 [6]	7.8 ~20 [7,8]

The LCDs technology works on the principle of light polarization and liquid crystal molecular rotation under electrical field. The liquid crystal cell is a passive structure which controls light intensity by controlling the thin film transparency. The light source is a white fluorescent bulb placed on the back to light up the display panel, and the RGB color are generated by placing RGB color filters on each pixel. Therefore, a big portion of the light is wasted by the linear polarizers, the liquid crystal absorption as well as the color filter, resulting in significantly lower efficiencies for LCDs. The two polarizers also reduce the viewing angle of the displays, limiting their application for large TVs and displays for multi-person usage. Meanwhile, the image contrast is low due to the incomplete blocking of light through the liquid crystal layer. The above mentioned limitations of LCDs can be very well solved by OLEDs, in which each pixel emits one color of light individually. Samsung, Sony and LG have successively launched their OLED-based TV and displays into commercial market [9].

## 1.2 Conductive Fluorescent Polymer Materials

Shortly after the first report of diode OLED based on small molecules, highly-conductive and fluorescent polymers soon joined the OLED materials family [10]. As small molecule materials, polymer conductivity is based on the electron wave function delocalization caused by p-orbital conjugation as in Figure 1-1(a). But unlike small molecules having low solubility in solvents, long polymer chains with different side

groups can dissolve very well in solvents so that thin films can be fabricated from their solution via spin-coating or ink-jet printing methods. Solution deposition techniques meet industrial demands for low-cost and large area processing. It also enables ink-jet printing as a low-cost patterning method which surpasses any other complicated and costly patterning process such as lithography and shadow mask. The possibilities of cross-linking different monomers to form copolymers, changing their side chains or forming polymer networks allows great tailoring on emission wavelength, material electrical property and mechanical property.

The essential structure of conductive polymer is a continuous series of double bonds formed by the half-filled p-orbital of carbon atoms. If more than one bonding states along the chain are considered together, molecular orbital will form due to the coupling between individual electron states. The electron in p-orbital fills half of the bonding molecular state, leaving the other half of anti-bonding molecular state empty. Figure 1-1 (b) schematically demonstrates these states. The gap between highest occupied molecular orbital (HOMO) and lowest unoccupied molecular orbital (LUMO) in Figure 1-1(b) determines the optical and electrical property of the conductive polymer, analogous to band gap in an inorganic semiconductor. Besides a linear chain, the other form of p-orbital conjugation is aromatic rings as shown in Figure 1-1(c). Both structures offer polymers with good conductive properties. Meanwhile, aromatic rings-formed polymers have weaker chain distortion between molecular HOMO and LUMO states, offering efficient electron transition between HOMO and LUMO. As such, it often has a higher fluorescence efficiency compared to linear chain-conjugated polymers [11]. For example the non-optimally active polyacetylene, through replacing a double bond by an aromatic ring in the backbone

unit cell, switches into Poly(p-phenylene vinylene) which has a fluorescent quantum yield of 20% ~50%. [12,13]

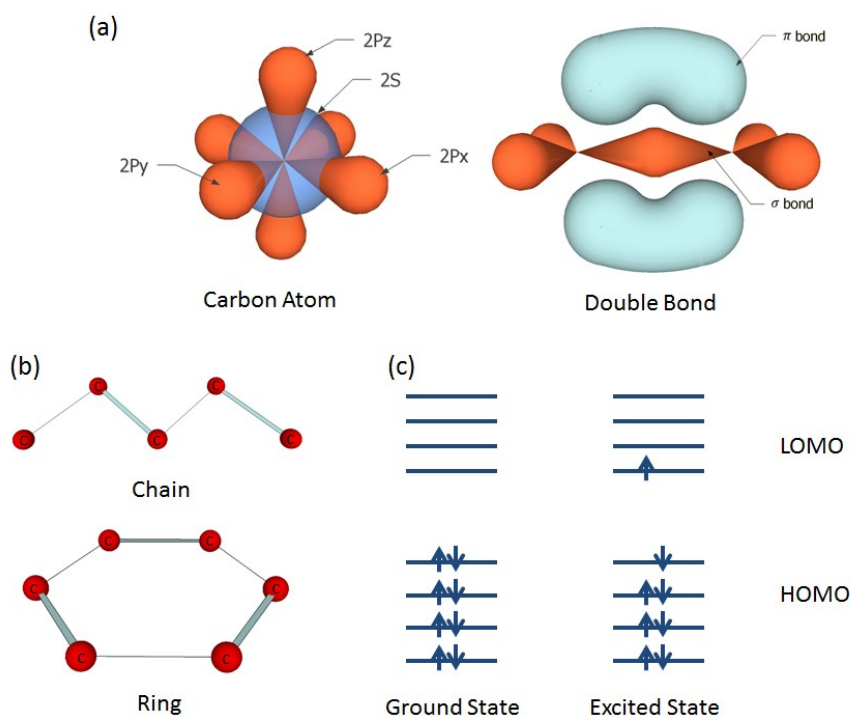


Figure 1-1: Description of conjugation in organic polymer. (a) Electron orbitals for a single carbon atom and a double bond between two carbon atoms. (b) Conjugated carbon chain and ring structure that afford electron transport (c) Ground state and excited state of molecular orbital energy states.

In polymer chains, the half-filled neutral dangling bond is highly reactive. If a dangling bond accepts an electron to pair the origin electron, it results in a negative charge in the segment of the polymer. Conversely, if the original electron is removed from the polymer chain, it forms a hole. These charges can diffuse along the polymer backbone or jump from one chain to another, forming current in polymer thin films.

When an electron and hole meet each other, they form an exciton – an elementary energy state of electron and hole bonded by electrostatic Coulomb force. Generally, the exciton binding energy in polymer is much stronger than in inorganic material due to the associated chain distortion to separate electron and hole pairs in polymer segment [14]. In polymer material, once an exciton is formed, it has greater chance to remain as a bonded entity instead of being separated as charged carriers again. Therefore, the strong bond of electron and hole makes fluorescent polymers more suitable for light emitting devices instead of photovoltaic devices. Excitons in polymers can be generated either by absorbing photons with energy greater than the HOMO/LUMO gap (photon excitation) or by injected carrier from metal electrode (electron excitation). Four possible exciton decay pathways can exist: (1) radiative decay to emit photon which is the source of photoluminescence and electroluminescence, (2) non-radiatively decay with energy loss as heat, (3) dissociation to release free mobile electrons and holes in the polymer, which is the mechanism for photovoltaic devices, (4) transfer of energy non-radiatively to another organic or inorganic material close by. To achieve highly-efficient electroluminescence devices, process (1) should be maximized during structure design and materials' choices. In contrast, process (3) would be favorable for photovoltaic devices.

While there are many similarities between electron and hole properties in polymer and inorganic materials and HOMO/LUMO levels can often be considered equivalent to the valence band maxima and conduction band minima in solid state physics, organic and inorganic materials demonstrate significantly different carrier and exciton transport properties as well as different material mechanical strength due to

different bonding states in the material's matrix. For polymers, the charged carriers are more localized that they only interact with the nearest repeat units of the polymer chain [15]. This weak interaction between conductive states cannot form a real energy band as in inorganic periodical lattice structures, consequently causing the low carrier mobilities observed in polymer materials. Meanwhile, disorder of HOMO and LUMO levels in polymer films also impedes electron and hole hopping between molecules. The lower energy states act as local traps for carriers, further lowering carrier mobilities in polymer materials. For exciton states in polymers, their binding energy is higher than in inorganic materials due to the chain distortion associated with exciton formation and the lower electron screening effect in polymers. Excitons are normally localized on the scale of a single monomer of polymer. Such excitons with strong bonding energy on the order of 0.1 to 1eV are referred to as Frenkel excitons [16]. In contrast, the large dielectric constants in inorganic materials (electron screen effect) reduce Coulomb interactions, resulting in exciton bonding energies on the order of 0.01eV. This type of exciton is referred to as a Wannier-Mott exciton. Figure 1-2 schematically demonstrates the differences between Frenkel and Wannier-Mott excitons. Finally, from the material's mechanical properties point of view, the weak van der Waals bonds between polymer chains also causes a soft and flexible texture of polymer thin films in contrast with their rigid inorganic counterparts, offering them high compatibility with different kinds of substrates such as silicon TFT backplanes and even flexible plastic substrates.

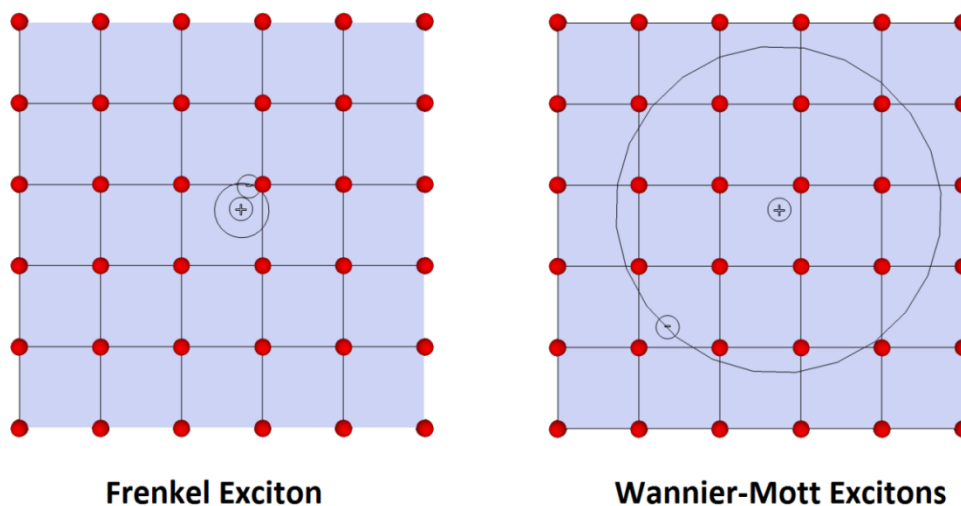


Figure 1-2: Exciton spatial distribution for Frenkel exciton in organic material and Wannier-Mott exciton in inorganic semiconductor material. The “+” and “-” symbols mean “electron” and “hole” respectively in the material.

Due to Pauli’s Exclusion Principle, three fourth of excitons formed in electron excitation in the small molecule solids are not optically active. The spin state of an electron-hole pair can have four possibilities: <spins opposite, phases opposite>, <spin opposite, phases same>, < spins same, phases same>, < spins same, phases opposite> (phase is used to conveniently represent singlet and triplet in vector model, detailed model can be find in ref [17]). Only the <spins opposite, phases opposite> situation obeys selection rule for electron-hole recombination to occur, while other states have a very long lifetime and will eventually decay through non-radiative pathways. Statistically, this results in a maximum theoretical efficiency of 25% for electroluminescence, significantly limiting the intrinsic performances of organic LEDs [18]. For excitons in polymers, although the mechanism is still not very clear, it is found that the singlet exciton population is much higher than  $\frac{1}{4}$ . In fact, the singlet to

triplet state ratio increases as the repeat unit in the polymer chain increases [19]. Beljonne explored the singlet and triplet formation cross-section dependence on chain length [20]. From their calculation, it was found that the tunneling matrix element is larger for transit from charge transfer state to singlet state in long-chain polymers, and the chance for triplet charge transfer states to undergo intersystem crossing or dissociation is also higher, giving the opportunity for triplets to convert to singlets. Therefore, polymer LEDs can potentially achieve high electroluminescence efficiency by efficient use of injected carriers.

### **1.3 Colloidal Quantum Dot**

Due to their low-cost solution based processing and substrate compatibility, polymer LEDs were proposed as a promising candidate to solve the LED integration problem on silicon-based integrated circuits. Polymers' fluorescence can cover the visible wavelength range, but efficient near-infrared emitting polymers are still absent. Some infrared dye-doped polymer LED can permit infrared emission, but with a quite low efficiency [21]. Lead chalcogenides colloidal quantum dots can fill in this deficiency as a solution processed material. Electroluminescent devices operating at telecommunication wavelengths incorporated with PbSe and PbS quantum dots have been reported. Fundamental studies of PbS and PbSe QDs revealed the fact that the large exciton Bohr radii of PbSe and PbS permit stronger confinement than other II-VI or III-V materials at the same quantum dot size. Furthermore, unlike other II-VI and III-V materials, in which the hole and electron Bohr radii are asymmetric, the exciton Bohr radii in lead chalcogenides quantum dots are composed of nearly equal contributions from the electron and hole, allowing both carriers to be extremely quantum-confined [22].

Colloidal quantum dot are inorganic semiconductors synthesized from solution through chemical reaction. The resulting material consists in nanometer-scale particles protected by surface ligands, which provides them good solubility in solution. Over the past several years, the optical and electronic properties of colloidal-synthesized nanocrystals, or quantum dots, have been extensively studied because of their unique optical and electrical features, including high quantum yields, large effective stokes shift, broad absorption and narrow emission. These features offer them potential advantages in diverse applications, such as multimodality imaging, optoelectronics, and nanomedicine. These developments are results of the advances in colloidal quantum dot synthesis that allow for increased control over the shape, size, and emission wavelength of the nanocrystals, and the development of quantum dot thin films formation methods of controlled structure and composition [23]. By changing surface ligand, colloidal quantum dot can be dissolved in various polar and non-polar organic solvent and even in water [24,25]. Besides the controllability on solubility, after deposit quantum dot into solid state thin film form, ligand exchange can also alter the quantum dot film properties including its doping concentration, fluorescent quantum yield and carrier mobility [26]. Compared with epitaxially-grown quantum dots, solution-synthesized quantum dots not only offer higher substrate compatibility and low fabrication cost, but they also provide monodispersed and densely packed quantum dot solid thin film structures which are extremely difficult to realize with epitaxial growth. The quantum dots formed by epitaxy, which relies on lattice mismatch-induced strain between two materials, typically have broad size distribution and low surface densities. Solution-synthesis offers more spherical dots with a size distribution as narrow as 10%, and can form films with quantum dot multiple layers.

Colloidal quantum dots outperform molecular dyes and some organic materials by their characters of good photo-electrical stabilities, easy emission wavelength tunability and higher quantum yield. CdSe, CdS and ZnSe are typical quantum dot materials for visible emission [27–29], and PbS and PbSe are materials used for near-infrared emission[22,25,30–34].

A basic colloidal quantum dot synthesis process using three-neck flask and organic-metallic precursor consists of the following [35]. Organic solvent and surface ligand molecules are heated into high temperature under nitrogen environment. After enough heating of the solution to allow complete dissolve and degas of reacting chemicals, organic-metallic precursors are injected into the hot mixture. Precursors react in solution to form nuclei first and the reaction continuously happens on the nuclei, making them grow larger into quantum dots. The size of the quantum dots can be controlled by adjusting surface ligand concentration in the reaction mixture at the beginning, or via tuning the reaction temperature and time. Figure 1-3 demonstrates the basic reaction setup.

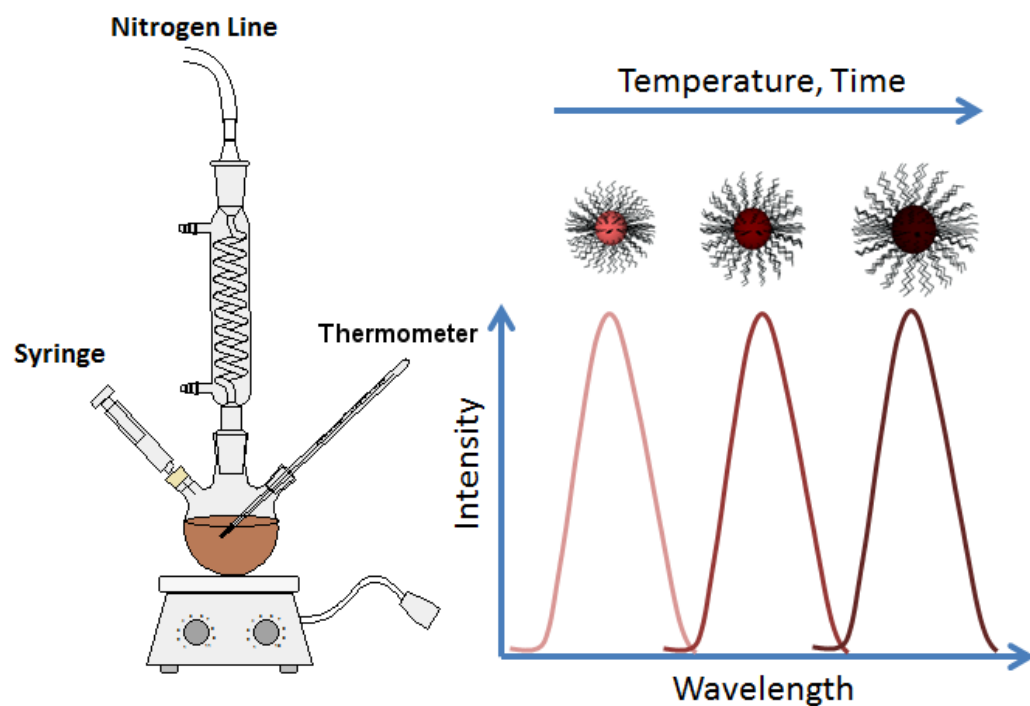


Figure 1-3: Quantum dot synthesis schema using the flask method. Right panel shows the size growth with increasing synthesis temperature.

When the nanoparticle radius is smaller than the Bohr radius of bulk material,  $a_B = \kappa \hbar^2 / \mu e^2$ , where  $\kappa$  is dielectric constant of the material and  $\mu$  is a bulk exciton reduced mass [36], quantum confinement occurs, which raises the band gap of the semiconductor nanoparticle. Accordingly, by tuning the size of the semiconductor nanoparticle, the band gap can be tuned to achieve different light emission wavelengths using the same semiconductor material. Table 1-2 gives the exciton Bohr diameter of typical colloidal quantum dot materials in visible and near infrared regime [37–39]. Combining the use of different semiconductor materials with the size tunability, quantum dot emission can virtually cover the entire visible and infrared

wavelength range. Carefully-controlled synthesis conditions can ensure narrow size distribution of the quantum dots. Therefore, colloidal quantum dot light emitting devices can have much narrower emission peaks, and thus much purer and more saturated color than small molecular and polymer based devices. Colloidal quantum dots attracted significant attention in recent years due to the above mentioned competitive advantages. Meanwhile, comparing with organic small molecules and polymer materials, inorganic semiconductor quantum dot are more stable during device operation, making them highly promising for commercial product applications.

Table 1-2: Exciton bulk Bohr diameter and bulk material band gap for typical colloidal quantum dot materials. [39]

Semiconductor	Exciton Bohr Diameter	Band gap Energy
<b>ZnSe</b>	84 Å	2.58eV
<b>CdS</b>	56 Å	2.53eV
<b>CdSe</b>	60~106 Å <sup>a</sup>	1.74eV
<b>CdTe</b>	150 Å	1.50eV
<b>GaAs</b>	280 Å	1.43eV
<b>Si</b>	37 Å (longitudinal) 90 Å (transverse)	1.11eV
<b>Ge</b>	50 Å (longitudinal) 200 Å (transverse)	0.67eV
<b>PbS</b>	200~400 Å <sup>a</sup>	0.41eV
<b>PbSe</b>	460 Å <sup>a</sup>	0.26eV <sup>b</sup>

<sup>a</sup> Ref [38]

<sup>b</sup> Ref [37]

Compared with quantum well or carbon nanotubes which are confined in one to two dimensions, quantum dots are materials fully quantized in three dimensions. The energy states of zero-dimensional materials are atomic-like discrete levels with a  $\delta$ -function density of states, such as shown in Figure 1-4. The energy gap of the lowest

optical transition of quantum dot can be calculated using equation 1-1 with four terms: the band gap of the bulk semiconductor material  $E_g$ , the quantum confinement energy due to quantization, the attraction between opposite charges due to Coulombic interaction, and the spatial correlation (in meV) between two charges referred-to as Rydberg effect.

$$E = E_g + \frac{\hbar^2}{2} \left( \frac{1}{m_e} + \frac{1}{m_h} \right) \frac{\pi^2}{R^2} - 1.786 \frac{e^2}{\epsilon R} - 0.248 E_{Ry} \quad (1-1)$$

where  $E_{Ry} = 13605.8 \frac{1}{\epsilon^2} \left( \frac{m_0}{m_e} + \frac{m_0}{m_h} \right)^{-1}$ ,  $\hbar$  is the reduced planck constant,  $m_e$  and  $m_h$  are effective masses,  $m_0$  is the free electron mass,  $R$  is the radius of quantum dot,  $e$  is the electron charge,  $\epsilon$  is the permittivity of the material, and  $E_{Ry}$  is referred to as the effective Rydberg effect [40].

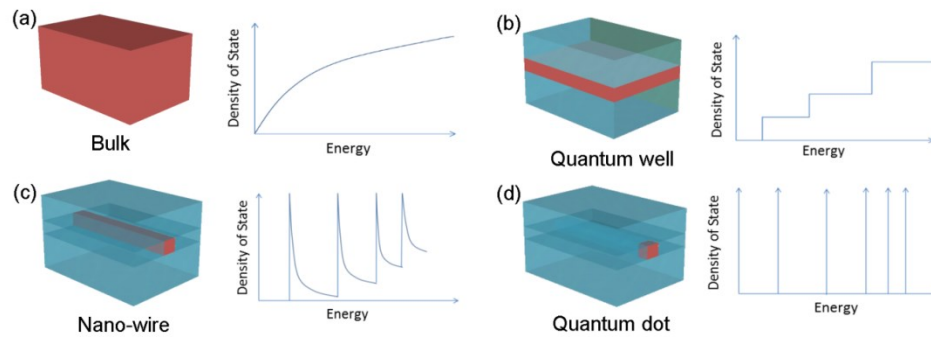


Figure 1-4: Density of states for nano-scale confined materials.

In strong-confinement regime, the confinement energy is much larger than the contribution from Coulomb and Rydberg terms. The confinement energy increases

inversely to the quantum dot radius squared, which causes the total energy of band edge-optical transitions to increase rapidly as the size is reduced. But for large quantum dot, the Coulomb interaction is more important. In three confinement regime:  $a \gg R$ ,  $a \sim R$ , and  $a \ll R$ , different approximations can be used to estimate the exciton energy.

For spherical shape quantum dots surrounded by an infinite potential barrier, the solution for quantized energy level can be written in the parabolic approximation as [41]

$$E_{l,n}^{e,h} = \frac{\hbar^2 \phi_{l,n}^2}{2m_{e,h} R^2} \quad (1-2)$$

where  $\phi_{l,n}$  is the  $n^{\text{th}}$  root of the spherical Bessel function of order  $l$   $J_l(\phi_{l,n}) = 0$ , the four lowest roots are  $\phi_{0,0} = \pi$ ,  $\phi_{1,0} = 4.49$ ,  $\phi_{2,0} = 5.76$  and  $\phi_{0,1} = 2\pi$ . But the assumption of simple parabolic conduction and valence bands used to obtain equation (1-2) is oversimplified to represent properly the real band structure of semiconductor quantum dots, bringing discrepancies between equation (1-2) and most experimental measurements. A multi-band effective mass approximation proposed by Pidgeon and Brown using 8-band Luttinger-Kohn Hamiltonian to simultaneously take into account the conduction and valence bands' structure[35]. This model can predict the band energy more accurately, agreeing with experimental absorption spectra measurements [41]. With the consideration of intrinsic crystal field [42] and nanocrystal anisotropy[43], large Stokes shift and long exciton lifetime of QD can be consistently explained as a result of optically inactive lowest energy states [44]. In some case,

within a range of quantum dot diameter, the exciton energy and quantum dot size relation can also be very accurately predicted by empirical formula as well [30].

For quantum dot material, there is always a large redshift, called Stokes shift, from the first absorption peak to the PL emission peak of semiconductor quantum dots [44]. Stokes shift can be explained by the presence of “dark excitons” in quantum dots. This exciton state has a slightly lower energy than the bright exciton state [44]. It cannot couple directly with photons (angular momentum projection of  $\pm 1$ ) due to its angular momentum of  $\pm 2$ . During photo-excitation, the system absorbs a higher energy photon to excite the electron into the lowest bright exciton state, then via phonon interaction relaxes into the dark state, which can radiatively recombine after a long lifetime through phonons interaction. The difference in energy between lowest bright exciton states and dark exciton states causes the Stokes shift between absorption and photoluminescence peaks. Factors such as asymmetry of the quantum dots, electron-hole exchange interactions, exciton polaritons [45], and acoustic phonons all contribute to the split between dark and bright states in quantum dots.

With the development of better quantum dot synthesis methods, size uniformity and quantum efficiency for visible and infrared colloidal quantum dot were greatly improved through temperature and precursor control. The successful synthesis of core-shell and gradient shell structures further boosted quantum dots' fluorescence quantum yields [29]. For visible range, a gradient-changing alloy layer of  $\text{Cd}_{1-x}\text{Zn}_x\text{Se}_{1-y}\text{S}_y$  synthesized in a single-step method can provide quantum yields up to 80% in solvent, with a narrow emission spectrum FWHM (full width at half maximum)  $< 35\text{nm}$  [46]. Gradient change core shell structure relieves the lattice mismatch and confines electrons and holes within the core, passivating the exciton quenching due to

quantum dot surface defects. It is reported that gradient core-shell structure can also suppress quantum dot blinking which is a results of Auger non-radiative recombination process [29]. For infrared PbS and PbSe quantum dots, the quantum yield can range from 3% to 80%, dependent on quantum dot size as summarized in Ref [47]. Quantum yields for larger size dots are generally lower than smaller quantum dots because of the increased surface defect densities in larger dots. Surface defect is a key parameter that affects the photoluminescence quantum yield, since high quantum yields often result from good surface passivation by the ligand molecules surrounding the quantum dots. Surface ligand exchange can affect the surface protection, therefore changing the thin film photoluminescence quantum yield [48].

Small molecular ligands attached around quantum dots during the chemical synthesis procedure are an important component of quantum dots that provide them with good stability and solubility in common organic solvents. By manipulating and exchanging the surface ligands, quantum dot solubility [49,50], photoluminescence quantum yield [51], surface chemistry & functionality [52,53] as well as electronic properties [54,55] can all be controllably affected.

Short dithiol ligand exchange is a recently developed approach that completely changed the scenario of quantum dot incorporation in optoelectronic devices [26]. To allow quantum dots to dissolve stably in solution, the ligands are generally long (typically a 2.5 nm-long oleic acid in the case of lead-salt quantum dot synthesis). After depositing these quantum dots into thin films, the long ligand inhibits carrier transport between nanocrystals, resulting in quantum dot films with large resistance, which is impractical for optoelectronic applications. Therefore, short ligand exchanges such as small dithiol molecules have been widely explored for quantum dot use in

devices. In this ligand-exchange process, short cross-linking molecules with strong thiolated groups on each end are used to replace the oleate capping group around colloidal nanocrystals to achieve the cross-linking of the nanocrystals into films[26,56–58]. High structural quality and excellent electronic transport properties have propelled these self-assembled nanocrystalline lead-chalcogenide film structures to the forefront of cutting-edge research in the area of low-cost photovoltaic and photodetector platforms[59–61]. Chapter 4 investigated PbS quantum dot thin film properties differences after two kinds of dithiol ligands, namely benzenedithiol (BDT) and ethanedithiol (EDT).

#### **1.4 LEDs Made from Organic, Quantum Dots and Hybrid Materials**

The first organic electroluminescent device structure [62,63] originally consisted of a small molecules crystal layer sandwiched between two electrode contacts, and the operating voltages could be as high as 1000 Volts [64]. In 1987, Ching W. Tang and Steven Van Slyke from Kodak demonstrated the first practical organic light emitting diode structure [2]. Two organic materials acting as hole-transporting layer (TPD) and emissive electron-transporting layer (Alq<sub>3</sub>) were incorporated in the device. ITO was used as the transparent anode and Mg as the cathode to reduce the injection barrier of electrons from conventional cathode-like Ag or Al into Alq<sub>3</sub>. Compared with single-layer structure, two and multi-layer structures with electron- or hole-specified transport on cathode and anode side respectively can (1) decrease device resistance for carrier injection and transport, (2) create holes build-up at the heterojunction interface which can help electron injection via built-in electrical field, thus balancing electrons and holes, (3) increase exciton formation by introducing electron and hole blocking layer, and (4) confine the recombination region

away from the metal cathode where higher rates of exciton quenching are observed. Figure 1-5 shows a multilayer device structure including all possible functional layers and the typical energy band alignment to achieve the function of each layer used in this structure. In most of the actual devices, only a few of these layers are included due to material limitation or fabrication complexity, and some of the functional layers are combined in one layer such as Alq3 or F8BT materials that can function as an electron transport layer as well as an emission layer, and a hole transporting material with high LUMO level can also block electrons due to the large barrier for electron injection into this material.

During device operation, a voltage is applied between cathode and anode contact across the device structure. On the cathode side, electrons are injected from the cathode into the LUMO level of the electron transport layer. Most organic materials have a high LUMO level and the carrier mobilities are 5~7 orders of magnitude lower compared with their organic counterparts. Thus low work function metals must be used to achieve sufficient carrier injection and assure high quantum efficiencies in organic LEDs. Calcium, Magnesium and Barium are considered more preferable than Aluminum, Silver, and Gold, which are conventional electrode contact materials. But low work function metals are susceptible to degradation related to oxygen and moisture, in part, causing low stability of organic LEDs. The metal ions can also drift easily into the organic layer, subsequently creating defects that reduce the lifetime of the device. On the anode side, holes are injected from transparent ITO anode into HOMO level of hole transporting layer. ITO has a work function of  $\sim 5.1\text{eV}$ , promoting efficient hole injection. Electrons and holes drift toward each other under external electromagnetic field, meet and form excitons in the emission layer. If

excitons are formed in other layers, energy transfer mechanism can allow non-radiative exciton energy transfer from the large band gap material layers into smaller band gap emission layer via Förster or Dexter mechanisms. As can be seen from Figure 1-5, carrier-blocking layer can prevent injected carriers from leaking through the whole structure, confining carriers in the emission layer to increase the chance of exciton formation.

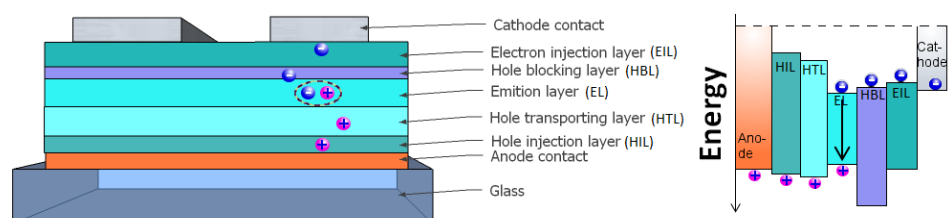


Figure 1-5: Multilayer device structure including all possible functional layers and the typical energy band alignment to achieve the function of each layer used in this structure.

Multilayer structures can be achieved through layer-by-layer thermal evaporation for small-molecules devices, but are much harder to achieve for polymer LEDs. Conjugated polymers have similar solubility in common organic solvents, thus the bottom layer will often be dissolved and blended with the top layer materials during spin-casting, destroying the multilayer structure. Only a very limited number of polymers can be used for multilayer device structure such as PPV, which requires high temperature baking polymerization process under high vacuum. PPV layer forms a cross-linked polymer network which does not dissolve in solvent anymore after high temperature thermal treatment, thus further deposition of other solution processed

polymer on top of PPV is possible. Given the difficulty of making multilayered polymer LED, blend polymer LED are mostly used in polymer LED literatures, as good performances can be achieved by simply adjusting polymer solution solvent to control phase separation in polymer blend thin film. For polymer photovoltaic devices, rich heterojunction interface is desired to increase the chance for exciton dissociation and form free electron- and hole-current, therefore, small domain size is preferable to increase the interface area. For light-emitting devices, different constraints on bulk heterojunction interface are applied for device optimization. There, excitons formed in emission polymer either by direct electron-hole encounter or energy transfer from a larger band gap polymer can drift in polymer domains before they recombine radiatively. Given an exciton diffusion length on the order of  $\sim 10\text{nm}$ , domain separation larger than this range in blend film structure is favorable for an LED structure to prevent exciton breaking at interface before recombination. Solvent effect on blend polymer LED performance will be further discussed in details in chapter 3.

Typically, I-V characteristics of conductive polymer layer are usually bulk-limited rather than injection-limited, in which the metal contact is the main current limiting factor, due to the low carrier mobilities in polymer thin film. Carriers injected into polymer thin films form built-in electromagnetic field that impedes further carrier injection. The field-dependent carrier mobility in polymer also needs to be considered to describe current densities in polymer LEDs. Mott-Gurney law gives the space-charge limited current equation. Combining with field-dependent mobility, a simple device I-V model can be used for device of single carrier injection:

$$J_{SCLC}^{PF} = \frac{9}{8} \varepsilon \mu_0 \frac{V^2}{d^3} \exp\left(\beta \frac{V}{d}\right) \quad (1-3)$$

Where  $J_{SCLC}^{PF}$  is the current density,  $\varepsilon = \varepsilon_0 \varepsilon_r$  is the permittivity of the polymer,  $\mu_0$  is the carrier zero field mobility,  $d$  is thickness of the polymer film,  $V$  is the applied bias and  $\beta$  is the field effect mobility coefficient, which depends upon trap depths in organic semiconductors [65]. Varying the efficiency of carrier injection from each electrode and combining with relative mobility of electrons and holes in the emissive layer, the recombination region can be adjusted. The best scenario for achieving high efficiency is to confine the recombination region in the middle of the device, where electrode quenching is reduced to the minimum.

Lambert's distribution defines the luminous space pattern of the polymer LED electroluminescence, that is the emission intensity spatial distribution is proportional to the cosine of  $\theta$  between observer's line of sight and surface normal,  $I = I_0 \cos(\theta)$  [66], where  $I_0$  is the maximum intensity observed from the surface normal direction as shown in Figure 1-6. According to this intensity distribution, by integral the half space above emission surface numerically, the total power emitted by the LED can be estimated from a measured power within a given cone by  $P_0 = P / \sin^2(\varphi)$ , where  $P_0$  is the total power emitted by the LED and  $\varphi$  is the half-angle of the cone.

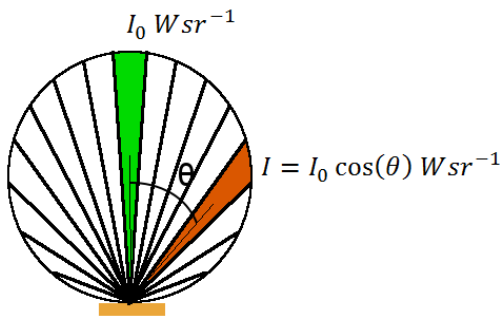


Figure 1-6: Lambert distribution.

Colloidal quantum dots were introduced into organic LEDs only since 1994 [67]. Colloidal quantum dots combine the benefits of large area device fabrication capacity of polymer materials with the good electrical stability of inorganic materials. Meanwhile, the emission wavelength of quantum dot LEDs can be controllably tuned by adjusting quantum dot size during synthesis. Two approaches are mostly used for quantum dot LEDs found in the literature: 1) quantum dots are photo excited by a primary LED, and 2) direct electrical excitation by carrier injection [67]. For the first approach, the primary blue or UV LED can be either organic or inorganic. It is independent from the quantum dot layer, which does not participant in any charge transport process. Photoluminescent quantum dots are simply deposited on top of the primary LED structure to achieve the desired emission. The second approach achieves electroluminescence by direct carrier injection. The first realization of carrier injection infrared quantum dot/organic LED employed a blend layer of polymer and quantum dots. The development of hybrid organic/inorganic nanocomposite materials is a promising strategy to create new functional materials with superb optical and electronic properties not accessible in any of the individual components. Some of the potential advantages offered by this hybrid approach include: a) solution-based processing, flexible substrate compatibility and good charge transport property from polymer matrix; b) fast exciton extraction at the heterojunction interface, and c) broad absorption band, tunable optical bandgap and narrow emission linewidths from semiconducting quantum dots. The performance of these hybrid devices crucially depends on energy bands matching at the interface, blend film morphology, composition ratios, and nanocrystal shape. [68].

For the blend hybrid device as in Figure 1-7 (a), quantum dots and polymer are blended in solution, then spin-coated on to hole injection polymer PEDOT:PSS (poly(3,4-ethylenedioxythiophene) poly(styrenesulfonate)) covered ITO substrate [67]. Quantum dots have long insulating organic ligands attached to their surface, resulting in low electron injection efficiencies and insufficient charge transport between quantum dots. Device performance was very limited in blend structures and structures with thick quantum dot layers [69]. Bawendi's group fabricated a device consisting of a single layer of quantum dot sandwiched between organic electron- and hole-transporting layers by utilizing polymer quantum dot phase separation during spin-coating [70]. Quantum dot and hole transporting TPD polymer were first blended in solution first by carefully choosing concentration ratio. During spin-coating, the quantum dots produced a self-organized single layer on top of the TPD layer due to phase separation. Then, an electron-transporting layer of Alq3 was deposited by thermal evaporation, keeping the bottom TPD/quantum dot layer intact. Figure 1-7 (b) shows the device structure. An external quantum efficiency of 0.5% was reported from this structure. In this device design, quantum dots are confined between electron-transporting and hole-transporting organic materials, with electrons and holes being injected into the quantum dot layer at the junction to ensure efficient carrier recombination. The high LUMO of the TPD makes the hole-transporting layer a good electron-blocking layer as well, confining electrons in the quantum dot region. Due to the large band gap of the organic materials, excitons formed in the organic layer can transfer their energy to quantum dot excitons, but the green emission from Alq3 can still be observed in this structure [71,72]. The infrared output power of this device is also very weak due to the ultrathin monolayer of quantum dots incorporated into the

structure. In recent years, metal oxide are introduced into organic and quantum dot hybrid LED structures. TiO<sub>2</sub> [73] and ZnO [74] have all been subsequently used as good electron-transporting material. Figure 1-7 (c) is an example of a quantum dot-sensitized solar cell with TiO<sub>2</sub> as electron-transporting material. Inorganic metal oxides are more robust and stable in air and moisture than organic materials. But the metal oxides deposited by sputtering or thermal evaporation increase the fabrication cost and limit large-scale fabrication capacity. Colloidal or sol-gel fabricated metal oxide nanoparticles also suffer from the low carrier transport mobilities before undergoing high temperature thermal treatment, which can potentially harm other material and quantum dot layers deposited underneath the metal-oxide electron-transporting layer. The quantum efficiencies of organic or quantum dot LEDs using metal oxide as electron transporting layer are still lower than devices using pure conjugated organic materials [65]. Many new metal oxide materials are still undergone investigation, and significant improvements in LED performances have been reported for ZnO, TiO<sub>2</sub> and MoO<sub>3</sub> incorporated devices. Significant research efforts are also invested into low-temperature metal-oxide fabrication to extend their applicability for various substrates and other temperature-sensitive materials [75].

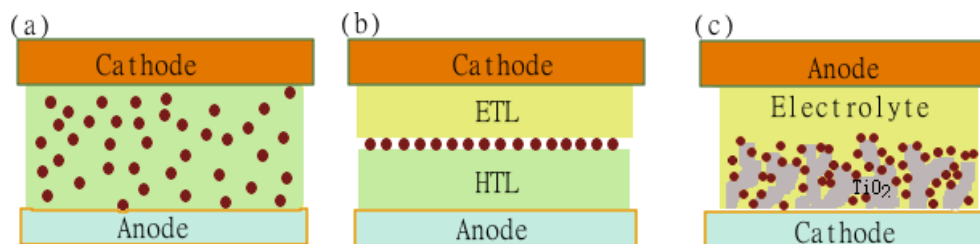


Figure 1-7: Conventional hybrid quantum dot device configuration. (a) polymer/quantum dot blend device (b) monolayer of quantum dot sandwiched between organic electron transport layer (ETL) and hole transport layer (HTL) (c) Quantum dot-sensitized device.

As mentioned previously, short dithiol ligand exchange has completely changed the scenario of quantum dot incorporation into optoelectronic devices [26]. Ligand-exchange can provide multilayered quantum dot thin films with high structural quality and excellent electronic transport properties. Since the carrier doping densities and carrier mobilities in thin film highly depend on quantum dot surface states and the spacing between quantum dots, choosing the proper surface ligand in the exchange process can significantly alter the thin film electronic properties to target different device applications. Meanwhile, after ligand-exchange, the quantum dot layer becomes unsolvable in nonpolar solvent. Therefore, layer-by-layer deposition can be used to fabricate thin film with superior structure quality and better charge transport properties. The possibility of using bulk quantum dot layers in photovoltaic, photodetector and LED platforms significantly improves the device performances, and extends the range of possible device configurations. Figure 1-8 shows several quantum dot device configurations using cross-linked quantum dot layers.

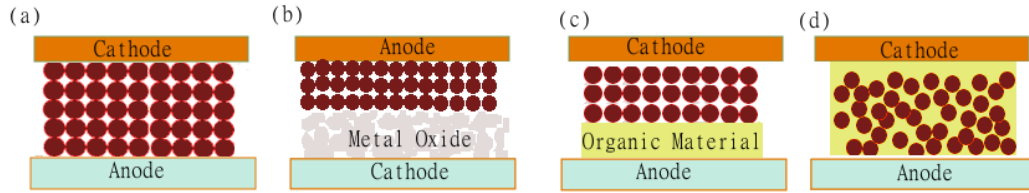


Figure 1-8: Four possible device configurations using cross-linked bulk quantum dot layers as the functional material. (a) The Schottky device with pure quantum dot layer, (b) Depletion heterojunction between metal-oxide and quantum dot materials, (c) Organic material as carrier transport and blocking layer in hybrid multilayer structure, (d) cross-linked quantum dot in polymer quantum dot blend bulk heterojunctions [76].

### 1.5 Surface Plasmon-Enhanced LEDs

Surface plasmon modes stem from the collective oscillations of free electrons in metals. The particular properties of surface plasmons (SPs) in metallic nanostructures and their interaction with photons and excitons have generated tremendous research interests and efforts in the last decades[77–82]. Metallic nanostructures have now been widely used to enhance Raman scattering [83], optical absorption [84] and photoluminescence of fluorescent materials[77]. Recently, the phenomenon of SP-enhanced exciton decay rate has also been exploited on organic and inorganic material electroluminescence (EL), offering great promising on improving LED performance [85].

It is well understood that flat metal films placed directly atop a fluorescent material quench excitons by causing exciton dissociation and coupling with the propagating surface plasmon polariton (SPP) mode [86,87], which ultimately results in non-radiative thermal loss in the metal film due to a momentum mismatch preventing photon emission. Using GaN quantum wells [80], it was previously demonstrated that two key factors can contribute to switching this metal quenching into strong metal-

enhanced luminescence: (1) having a thin spacer layer between the metal film and the luminescent material to prevent exciton dissociation and (2) using metal nanostructures supporting localized SP modes that can couple with the photon-emission mode. The enhancement is explained by a high electromagnetic density of states  $\rho$  introduced by surface plasmons around the metal structure, through which the exciton decay rate is enhanced according to Purcell's theory [88].

Using quantum theory, the probability of spontaneous emission is proportional to number of radiation oscillators per unit volume  $8\pi\nu^2/c^3$ , where  $\nu$  is the frequency of the oscillators and  $c$  is the speed of light. Purcell predicted that when the system is coupled to a resonant electrical circuit, the number of radiation oscillators per unit volume is associated with the cavity Q factor [88]. The spontaneous emission probability is thereby increased by a factor of  $f = 3Q\lambda^3/4\pi^2V$ , where  $V$  is the volume of the resonator. SP resonance can be considered as a novel cavity in which the emitters surround outside of the cavity and remain strongly-coupled with the cavity. Although the Q factor is smaller compared with other cavity architectures due to high metal losses in the particle, the mode is strongly-confined at the nano-scale thus significantly reducing the  $V_{\text{eff}}$  to yield a large Purcell enhancement factor. Enhanced spontaneous emission competes and dominates over other non-radiative recombination channels in photoluminescence and electroluminescence measurements, resulting in high quantum yield  $\eta = \frac{\Gamma_{\text{rad}}}{\Gamma_{\text{rad}} + \Gamma_{\text{non-rad}}}$ , where  $\Gamma_{\text{rad}}$  and  $\Gamma_{\text{non-rad}}$  are radiative recombination rate and non-radiative recombination rate respectively.

Thus, enhanced electroluminescence using noble metal nanoparticles formed by vacuum evaporation and thermal annealing has been successfully observed in GaN-based quantum-well LEDs[89–93], Si-based LEDs [81,94] and small molecule

OLEDs [77,95–97]. Chen et al., who have successfully validated the possibility of SP enhancement in polymer LED (PLED) structures, applied a special low-temperature pulsed laser anode deposition method to embed silver nanoparticles in a gallium-doped zinc oxide anode layer prior to polymer spin-coating [32]. Besides the stringent requirements on the anode deposition process, a very modest enhancement factor of about 2 was achieved, likely due to the large spatial separation between the SP mode and the exciton formation region in the polymer film [32]. Meanwhile, colloidal metallic nanoparticles allowing facile solution processing were used to achieve SP enhancement on small molecule-based OLEDs by electrostatic absorption into Au nanoparticle layers or through Au nanoparticles blending into a hole-injecting polymer layer. Their results also confirm that high nanoparticle densities can be beneficial for producing high SP enhancement. In chapter 5, a simple all solution-processed SP-enhanced PLED structure is produced, with a high enhancement factor obtained by using solution synthesized colloidal silver (Ag) nanoparticles encapsulated with a long oleylamine ligand.

## **1.6 Structure of This Thesis**

Given the low-cost advantage for industry manufacturing and potential roll-to-roll ink-jet printing fabrication, solution processing is expected to replace current high cost vacuum deposition methods often required for deposition of inorganic materials and small molecules. Modern polymer materials and colloidal quantum dots also show relatively better optical and electrical stability in oxygen and moisture environment than most fluorescent small-molecule materials. Exceptional properties like high absorption cross-section, size tunability and narrow luminescence peak have initiated a wide range of application of colloidal quantum dots in opto-electronic devices. In a

polymer-quantum dot hybrid device, the polymer can act as carrier transport layer, carrier blocking layer, and to form a hetero-junction with quantum dots to offer superior device performances. Colloidal synthesis of metallic nanoparticles also introduced the possibility of using surface plasmon enhancement effect on material electroluminescence.

This thesis focuses on solution-processed light emitting diodes based on polymer blend, polymer/PbS and polymer/Ag nanoparticles hybrid structures. Two types of polyfluorenes: TFB (poly(9,9'-dioctylfluorene-co-N-(4-butylphenyl)diphenylamine) and F8BT (poly(9,9'-dioctylfluorene-co-benzothiadiazole) were chosen as the reference polymer system used for device fabrication and material property investigation. Polyfluorenes are superb materials for polymer LEDs due to their high luminescence efficiency, resistance to photo-oxidation and good processability [98]. Combining electronic and optical measurements with morphological analysis, the impact of aromatic and non-aromatic solvents used in polymer blend film preparation is first investigated in this thesis. We see that charge transport and film morphology can be manipulated by choosing the right solvent to enhance polymer LED efficiency and output power. For polymer and quantum dot hybrid LEDs, this thesis will focus on the infrared LED made from lead sulfide (PbS) quantum dots, which have high quantum yield in infrared wavelength range of interest. Lead sulfide dots have large dielectric constants, large bohr radius, allow efficient multiple exciton generation, and large carrier mobilities. Solution based processing of this infrared emitting material offers the possibility of direct integration on silicon substrate. A polymer/quantum dot heterojunction multilayer structure produced using orthogonal solvents is demonstrated. Quantum dot ligand exchange is

first applied to increase carrier transport in quantum dot thick films in LED structures. The ligand exchange effect is further analyzed by doping concentration and carrier mobility investigation to explain their emission properties. For surface plasmon-enhanced polymer LEDs, an all solution-processed polymer/Ag nanoparticle hybrid device is presented, and the enhancement dependence on Ag nanoparticle incorporation is also investigated.

Chapter 2 introduces the experimental methods for device fabrication, and the characterization methods used to investigate material and device properties. Chapter 3 demonstrates the solvent and baking effect on polymer thin film morphology and polymer LED performance. Chapter 4 discusses quantum dot ligand exchange effect on exciton behavior in polymer and quantum dot hybrid structure. Chapter 5 demonstrates a QD/polymer hybrid LED device. Emission wavelength can be adjusted from 980nm to 1600nm by incorporating different sizes of quantum dots in the same device structure. Chapter 6 shows the impact of metallic nanoparticles' incorporation to improve the performances of polymer LEDs. Finally, chapter 7 presents the main conclusions and future research prospects.

## REFERENCES

- [1] O. V. Losev, "Luminous carborundum [silicon carbide] detector and detection with crystals," *Telegr. ya i Telef. bez Provodov*, vol. 44, pp. 485–494, 1927.
- [2] C. W. Tang and S. A. VanSlyke, "Organic electroluminescent diodes," *Appl. Phys. Lett.*, vol. 51, no. 12, p. 913, Sep. 1987.
- [3] N. C. Greenham, S. C. Moratti, D. D. C. Bradley, R. H. Friend, and A. B. Holmes, "Efficient light-emitting diodes based on polymers with high electron affinities," *Nature*, vol. 365, no. 6447, pp. 628–630, Oct. 1993.
- [4] S. Reineke, F. Lindner, G. Schwartz, N. Seidler, K. Walzer, B. Lüssem, and K. Leo, "White organic light-emitting diodes with fluorescent tube efficiency.," *Nature*, vol. 459, no. 7244, pp. 234–8, May 2009.
- [5] T. Tsujimura, Y. Kobayashi, K. Murayama, A. Tanaka, M. Morooka, E. Fukumoto, H. Fujimoto, J. Sekine, K. Kanoh, K. Takeda, K. Miwa, M. Asano, N. Ikeda, S. Kohara, S. Ono, C.-T. Chung, R.-M. Chen, J.-W. Chung, C.-W. Huang, H.-R. Guo, C.-C. Yang, C.-C. Hsu, H.-J. Huang, W. Riess, H. Riel, S. Karg, T. Beierlein, D. Gundlach, S. Alvarado, C. Rost, P. Mueller, F. Libsch, M. Mastro, R. Polastre, A. Lien, J. Sanford, and R. Kaufman, "4.1: A 20-inch OLED Display Driven by Super-Amorphous-Silicon Technology," *SID Symp. Dig. Tech. Pap.*, vol. 34, no. 1, p. 6, 2003.
- [6] "'Lighting'. Energy Efficiency & Renewable Energy," *US Department of Energy*, 2011. [Online]. Available: <http://energy.gov/eere/energybasics/articles/lighting-basics>.
- [7] L. P. Lu, C. E. Finlayson, and R. H. Friend, "Thick polymer light-emitting diodes with very high power efficiency using Ohmic charge-injection layers," *Semicond. Sci. Technol.*, vol. 29, no. 2, p. 025005, Feb. 2014.
- [8] F. Huang, P.-I. Shih, C.-F. Shu, Y. Chi, and A. K.-Y. Jen, "Highly Efficient Polymer White-Light-Emitting Diodes Based on Lithium Salts Doped Electron Transporting Layer," *Adv. Mater.*, vol. 21, no. 3, pp. 361–365, Jan. 2009.

- [9] T. Perry and G. Zorpette, "Oled TV arrives [2013 Tech To Watch]," *IEEE Spectr.*, vol. 50, no. 1, pp. 46–47, Jan. 2013.
- [10] R. H. Partridge, "Radiation sources," 05/620,4501975.
- [11] A. Rockett, *The Materials Science of Semiconductors*. Springer, 2007, p. 640.
- [12] J.-L. Brédas, J. Cornil, D. Beljonne, D. A. dos Santos, and Z. Shuai, "Excited-State Electronic Structure of Conjugated Oligomers and Polymers: A Quantum-Chemical Approach to Optical Phenomena," *Acc. Chem. Res.*, vol. 32, no. 3, pp. 267–276, Mar. 1999.
- [13] G. C. Bazan, Y.-J. Miao, M. L. Renak, and B. J. Sun, "Fluorescence Quantum Yield of Poly(p-phenylenevinylene) Prepared via the Paracyclophene Route: Effect of Chain Length and Interchain Contacts," *J. Am. Chem. Soc.*, vol. 118, no. 11, pp. 2618–2624, Jan. 1996.
- [14] P. W. M. Blom, V. D. Mihailechi, L. J. a. Koster, and D. E. Markov, "Device Physics of Polymer:Fullerene Bulk Heterojunction Solar Cells," *Adv. Mater.*, vol. 19, no. 12, pp. 1551–1566, Jun. 2007.
- [15] A. Kohler, D. A. dos Santos, D. Beljonne, Z. Shuai, J.-L. Bredas, A. B. Holmes, A. Kraus, K. Mullen, and R. H. Friend, "Charge separation in localized and delocalized electronic states in polymeric semiconductors," *Nature*, vol. 392, no. 6679, pp. 903–906, Apr. 1998.
- [16] M. Pope and C. E. Swenberg, *Electronic Processes in Organic Crystals and Polymers*. Oxford University Press, 1999, p. 1328.
- [17] N. J. Turro, V. Ramamurthy, and J. C. Scaiano, *Principles of Molecular Photochemistry: An Introduction*. University Science Books; 1st edition, 2008, p. 495.
- [18] M. A. Baldo, D. F. O'brien, M. E. Thompson, and S. R. Forrest, "Excitonic singlet-triplet ratio in a semiconducting organic thin film," *Phys. Rev. B*, vol. 60, pp. 14422–14428, 1999.
- [19] M. Wohlgenannt, X. Jiang, Z. Vardeny, and R. Janssen, "Conjugation-Length Dependence of Spin-Dependent Exciton Formation Rates in  $\Pi$ -Conjugated Oligomers and Polymers," *Phys. Rev. Lett.*, vol. 88, no. 19, p. 197401, Apr. 2002.

- [20] D. Beljonne, A. Ye, Z. Shuai, and J.-L. Brédas, “Chain-Length Dependence of Singlet and Triplet Exciton Formation Rates in Organic Light-Emitting Diodes,” *Adv. Funct. Mater.*, vol. 14, no. 7, pp. 684–692, Jul. 2004.
- [21] J. R. Sommer, R. T. Farley, K. R. Graham, Y. Yang, J. R. Reynolds, J. Xue, and K. S. Schanze, “Efficient near-infrared polymer and organic light-emitting diodes based on electrophosphorescence from (tetraphenyltetranaphtho[2,3]porphyrin)platinum(II),” *ACS Appl. Mater. Interfaces*, vol. 1, no. 2, pp. 274–8, Feb. 2009.
- [22] J. J. Peterson and T. D. Krauss, “Fluorescence spectroscopy of single lead sulfide quantum dots,” *Nano Lett.*, vol. 6, no. 3, pp. 510–4, Mar. 2006.
- [23] P. O. Anikeeva, C. F. Madigan, S. a. Coe-Sullivan, J. S. Steckel, M. G. Bawendi, and V. Bulović, “Photoluminescence of CdSe/ZnS core/shell quantum dots enhanced by energy transfer from a phosphorescent donor,” *Chem. Phys. Lett.*, vol. 424, no. 1–3, pp. 120–125, Jun. 2006.
- [24] D. Gerion, F. Pinaud, S. C. Williams, W. J. Parak, D. Zanchet, S. Weiss, and A. P. Alivisatos, “Synthesis and Properties of Biocompatible Water-Soluble Silica-Coated CdSe/ZnS Semiconductor Quantum Dots †,” *J. Phys. Chem. B*, vol. 105, no. 37, pp. 8861–8871, Sep. 2001.
- [25] L. Bakueva, I. Gorelikov, S. Musikhin, X. S. Zhao, E. H. Sargent, and E. Kumacheva, “PbS Quantum Dots with Stable Efficient Luminescence in the Near-IR Spectral Range,” *Adv. Mater.*, vol. 16, no. 11, pp. 926–929, Jun. 2004.
- [26] J. M. Luther, M. Law, Q. Song, C. L. Perkins, M. C. Beard, and A. J. Nozik, “Structural, optical, and electrical properties of self-assembled films of PbSe nanocrystals treated with 1,2-ethanedithiol,” *ACS Nano*, vol. 2, no. 2, pp. 271–80, Feb. 2008.
- [27] B. O. Dabbousi, M. G. Bawendi, O. Onitsuka, and M. F. Rubner, “Electroluminescence from CdSe quantum-dot/polymer composites,” *Appl. Phys. Lett.*, vol. 66, no. 11, p. 1316, 1995.
- [28] Z. Tan, F. Zhang, T. Zhu, J. Xu, A. Y. Wang, J. D. Dixon, L. Li, Q. Zhang, S. E. Mohny, and J. Ruzyllo, “Bright and color-saturated emission from blue light-emitting diodes based on solution-processed colloidal nanocrystal quantum dots,” *Nano Lett.*, vol. 7, no. 12, pp. 3803–7, Dec. 2007.

- [29] X. Wang, X. Ren, K. Kahen, M. a Hahn, M. Rajeswaran, S. Maccagnano-Zacher, J. Silcox, G. E. Cragg, A. L. Efros, and T. D. Krauss, “Non-blinking semiconductor nanocrystals.,” *Nature*, vol. 459, no. 7247, pp. 686–9, Jun. 2009.
- [30] I. Moreels, K. Lambert, D. Smeets, D. De Muynck, T. Nollet, J. C. Martins, F. Vanhaecke, A. Vantomme, C. Delerue, G. Allan, and Z. Hens, “Size-dependent optical properties of colloidal PbS quantum dots.,” *ACS Nano*, vol. 3, no. 10, pp. 3023–30, Oct. 2009.
- [31] X. Ma, F. Xu, and S. G. Cloutier, “Impact of different dithiol treatments on the optoelectronic properties of self-assembled PbS nanocrystalline films,” in *Frontiers in Optics / Laser Science 2011*, 2011, p. FMK3.
- [32] L. Sun, J. J. Choi, D. Stachnik, A. C. Bartnik, B.-R. Hyun, G. G. Malliaras, T. Hanrath, and F. W. Wise, “Bright infrared quantum-dot light-emitting diodes through inter-dot spacing control.,” *Nat. Nanotechnol.*, vol. 7, no. 6, pp. 369–73, Jun. 2012.
- [33] K. N. Bourdakos, D. M. N. M. Dissanayake, T. Lutz, S. R. P. Silva, and R. J. Curry, “Highly efficient near-infrared hybrid organic-inorganic nanocrystal electroluminescence device,” *Appl. Phys. Lett.*, vol. 92, no. 15, p. 153311, 2008.
- [34] E. Lifshitz, M. Brumer, a Kigel, a Sashchiuk, M. Bashouti, M. Sirota, E. Galun, Z. Burshtein, a Q. Le Quang, I. Ledoux-Rak, and J. Zyss, “Air-stable PbSe/PbS and PbSe/PbSexS1-x core-shell nanocrystal quantum dots and their applications.,” *J. Phys. Chem. B*, vol. 110, no. 50, pp. 25356–65, Dec. 2006.
- [35] M. A. Hines and G. D. Scholes, “Colloidal PbS Nanocrystals with Size-Tunable Near-Infrared Emission: Observation of Post-Synthesis Self-Narrowing of the Particle Size Distribution,” *Adv. Mater.*, vol. 15, no. 21, pp. 1844–1849, Nov. 2003.
- [36] S. A. Coe-sullivan, “Hybrid Organic/Quantum Dot Thin Film Structures and Devices,” *PhD thesis, Massachusetts Inst. Technol.*, 2005.
- [37] F. W. Wise, “Lead Salt Quantum Dots: the Limit of Strong Quantum Confinement,” *Acc. Chem. Res.*, vol. 33, no. 11, pp. 773–780, Nov. 2000.
- [38] Z. Hens, D. Vanmaekelbergh, E. Kooij, H. Wormeester, G. Allan, and C. Delerue, “Effect of Quantum Confinement on the Dielectric Function of PbSe,” *Phys. Rev. Lett.*, vol. 92, no. 2, p. 026808, Jan. 2004.

- [39] T. J. Bukowski and J. H. Simmons, “Quantum Dot Research: Current State and Future Prospects,” *Crit. Rev. Solid State Mater. Sci.*, vol. 27, no. 3–4, pp. 119–142, Jul. 2002.
- [40] G. Einevoll, “Confinement of excitons in quantum dots,” *Phys. Rev. B*, vol. 45, no. 7, pp. 3410–3417, 1992.
- [41] A. Efros and M. Rosen, “The Electronic Structure of Semiconductor Nanocrystals,” *Annu. Rev. Mater. Sci.*, vol. 30, pp. 475–521, 2000.
- [42] A. L. Efros, “Luminescence polarization of CdSe microcrystals,” *Phys. Rev. B*, vol. 46, no. 12, pp. 7448–7458, 1992.
- [43] A. Efros and A. Rodina, “Band-edge absorption and luminescence of nonspherical nanometer-size crystals,” *Phys. Rev. B*, vol. 47, no. 15, pp. 5–7, 1993.
- [44] A. Efros, M. Rosen, M. Kuno, M. Nirmal, D. Norris, and M. Bawendi, “Band-edge exciton in quantum dots of semiconductors with a degenerate valence band: Dark and bright exciton states,” *Phys. Rev. B. Condens. Matter*, vol. 54, no. 7, pp. 4843–4856, Aug. 1996.
- [45] Z. Chen, S. Hellstr, Z. Ning, Z. Yu, and Y. Fu, “Exciton Polariton Contribution to the Stokes Shift in Colloidal Quantum Dots †,” pp. 5286–5293, 2011.
- [46] W. K. Bae, K. Char, H. Hur, and S. Lee, “Single-Step Synthesis of Quantum Dots with Chemical Composition Gradients,” no. 22, pp. 531–539, 2008.
- [47] O. E. Semonin, J. C. Johnson, J. M. Luther, A. G. Midgett, A. J. Nozik, and M. C. Beard, “Absolute Photoluminescence Quantum Yields of IR-26 Dye, PbS, and PbSe Quantum Dots,” *J. Phys. Chem. Lett.*, vol. 1, no. 16, pp. 2445–2450, Aug. 2010.
- [48] D. Cui, J. Xu, G. Paradee, S. Xu, and A. Y. Wang, “Developing PbSe/PbS core-shell nanocrystals quantum dots toward their potential heterojunction applications,” *J. Exp. Nanosci.*, vol. 2, no. 1–2, pp. 13–21, Mar. 2007.
- [49] A. L. Rogach, T. Franzl, T. A. Klar, J. Feldmann, N. Gaponik, V. Lesnyak, A. Shavel, A. Eychmuller, Y. P. Rakovich, and J. F. Donegan, “Aqueous Synthesis of Thiol-Capped CdTe Nanocrystals: State-of-the-Art,” *J. Phys. Chem. C*, vol. 111, no. 40, pp. 14628–14637, Oct. 2007.

- [50] F. Pinaud, D. King, H.-P. Moore, and S. Weiss, "Bioactivation and cell targeting of semiconductor CdSe/ZnS nanocrystals with phytochelatin-related peptides.," *J. Am. Chem. Soc.*, vol. 126, no. 19, pp. 6115–23, May 2004.
- [51] G. Kalyuzhny and R. W. Murray, "Ligand effects on optical properties of CdSe nanocrystals.," *J. Phys. Chem. B*, vol. 109, no. 15, pp. 7012–21, Apr. 2005.
- [52] S. Kim and M. G. Bawendi, "Oligomeric ligands for luminescent and stable nanocrystal quantum dots.," *J. Am. Chem. Soc.*, vol. 125, no. 48, pp. 14652–3, Dec. 2003.
- [53] W. C. Chan, "Quantum Dot Bioconjugates for Ultrasensitive Nonisotopic Detection," *Science (80-. )*, vol. 281, no. 5385, pp. 2016–2018, Sep. 1998.
- [54] D. V Talapin and C. B. Murray, "PbSe nanocrystal solids for n- and p-channel thin film field-effect transistors.," *Science*, vol. 310, no. 5745, pp. 86–9, Oct. 2005.
- [55] A. Hassinen, I. Moreels, K. De Nolf, P. F. Smet, J. C. Martins, and Z. Hens, "Short-chain alcohols strip X-type ligands and quench the luminescence of PbSe and CdSe quantum dots, acetonitrile does not.," *J. Am. Chem. Soc.*, vol. 134, no. 51, pp. 20705–12, Dec. 2012.
- [56] K. Baheti, J. a Malen, P. Doak, P. Reddy, S.-Y. Jang, T. D. Tilley, A. Majumdar, and R. a Segalman, "Probing the chemistry of molecular heterojunctions using thermoelectricity.," *Nano Lett.*, vol. 8, no. 2, pp. 715–9, Feb. 2008.
- [57] A. Lefrançois, E. Couderc, J. Faure-Vincent, S. Sadki, A. Pron, and P. Reiss, "Effect of the treatment with (di-)amines and dithiols on the spectroscopic, electrochemical and electrical properties of CdSe nanocrystals' thin films," *J. Mater. Chem.*, vol. 21, no. 31, p. 11524, 2011.
- [58] Y. Liu, M. Gibbs, J. Puthussery, S. Gaik, R. Ihly, H. W. Hillhouse, and M. Law, "Dependence of carrier mobility on nanocrystal size and ligand length in PbSe nanocrystal solids.," *Nano Lett.*, vol. 10, no. 5, pp. 1960–9, May 2010.
- [59] H. W. Hillhouse and M. C. Beard, "Solar cells from colloidal nanocrystals: Fundamentals, materials, devices, and economics," *Curr. Opin. Colloid Interface Sci.*, vol. 14, no. 4, pp. 245–259, 2009.
- [60] B.-R. Hyun, Y.-W. Zhong, A. C. Bartnik, L. Sun, H. D. Abruña, F. W. Wise, J. D. Goodreau, J. R. Matthews, T. M. Leslie, and N. F. Borrelli, "Electron

- injection from colloidal PbS quantum dots into titanium dioxide nanoparticles.," *ACS Nano*, vol. 2, no. 11, pp. 2206–12, Nov. 2008.
- [61] S. A. McDonald, G. Konstantatos, S. Zhang, P. W. Cyr, E. J. D. Klem, L. Levina, and E. H. Sargent, "Solution-processed PbS quantum dot infrared photodetectors and photovoltaics.," *Nat. Mater.*, vol. 4, no. 2, pp. 138–42, Feb. 2005.
- [62] A. Bernanose, "The mechanism of organic electroluminescence," *J. Chim. Phys.*, vol. 52, p. 396, 1953.
- [63] A. Bernanose, M. Comte, and P. Vouaux, "A new method of emission of light by certain organic compounds," *J. Chim. Phys.*, vol. 50, pp. 64–68, 1953.
- [64] M. Pope, H. P. Kallmann, and P. Magnante, "Electroluminescence in Organic Crystals," *J. Chem. Phys.*, vol. 38, no. 8, p. 2042, Apr. 1963.
- [65] D. Kabra, L. P. Lu, M. H. Song, H. J. Snaith, and R. H. Friend, "Efficient single-layer polymer light-emitting diodes.," *Adv. Mater.*, vol. 22, no. 29, pp. 3194–8, Aug. 2010.
- [66] W. Smith, *Modern Optical Engineering, 4th Ed.* McGraw-Hill Professional, 2007, p. 764.
- [67] V. L. Colvin, M. C. Schlamp, and A. P. Alivisatos, "Light-emitting diodes made from cadmium selenide nanocrystals and a semiconducting polymer," *Nature*, vol. 370, no. 6488, pp. 354–357, Aug. 1994.
- [68] J. Seo, M. Cho, and D. Lee, "Efficient heterojunction photovoltaic cell utilizing nanocomposites of lead sulfide nanocrystals and a low-bandgap polymer," *Adv. ...*, 2011.
- [69] M. C. Schlamp, X. Peng, and A. P. Alivisatos, "Improved efficiencies in light emitting diodes made with CdSe(CdS) core/shell type nanocrystals and a semiconducting polymer," *J. Appl. Phys.*, vol. 82, no. 11, p. 5837, Dec. 1997.
- [70] J. S. Steckel, S. Coe-Sullivan, V. Bulović, and M. G. Bawendi, "1.3 $\mu\text{m}$  to 1.55 $\mu\text{m}$  Tunable Electroluminescence from PbSe Quantum Dots Embedded within an Organic Device," *Adv. Mater.*, vol. 15, no. 21, pp. 1862–1866, 2003.
- [71] S. Coe, W.-K. Woo, M. Bawendi, and V. Bulović, "Electroluminescence from single monolayers of nanocrystals in molecular organic devices.," *Nature*, vol. 420, no. 6917, pp. 800–3, Jan. 2002.

- [72] J. S. Steckel, S. Coe-Sullivan, V. Bulović, and M. G. Bawendi, “1.3 $\mu\text{m}$  to 1.55 $\mu\text{m}$  Tunable Electroluminescence from PbSe Quantum Dots Embedded within an Organic Device,” *Adv. Mater.*, vol. 15, no. 21, pp. 1862–1866, Nov. 2003.
- [73] L. Qian, Y. Zheng, J. Xue, and P. Holloway, “Stable and efficient quantum-dot light-emitting diodes based on solution-processed multilayer structures,” *Nat. Photonics*, vol. 5, no. September, 2011.
- [74] J. M. Caruge, J. E. Halpert, V. Wood, V. Bulović, and M. G. Bawendi, “Colloidal quantum-dot light-emitting diodes with metal-oxide charge transport layers,” *Nat. Photonics*, vol. 2, no. 4, pp. 247–250, Mar. 2008.
- [75] N.-G. Park, K. M. Kim, M. G. Kang, K. S. Ryu, S. H. Chang, and Y.-J. Shin, “Chemical Sintering of Nanoparticles: A Methodology for Low-Temperature Fabrication of Dye-Sensitized TiO<sub>2</sub> Films,” *Adv. Mater.*, vol. 17, no. 19, pp. 2349–2353, Oct. 2005.
- [76] K. M. Noone, S. Subramaniyan, Q. Zhang, G. Cao, S. a. Jenekhe, and D. S. Ginger, “Photoinduced Charge Transfer and Polaron Dynamics in Polymer and Hybrid Photovoltaic Thin Films: Organic vs Inorganic Acceptors,” *J. Phys. Chem. C*, vol. 115, no. 49, pp. 24403–24410, Dec. 2011.
- [77] K. Y. Yang, K. C. Choi, and C. W. Ahn, “Surface plasmon-enhanced spontaneous emission rate in an organic light-emitting device structure: Cathode structure for plasmonic application,” *Appl. Phys. Lett.*, vol. 94, no. 17, p. 173301, 2009.
- [78] J. Bellessa, C. Bonnard, J. Plenat, and J. Mugnier, “Strong Coupling between Surface Plasmons and Excitons in an Organic Semiconductor,” *Phys. Rev. Lett.*, vol. 93, no. 3, pp. 3–6, Jul. 2004.
- [79] G. I. Koleilat, L. Levina, H. Shukla, S. H. Myrskog, S. Hinds, A. G. Pattantyus-Abraham, and E. H. Sargent, “Efficient, stable infrared photovoltaics based on solution-cast colloidal quantum dots,” *ACS Nano*, vol. 2, no. 5, pp. 833–40, May 2008.
- [80] K. Okamoto, I. Niki, A. Shvartser, Y. Narukawa, T. Mukai, and A. Scherer, “Surface-plasmon-enhanced light emitters based on InGaN quantum wells,” *Nat. Mater.*, vol. 3, no. 9, pp. 601–5, Sep. 2004.
- [81] B.-H. Kim, C. Cho, J. Mun, M. Kwon, T.-Y. Park, J. S. Kim, C. C. Byeon, J. Lee, and S. Park, “Enhancement of the External Quantum Efficiency of a

- Silicon Quantum Dot Light-Emitting Diode by Localized Surface Plasmons,” *Adv. Mater.*, vol. 20, no. 16, pp. 3100–3104, Aug. 2008.
- [82] J. Nelayah, M. Kociak, O. Stéphan, F. J. García de Abajo, M. Tencé, L. Henrard, D. Taverna, I. Pastoriza-Santos, L. M. Liz-Marzán, and C. Colliex, “Mapping surface plasmons on a single metallic nanoparticle,” *Nat. Phys.*, vol. 3, no. 5, pp. 348–353, Apr. 2007.
- [83] Y. Yang, J. Shi, T. Tanaka, and M. Nogami, “Self-assembled silver nanochains for surface-enhanced Raman scattering,” *Langmuir*, vol. 23, no. 24, pp. 12042–7, Nov. 2007.
- [84] A. D. McFarland, M. a Young, J. a Dieringer, and R. P. Van Duyne, “Wavelength-scanned surface-enhanced Raman excitation spectroscopy,” *J. Phys. Chem. B*, vol. 109, no. 22, pp. 11279–85, Jun. 2005.
- [85] X. Gu, T. Qiu, W. Zhang, and P. K. Chu, “Light-emitting diodes enhanced by localized surface plasmon resonance,” *Nanoscale Res. Lett.*, vol. 6, no. 1, p. 199, Jan. 2011.
- [86] H. Becker, S. Burns, and R. Friend, “Effect of metal films on the photoluminescence and electroluminescence of conjugated polymers,” *Phys. Rev. B*, vol. 56, no. 4, pp. 1893–1905, Jul. 1997.
- [87] V. Choong, Y. Park, Y. Gao, T. Wehrmeister, K. Müllen, B. R. Hsieh, and C. W. Tang, “Dramatic photoluminescence quenching of phenylene vinylene oligomer thin films upon submonolayer Ca deposition,” *Appl. Phys. Lett.*, vol. 69, no. 10, p. 1492, Sep. 1996.
- [88] E. Purcell, “Spontaneous emission probabilities at radio frequencies,” *Phys. Rev.*, vol. 69, p. 681, 1946.
- [89] C.-Y. Cho, M.-K. Kwon, S.-J. Lee, S.-H. Han, J.-W. Kang, S.-E. Kang, D.-Y. Lee, and S.-J. Park, “Surface plasmon-enhanced light-emitting diodes using silver nanoparticles embedded in p-GaN,” *Nanotechnology*, vol. 21, no. 20, p. 205201, May 2010.
- [90] J.-H. Sung, B.-S. Kim, C.-H. Choi, M.-W. Lee, S.-G. Lee, S.-G. Park, E.-H. Lee, and O. Beom-Hoan, “Enhanced luminescence of GaN-based light-emitting diode with a localized surface plasmon resonance,” *Microelectron. Eng.*, vol. 86, no. 4–6, pp. 1120–1123, Apr. 2009.

- [91] D.-M. Yeh, C.-F. Huang, C.-Y. Chen, Y.-C. Lu, and C. C. Yang, "Localized surface plasmon-induced emission enhancement of a green light-emitting diode.," *Nanotechnology*, vol. 19, no. 34, p. 345201, Aug. 2008.
- [92] M.-K. Kwon, J.-Y. Kim, B.-H. Kim, I.-K. Park, C.-Y. Cho, C. C. Byeon, and S.-J. Park, "Surface-Plasmon-Enhanced Light-Emitting Diodes," *Adv. Mater.*, vol. 20, no. 7, pp. 1253–1257, Apr. 2008.
- [93] D.-M. Yeh, C.-F. Huang, C.-Y. Chen, Y.-C. Lu, and C. C. Yang, "Surface plasmon coupling effect in an InGaN/GaN single-quantum-well light-emitting diode," *Appl. Phys. Lett.*, vol. 91, no. 17, p. 171103, 2007.
- [94] S. Pillai, K. R. Catchpole, T. Trupke, G. Zhang, J. Zhao, and M. A. Green, "Enhanced emission from Si-based light-emitting diodes using surface plasmons," *Appl. Phys. Lett.*, vol. 88, no. 16, p. 161102, 2006.
- [95] A. Kumar, R. Srivastava, P. Tyagi, D. S. Mehta, and M. N. Kamalasanan, "Efficiency enhancement of organic light emitting diode via surface energy transfer between exciton and surface plasmon," *Org. Electron.*, vol. 13, no. 1, pp. 159–165, Jan. 2012.
- [96] Y. Xiao, J. P. Yang, P. P. Cheng, J. J. Zhu, Z. Q. Xu, Y. H. Deng, S. T. Lee, Y. Q. Li, and J. X. Tang, "Surface plasmon-enhanced electroluminescence in organic light-emitting diodes incorporating Au nanoparticles," *Appl. Phys. Lett.*, vol. 100, no. 1, p. 013308, 2012.
- [97] A. Fujiki, T. Uemura, N. Zettsu, M. Akai-Kasaya, A. Saito, and Y. Kuwahara, "Enhanced fluorescence by surface plasmon coupling of Au nanoparticles in an organic electroluminescence diode," *Appl. Phys. Lett.*, vol. 96, no. 4, p. 043307, 2010.
- [98] K. Murata, S. Cinà, and N. C. Greenham, "Barriers to electron extraction in polymer light-emitting diodes," *Appl. Phys. Lett.*, vol. 79, no. 8, p. 1193, Aug. 2001.

## Chapter 2

### EXPERIMENTAL METHOD

#### 2.1 Materials Used in The Thesis

Three kinds of solution-processed materials were used in this thesis: conjugated fluorescent polymer, colloidal PbS quantum dot and colloidal Ag nanoparticles. The fluorescent polymer poly(9,9'-dioctylfluorene-co-benzothiadiazole) (abbreviated as F8BT) and poly(9,9'-dioctylfluorene-co-N-(4-butylphenyl)diphenylamine) (abbreviated as TFB) are purchased from American Dye Source, and the other two nanoparticle materials are all synthesized in our lab.

##### 2.1.1 Polyfluorene Polymer

Polyfluorene is a class of state-of-the-art conjugated polymers that contain the fluorine unit as shown in Figure 2-1(a). The bridged pairs of benzene rings form the major part of the conjugated back bone, and the octyl side-chains help to solubilize the polymer. For the electron-transporting polyfluorene used in this thesis poly(9,9'-dioctylfluorene-co-benzothiadiazole) (F8BT) contains a fluorine unit copolymerized with the benzothiadiazole unit as in Figure 2-1(b). Given the highest occupied molecular orbital (HOMO) and lowest unoccupied molecular orbit (LUMO) to be 5.90 and 3.55 eV respectively, the LUMO level aligns better with cathode work function [1]. Based on its good electron mobility, F8BT is mainly used as electron-transporting polymer. It also has a high fluorescence efficiency of 70% ~80%, offering high fluorescence in polymer LED structure. Poly(9,9'-dioctylfluorene-co-N-(4-

butylphenyl)diphenylamine) (TFB) is a blue emission material with a HOMO and LUMO level of 5.35 and 2.3 eV respectively [2], the HOMO level aligns well with the ITO anode for hole injection. As for most of the polymer materials, its hole mobility is higher than its electron mobility.

In this thesis, the polymer solution is specified in weight per volume concentration. A 4ml amber vial (Fisher Scientific 0339111B) with PTFE-lined cap (Fisher Scientific 0339112B) was used to make the polymer solution in every batch. The amber vial can protect polymer from decomposition due to the ambient UV light, and the PTFE is resistant to the solvent for the polymer. To make the solution, the raw weight of amber vial was first measured on a balance with a precision of 0.1mg, and then the balance is re-zeroed. The polymer is then added into the amber vial by either a spatula or tweezers (more convenient for TFB polymer fiber) while the vial is removed from balance plate, in which way the dropping of polymer out of the vial on the measuring plate is prevented. Adding or removing polymer from the vial is repeated until the desired weight is reached. For polymer solution, two kinds of solvent, chloroform and toluene, are mostly used in this thesis. A 1 ml syringe was used to measure the solvent with desired amount. The solvent is slowly injected from the syringe into the amber vial to prevent any splash of either polymer powder or the solvent. After capping, the vial was vibrated on a mixer (Maxi-Mix I) to fully dissolve polymer in the solution. The general batch sizes are about 2~4ml. For a 1 inch square substrate ~0.5ml solution is required for one spin coating. To remove any dust and impurity in the solution, all liquid solutions are filtered by a 0.2um PTFE filter when they were dispensed onto the substrates before spin-coating.

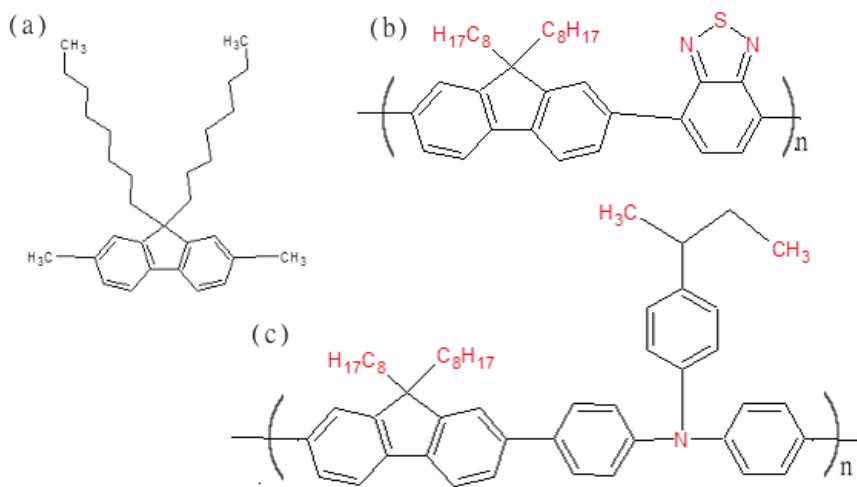


Figure 2-1: Polymer molecular structure. (a) Fluorine unit in polyfluorene. (b) poly(9,9'-dioctylfluorene-co-benzothiadiazole), F8BT. (c) Poly(9,9'-dioctylfluorene-co-N-(4-butylphenyl)diphenylamine), TFB.

### 2.1.2 Colloidal PbS Nanoparticles

Colloidal luminescent quantum dots are a branch of nanomaterials synthesized in solution, and the semiconductor core is capped by a layer of surfactant to ensure their solubility in solvent. The surfactants stabilize the nanoparticles during their growth in solution and finally provide these nanoparticles with good solubility in common solvents.

The synthesis of colloidal nanoparticles generally needs three key components: solvent, organic surfactant and precursor. To initiate the nanoparticle formation, after the reaction solution reaches the proper temperature, the precursor is injected into the solution in a fast manner to ensure all the nucleation happens at the same time to achieve monodispersed nanoparticles. The precursor decomposes or reacts rapidly in the solvent at high temperature to yield saturated monomers. The monomers in

solution quickly undergo nucleation to form nanocrystals, which serve as the seeds in the following nanoparticle grow process.

The surfactants for nanoparticle synthesis typically contain an electron-rich donating group such as phosphine, amines and acids, which will coordinate to electron-poor metal atom at the nanocrystal surface. The other end of solvophilic group will offer the solubility of nanoparticles in solvent.

Controlling the size of nanoparticles is of great importance as it controls the quantum confinement effect for nanometer-scaled materials. Since the quantum dots growth happens in a very fast manner (less than 1 minute) [3], the reaction time is therefore not a very practical way to control the final quantum dot size. Two factors can influence the size of nanoparticles: the injection temperature and the ratio between surfactant and precursor. First, higher temperature results in larger quantum dot sizes as they are more stable under high temperature conditions. Secondly, high concentrations of surfactant can effectively reduce monomer nucleation and therefore reduce the seed concentration. The rest monomer can further supply the growth from the fewer seeds, resulting in larger quantum dots. In contrast, if the surfactant concentration is merely sufficient to provide quantum dot stability, the highly reactive monomer would form a large amount of nucleation sites, resulting in a high concentrations of smaller nanoparticles in the synthesis solution [4].

The PbS quantum dots used in this thesis are prepared using a slightly modified method from Hines *et al.* [3]. The synthesis can be done in a nitrogen purged glove box or in fume hood with the reaction flask purged with nitrogen gas line continuously. A typical synthesis procedure for 1050nm emitting PbS quantum dot includes the following steps. 0.45 g of lead oxide (lead acetate, as the precursor

providing Pb ion in reaction), 10 g of octadecene (ODE, as solvent) and 1.34 g of oleic acid (OA, as surfactant) are added to a three-neck flask and heated to 80 °C for 2 h under vigorous stirring. The reaction flask is connected with a small vacuum pump to keep the flask in a low vacuum condition to degas the mixture. Then, the temperature is kept at 120 °C under nitrogen flow for 30 min before a second solution consisting of 105 µl of hexamethyldisilathiane ((CH<sub>3</sub>)<sub>3</sub>SiSSi(CH<sub>3</sub>)<sub>3</sub>) diluted in 4ml of octadecene is quickly injected into the reaction flask under vigorously stirring. The solution quickly changes from clear into dark brown. After the completion of the reaction, the colloidal PbS nanocrystals are collected by quick injection of the reaction solution into an excess amount of acetone (with a ratio of 1:4) for centrifugation. To ensure adequate removal of the reaction solvents, precipitation and re-dispersion are repeated multiple times. The nanocrystal solution was filtered with 0.2µm PTFE filters.

An IR-26 dye solution with a 0.3 optical density (quantum yield of 0.05%) is used as reference to characterize the quantum dot quantum yield. The IR-26 dye photoluminescence spectrum and intensity is measured using Jobin-Yvon iHR320 triple-grating spectrometer. With the same excitation and collection conditions, the quantum dot solution diluted to 0.3 optical density is measured as well. The quantum dot quantum yield can be obtained from the ratio of integrated PL spectrum from quantum dot and dye.

$$\eta_{QD} = \frac{PL_{int}^{QD}}{PL_{int}^{dye}} \eta_{dye} \quad (2-1)$$

where  $\eta_{QD}(\eta_{dye})$  is the quantum yield of quantum dot (dye) and  $PL_{int}^{QD} (PL_{int}^{dye})$  is the integrated spectrum intensity for quantum dot (dye). Figure 2-2 shows the TEM images of different sizes of PbS nanocrystals synthesized by changing the amount of

oleic acid (from 1.34 g to 20 g) used in this procedure, and the tunable emission wavelength from quantum dots with different sizes.

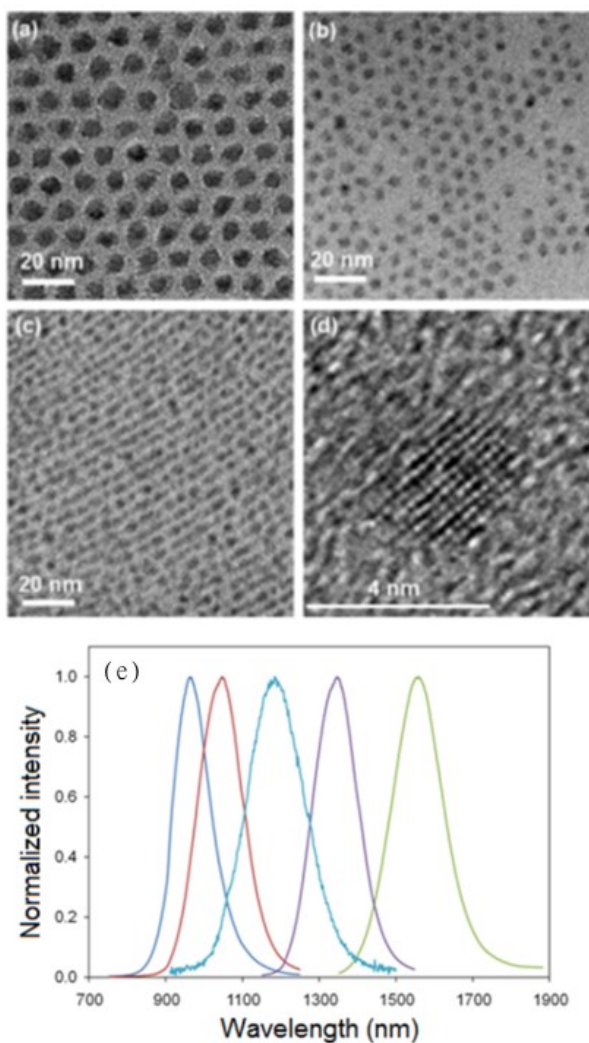


Figure 2-2: Quantum dot TEM and tunable fluorescence spectrum. (a) 7 nm, (b) 5 nm and (c) 3.5 nm PbS colloidal nanocrystals observed under TEM. (d) Lattice structure of a single 3.5 nm nanocrystal under high-resolution TEM (HRTEM). [2] (e) Tunable emission from different sizes of quantum dots due to the quantum confinement effect. [5]

Besides TEM measurements, the absorption spectrum of pristine untreated quantum dot films can also tell the quantum dot size information by the first absorption peak position using the following equation [4]:

$$E_0(\text{eV}) = 0.41 + \frac{1}{0.0252d^2 + 0.283d} \quad (2-2)$$

where  $E_0$  is the first absorption peak position and  $d$  is the quantum dot diameter in nm.

To characterize the quantum dot solution concentration, a given solution is diluted until its absorption does not saturate the UV-Vis spectrometer. The dilution ratio  $r$  is recorded for the calculation. With the solution absorption measurement, the quantum dot concentration was obtained using Beer's law ( $A = c \times \varepsilon \times l$ , where  $A$  is absorption coefficient,  $c$  is molar concentration,  $\varepsilon$  is the molar extinction coefficient [6] at the given quantum dot size and  $l$  is the sample's path length (10mm cuvette). The original solution concentration is obtained just by multiply the results with the dilution ratio  $r$ . The molar extinction coefficient  $\varepsilon_{400}$  at 400nm has a cubic size dependence [6]:

$$\varepsilon_{400} = (0.0233 \pm 0.0001)d^3 \text{ cm}^{-1}/\mu\text{M} \quad (2-3)$$

where  $d$  is the diameter of the quantum dots. This equation gives the most convenient and accurate way for quantum dot concentration characterization.

### 2.1.3 Silver Nanoparticle Synthesis

The mono-dispersed silver nanoparticles used in this thesis are synthesized in organic solvent with oleylamine using a method reported by Hiramatsu and Osterloh [7]. First, 25mg of silver acetate ( $\text{Ag}(\text{OAc})$ ) is dissolved in 2g of oleylamine. To facilitate the dissolution of  $\text{Ag}(\text{OAc})$ , a short term low temperature heat or ultrasonic can be applied on the solution vial. But care needs to be taken to avoid heat or

ultrasonic the solution for long term. Otherwise the Ag(OAc) will start to decompose in the oleylamine since the oleylamine not only works as the surfactants but also serve as the reducing agent for silver acetate to form silver nanoparticles. For synthesizing 9nm diameter nanoparticles, toluene is used as the reaction solvent. The solvent is heated to its boiling temperature and refluxing with a condenser. After quick injection of the Ag(OAc) oleylamine (C<sub>18</sub>H<sub>37</sub>N) solution into the refluxing toluene, the mixture slowly turn from transparent to yellow, orange and then dark brown as the reaction proceeded. Then the heat was kept for 8 hours for reaction to continue. It has been noticed that shorter reaction time like 2~3 hours results in large size distribution, while longer reaction time generates nanoparticles prone to aggregate. The reaction solution is then moved into a clean beaker and left in a fume hood to concentrate to about 10ml. 50ml of methanol was added to the concentrated solution followed by centrifuge to precipitate the nanoparticles and remove reaction residues. For the next round of precipitation, the nanoparticles are dissolved in 10ml of hexane and the followed by adding 40ml of methanol before centrifuge. After the second time precipitation, the solid is re-dissolved in 5ml of hexane and transferred to a small vial with known weight measured in advance. The vial was left in fume hood or vacuum without cap to dry all the solvent. After fully dry of the solid, the net weight of the vial is measured again to obtain nanoparticles weight. Finally, the nanoparticle is re-dissolved with a certain amount of hexane to obtain a desired concentration in the same vial. Low concentration solution is obtained by diluting from its high concentration solution.

## 2.2 Device Structure

### 2.2.1 General Device Structure and Design Requirements

Generally, these novel organic and quantum dot materials based devices consist of a sandwich structure where the thin active films are sandwiched between two electrodes as in Figure 2-3 (a). These devices are surface emitters, so they require one of the electrodes to be transparent. In this thesis, indium tin oxide (ITO) is used as the transparent anode. Recent developments show several promising alternatives for transparent electrodes like metal oxides [8], highly-conductive transparent polymers [9], silver nanowires [10] as well as single-layer graphene [11]. Despite the benefits from these new transparent materials, these techniques are still not mature and less accessible. ITO remains the most common transparent electrode and has been used extensively in industry for liquid crystal display applications. ITO can be deposited by sputtering on glass or plastic substrate, forming a transparent anode layer. But the sputtered ITO generally has a surface roughness on the scale of several nm to 10 nm. The spikes on the ITO surface can create “hot spot” of electrical field which poses a risk of piercing the device layer [12]. Therefore, a thin conductive polymer layer is usually deposited on ITO first before any other organic layers deposition. PEDOT:PSS (poly(ethylene dioxythiophene) doped with poly(styrene sulphonic acid)) polymer blend is the standard choice to limit the influence of anode roughness because of its suitable work function and water-based processability. PEDOT:PSS has a work function of 5.0~5.1eV, slightly higher than the work function of the ITO layer. The alignment of PEDOT:PSS layer with ITO greatly facilitates hole injection from the anode. Meanwhile, given the fact that PEDOT:PSS is water based, any additional polymer layer deposition from organic solvent would not impact the property and/or

morphology of the PEDOT:PSS hole-injection layer. Deposition of PEDOT:PSS layer not only renders a smooth surface for the following organic solvent based material deposition, but also blocks oxygen ions diffusion from the ITO anode to the active material which causes degradation [13]. The PEDOT:PSS used in this paper is PVP Al 4083 purchased from CLEVIOS™.

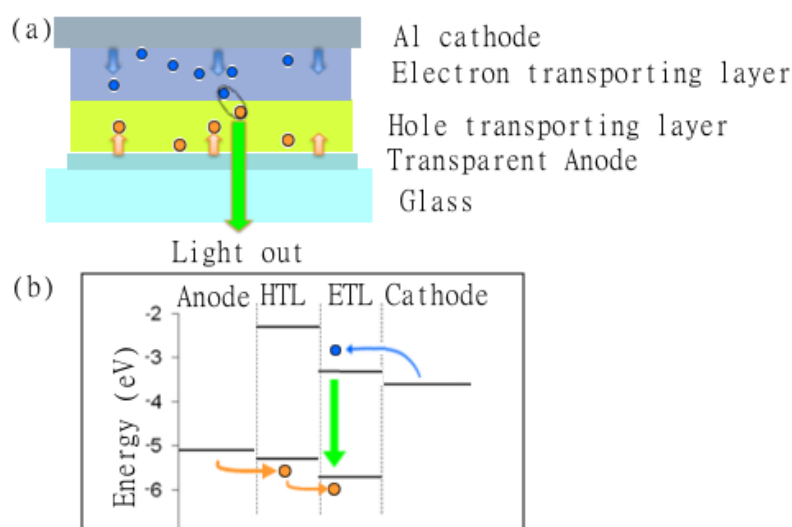


Figure 2-3: Organic light emitting device structure. (a) A sketch of general LED structure (b) the band alignment with in the structure given in (a).

The active region following PDOT:PSS is the place where charge transport, recombination and emission take place. The active region generally contains electron- and hole-transport materials to facilitate the carrier injection into the device as in Figure 2-3 (b). Since most of the polymers are mutually soluble in common solvents, fabricating multi-layer structure using polymer materials becomes challenging. Thus, utilizing the phase separation in polymer blend becomes a convenient way of forming

bulk heterojunction in polymer optoelectronics devices, and are investigated and discussed in chapter 3 in this thesis.

But for light emitting device, a layered structure is generally preferred over bulk heterojunction structure. First, in a layered structure, each carrier transport material can be placed adjacent to its preferred electrode, forming a continuous carrier injection path. Then, the electron and hole meet at the center of the device structure so that the exciton generation region is confined away from electrode where exciton quenching rate is very high due to the high carrier density and cathode surface plasmon coupling [14], [15]. For nanoparticles with oleyamine and oleic acid capping molecule, they can not only dissolve in organic solvent like toluene, but also dissolvable in non-polar organic solvent like hexane in which polymer have very low solubility. Therefore, hexane can be used as an orthogonal solvent to deposit nanoparticle layer on top of polymer layer, forming a real bi-layer structure.

After finishing the spin-coating of active layers, a metal cathode is deposited on top to inject electron into active layer. As most of this novel solution based materials have a very low carrier mobilities, a good conduction band alignment between cathode and electron transporting layer becomes a critical requirement to ensure good electron injection and reach balanced electron and hole densities. Figure 2-3(b) gives a general band structure alignment in an LED structure. Low work function metals such as calcium and magnesium are better suited than Al, Ag and Au. But the chemical reactivity of these alkaline earth metal electrodes reduces the stability of the devices.

## 2.2.2 Device Layout

The substrate consists of a 1 inch square glass substrate and a transparent ITO layer as the anode, the ITO stripe extending from top to bottom and has a width of 1mm or 5mm. The active solution processed material covers the whole substrate surface. The cathodes are patterned as 1mm strip conjunct with the ITO substrate, and the overlap area between cathode and anode defines the active device area as show in Figure 2-4.

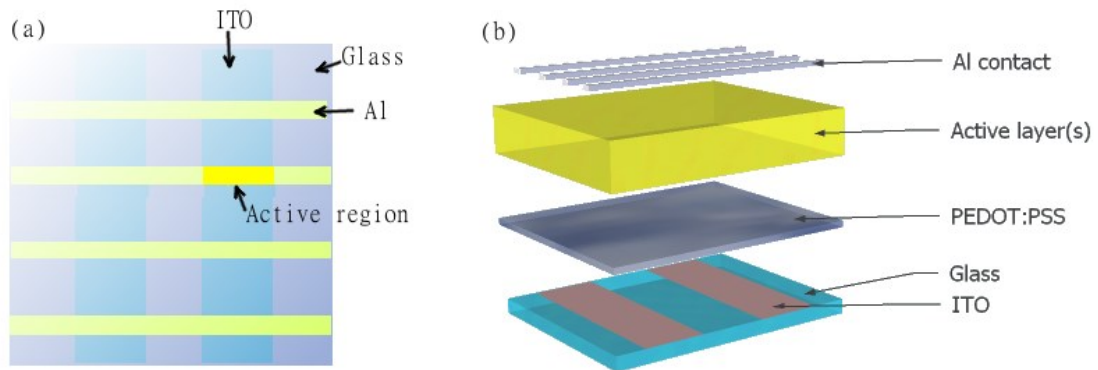


Figure 2-4: Diagram of the device layout. (a) top view through the glass. (b) side view of each layer in the device.

## 2.3 Device Fabrication Methods Used in This Thesis

### 2.3.1 ITO Deposition and Patterning

First, the ITO layer can be deposited on any substrate by radio frequency (RF) sputtering. If using DC sputtering system for less conductive or insulating target, the positive charge will build up on the target, which would increase the voltage required for sputtering. RF sputtering uses alternating potential to avoid the charge build-up, and therefore is good for sputtering insulator and less conductive materials. For our

ITO electrode sputtering process, a commercial Denton Vacuum Discovery 18 Deposition System is used, as shown in Figure 2-5. Cathode number 1 indicated on the machine is used for RF sputtering and cathode number 2 is used for DC sputtering. We use a 3.0in diameter and 0.25in thick indium tin oxide sputtering target (Alfa Aesar) for the ITO sputtering. To prevent target fragmentation under high voltage and high temperature in the RF sputtering process, the target is bonded on a copper backing plate to enhance the target mechanical strength and thermal conductivity.



Figure 2-5: Denton Vacuum Discovery 18 Sputtering Deposition System

The first stage mechanical pump can pump the chamber vacuum down to  $1.5 \times 10^{-1}$  torr, and next the turbo pump can further bring the chamber vacuum down to  $10^{-6}$  torr to  $10^{-7}$  torr if the system is left pumping overnight. After the system reaches the desired vacuum, a 20 sccm Argon gas flows into the chamber. The chamber pressure will rise to  $10^{-3} \sim 10^{-2}$  torr. For RF sputtering of ITO, we turn on the RF power supply at 100W. Once the plasma is struck, we adjust the RF matching controller to reach impedance match so that the reflected power read can be as close to 0W as possible. The target is struck for 30-90 seconds before opening the cathode shutter to cleanup

any contamination on the target surface. In our measurement, 40min deposition without substrate heating results in a very smooth ITO cover at a resistance of 50~60  $\Omega/\square$ . The surface roughness can be as low as 2~3 nm. To pattern the ITO substrate, a shadow mask can be placed on glass substrate to form the anode pattern as given in Figure 2-4.

Some of the devices in the thesis were fabricated on commercial high conductivity (15-20  $\Omega/\square$ ) ITO substrates (CG-61IN) from Delta-technology. To pattern the glass fully covered by ITO, photolithography followed by chemical etching is applied. A negative photo-resist (S1813), which provides better resist to following HCl solution, is used for the photolithography. With the patterned photoresist, the substrate is immersed in 20% hydrochloric acid water solution to etch away the exposed ITO. An etching of 30~40min is required for CG-61IN to fully remove the ITO. After etching, the photoresist can be easily rinsed away by acetone. To thoroughly clean the substrate and remove any organic residue, the substrate is first immersed in acetone and ultrasonicated for 10 minutes. After drying with a filtered nitrogen gun, the substrate is immersed in an isopropanol ultrasonic bath for 10 minutes, and then dried using the nitrogen gun. The patterned substrates were left in a 70°C hot oven for 8 hours to completely remove any residual moisture and solvent traces.

### **2.3.2 Spin-Coating**

Despite the different active materials used in this thesis, they are all solution based and are deposited through spin-coating technique. Spin-coating is a low cost and high throughput thin film deposition method that is widely used in industry. During spin-coating, the substrate is held on the rotating stage by low vacuum, and the

material solution is dropped to cover the whole surface of the substrate, then the rotating stage starts to spin at a speed (200~7000 rpm) and time duration programmed beforehand. During the spinning process, the solution is pushed to the edges of the substrate. With a fast evaporation of the solvent, the residual polymer forms a thin layer on top of the substrate. By controlling the solution concentration and spin coating speed, the final film thickness can be adjusted. For low boiling temperature solvents (like hexane, chloroform), a spin time of 40~60s was used and for high boiling temperature solvent (like toluene and water) a spin time of 90~180s was used to ensure a complete drying of the thin film after spinning. Figure 2-6 shows the spin-coating process.

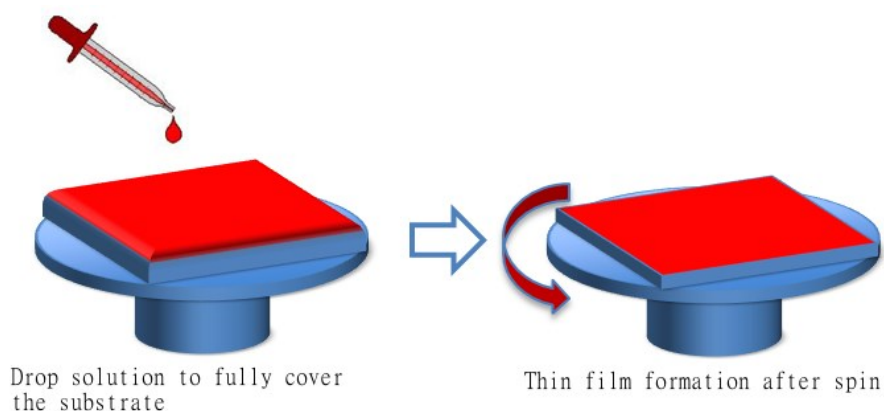


Figure 2-6: Sketch of spin-coating process.

### 2.3.3 E-beam Evaporation of Al Cathode

DC sputtering and e-beam evaporation can both be used for metal electrode deposition. With DC sputtering, the metal atom spray generated by plasma gas bombardment contains high kinetic energies that can bring substantial damage to the

soft polymer materials. Unstable device current, low break-up voltage and high chance of device short are observed on devices with sputtered cathode, and much reliable device performance are observed on devices with evaporated cathode. Therefore, in this thesis, device cathode contacts are all deposited by e-beam evaporation.

E-beam evaporation is one kind of physical vapor deposition (PVD), which is commonly used for high quality and controlled thickness thin film deposition. The evaporation takes place in chamber with high vacuum to remove impurity in air and prevent reaction of high temperature material with any air composite. A mechanical pump is first used to bring the chamber vacuum to  $10^{-2} \sim 10^{-3}$  torr, and then followed by a cryo pump to bring the vacuum down to  $10^{-6} \sim 10^{-7}$  torr. Figure 2-7 (a) shows the sketch of an e-beam evaporation system. Inside the chamber, a boat seated at the bottom of the chamber containing the deposition material is heated up by accelerated electron beam to its boiling or sublimation temperature. The vaporized material atoms travel upwards to the sample substrate, which is facing down and located at the top of the chamber. The low temperature substrate surface causes the material atom to condense and accumulate, forming a thin film on top. A shadow mask is covered on top of the substrate to define the pattern of cathode electrode of the LED device. The deposition rate can be controlled by the e-beam power. For the thickness control, a quartz crystal thickness monitor is mounted next to the sample substrate. A source shutter is used to accurately stop the deposition at the desired thickness. For Al contact used in our devices, a thickness of 100~150 nm is generally used and the deposition rate is controlled at 1~3Å/s.

The e-beam evaporator in the DuPont Hall cleanroom has a bell chamber, which can load 16 pieces of 5 inch wafer. The metal of Al (Sigma Aldrich,

99.9999%), or Ag (International Advanced Materials, 99.999%) or Au (International Advanced Materials, 99.999%) are loaded into a POCO graphite crucible (13cc or 7cc, Temescal). Figure 2-7 (b) shows the main chamber of the e-beam evaporator, (c) is the control panel for vacuum system, and (d) is the deposition system control panel.

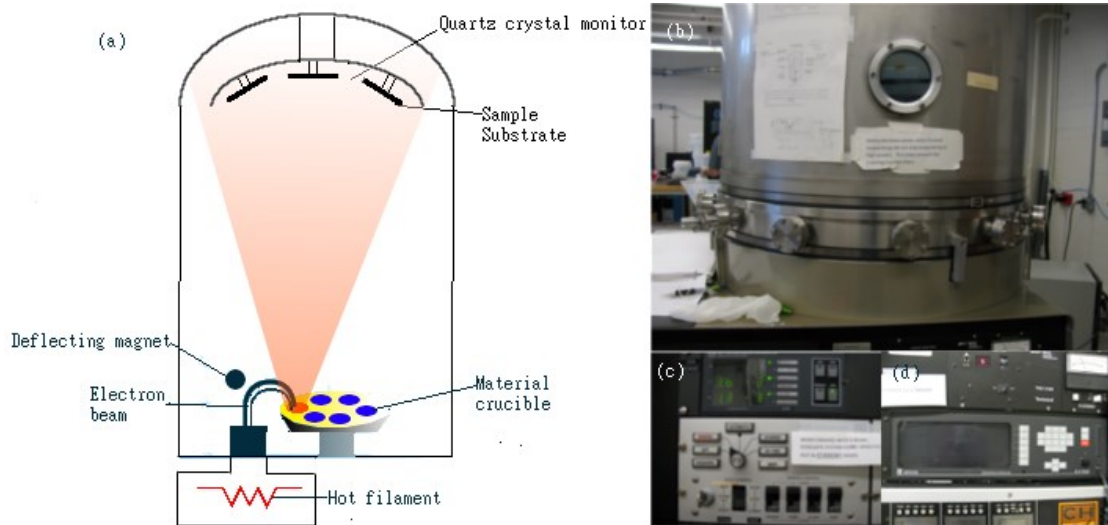


Figure 2-7: Diagram of e-beam evaporator system. (a) Sketch of the e-beam evaporator. (b) the main chamber of the e-beam evaporator (c) the control panel for vacuum system, and (d) the deposition system control panel.

## 2.4 Material and Device Characterization Method

### 2.4.1 UV-Visible Absorption Spectroscopy

Absorption spectrum is a direct method for semiconductor material bandgap measurement. As for semiconductor materials, when the photons passing through the sample have an energy lower than semiconductor band gap, the electrons cannot find an available excited states in the band gap so no absorption occurs. Once the photons have enough energy to overcome the energy gap in semiconductor, electrons would

start to absorb these photon and jump into higher energy states in the conduction band. Therefore, the band gap of a semiconductor material can be determined from the raising edge in absorption spectrum. Optical absorption is a very useful tool for nanoparticle analysis, as it can not only give the average size of the nanoparticle from the main absorption peak, but also identify the film thickness and solution concentration.

For optical absorption measurements, a tungsten lamp passing through monochromator illuminates the sample, and the transmission is recorded while the monochromator scans the illumination wavelength. To remove any effect from the substrate or solvent, baseline calibration is performed with a reference sample. For solution sample, the reference is pure solvent in the same cuvette as the sample used, and for thin film sample a clean substrate without thin film deposition is used as the reference. The absorbance is calculated from

$$A = -\log_{10}T = -\log_{10}\frac{I}{I_0} \quad (2-4)$$

where  $T$  is the transmission,  $I$  is the transmitted light intensity and  $I_0$  is the transmitted light with reference sample.

Besides the band gap information, the absorption spectrum can also be used to determine the quantum dot size and solution concentration as discussed in section 2.1.2 above.

This thesis uses a UV–VIS–NIR spectrometer UV-3600 from Shimadzu for the absorption measurements on solution and transparent thin films. But since this setup only measures the transmitted signal, it is not applicable for a non-transparent samples or samples with strong scattering. For those samples, diffuse reflectance absorption is measured on a Perkin Elmer Lambda 35 UV–VIS Spectrophotometer. Different from

the transmittance measurement setup, diffuse reflectance absorption collects the reflected light using an integrating sphere, so all the scattered light is collected and a true absorption is deducted from the results. Figure 2-8 shows the configuration for a diffuse reflectance measurement. The reference sample is obtained by putting a standard white Lambertian diffusing surface at the sample position.

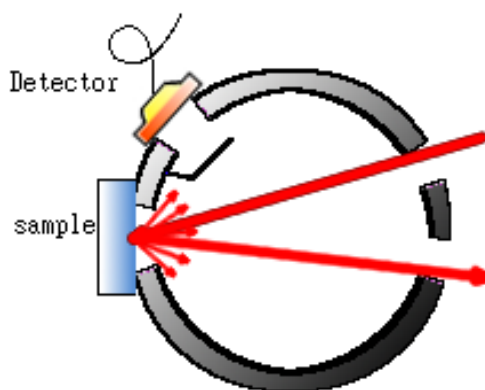


Figure 2-8: Diffused reflectance absorption measurement setup.

#### 2.4.2 Steady-State Photoluminescence and Electroluminescence Spectroscopy

For photoluminescence (PL), a laser in the range of the material absorption spectrum is used to excite the sample. The material absorbs high energy photons from the excitation laser, during which process the electrons are pumped into high energy levels in the conduction band and then relax to the bottom of the conduction band through a fast non-radiative process. With a certain exciton lifetime, the exciton releases a low energy photon and relaxes back to the ground state. The released photon generally has a lower energy than the actual band gap of the semiconductor because a portion of the energy is lost to the exciton binding process (exciton binding energy),

which is especially large in organic materials due to the associated distortion of the molecule. The photoluminescence spectroscopy can be used not only to determine the PL spectral shape, but also the relative and absolute quantum yields by comparing the integrated spectral intensity with a material of known quantum yield, like an organic dye. To record the spectrum, a Jobin–Yvon iHR320 triple-grating spectrometer equipped with a Synapse silicon CCD array (for the visible spectrum) and a Symphony thermoelectric-cooled InGaAs CCD array (for the near-infrared spectrum) are used. The excitation laser can be a 250mW 532 nm frequency-stabilized TORUS laser from Laser-Quantum Inc, a CW 405 nm laser diode or a 337 nm pulse UV laser dependent on the material absorption in this thesis.

For electroluminescence (EL) measurements, the sample is put at the same position as for photoluminescence measurements so that the maximum coupling efficiency to the spectrometer can be assured for light collection. Instead of using a 532nm laser, the excitons are generated by current injection. For a device structure consisting of layers of fluorescent material with different emission spectrum, the EL spectrum will depend on the place where excitons form and recombine. Therefore, EL spectrum can provide importance information for device design. Meanwhile, the EL spectrum determines the color purity and brightness of the device emission. Luminance efficiency of a device is calculated using EL spectrum as will be introduced in Section 2.4.8. A Keithley 236 source-measure unit is used to drive the device electrically.

This thesis also uses a Witec confocal Raman microscope system for confocal fluorescence measurements. The sample is excited under microscope and the fluorescence signals are collected by the 100X objective which offers ~300nm spatial

resolution. The collected signal is coupled to a spectrometer for spectral analysis. This can allow the detailed examination of phase separation on fluorescent thin films formed by blended materials.

### 2.4.3 Time-Resolved Photoluminescence Measurements

Time-resolved PL (TRPL) measurements can yield the exciton lifetime by using an ultrafast laser pulse to excite the sample and an avalanche photodiode to detect the emission intensity decay in a certain wavelength window. Using TRPL, the exciton lifetime can be determined by fitting the exponentially decaying curve.

$$I = I_0 \exp\left(-\frac{t}{\tau}\right) \quad (2-5)$$

$$\tau = \frac{1}{k_r + k_{nr}}$$

where  $\tau$  is the exciton life time,  $k_r$  and  $k_{nr}$  are the radiative and non-radiative decay rates.

For time-resolved photoluminescence (TRPL) measurements, excitation at 400 nm is achieved by frequency doubling a Mira-900 laser. The laser pulses are approximately 150 fs in duration and emitted at a repetition rate of 80 MHz. A pulse picker is used to reduce the repetition rate for sample excitation to 151 kHz. The fluorescence signal is detected using a Perkin–Elmer avalanche photodiode with a PicoHarp time correlated single photon counting system. The spectral bandwidth of the system is 20 nm and the temporal resolution is 300 ps. The time-resolved photoluminescence data are fitted using the FluoFit analysis software from PicoQuant.

#### **2.4.4 Transmission Electron Microscopy**

Transmission electron microscope (TEM) is used to obtain the image of nanoparticles and analyze their average size, size distribution and ligand length. TEM is a microscopy technique using electrons instead of photons for sample observation. Electrons have a small de Broglie wavelength on the order of tens of pm. This short wavelength offers electron microscopes much higher resolution than optical microscopes. In TEM, the electron beam transmits through the ultra-thin sample, interacts with the sample and is finally projected on an imaging device. Due to the low penetration depth of electrons, the samples need to be made ultra-thin and sit on special grids so that the electron can pass through. TEM images are obtained using a JEM 2010F instrument at an acceleration voltage of 200 keV in this thesis.

#### **2.4.5 Scanning Electron Microscopy**

Scanning electron microscopy (SEM) also use electrons as the imaging medium[16]. Unlike TEM, SEM collects the reflected electrons thus does not require the sample to be ultrathin. A focused electron beam whose diameter defines the resolution of imaging is rastered across the sample. The electrons interact with the sample and secondary electrons are re-emitted with information about surface topography and composition. SEM can offer a resolution of <1nm to 20nm depending on the instrument, the energy of the electrons and the electro-optical system. Despite its lower resolution compared with TEM, SEM can be used to image bulk materials with no limitation on sample thickness. It is therefore more suitable and convenient for surface morphology measurements and can be used on organic thin films, which are difficult to image under TEM due to the low contrast. But using SEM on organic sample is still more challenging than on high-conductivity samples. Due to the low

conductivity of organic materials, electron charging on sample surface can reduce the image contrast. For SEM observation, a relatively thin film is usually deposited on highly conductive surface like ITO or Al, and a quick scan is performed to prevent charge accumulation on the thin film's surface. SEM images are obtained using a JSM-7400F field-emission SEM instrument operating at an acceleration voltage of 3 kV.

#### **2.4.6 Atomic Force Microscopy**

Atomic force microscopy (AFM) is a scanning probe microscopy technique that measures nanoscale surface morphology based on the atomic force between tip and sample's surface. When the tip is in proximity with the surface, the interaction force will cause a deflection of the cantilever measured by a laser spot reflected from the top surface of the cantilever into a 4 phase photodetector. A piezo stage moves the sample in x-y plane to enable surface scan. Due to the rough surface on most of the sample, there is a high risk of tip-surface collision if it seat at a constant height. Therefore, the z direction piezo stage with a feedback mechanism is used to adjust the distance and maintain a constant force between sample and tip. Besides the sample surface morphology, additional information like local conductivity and thermal property can be extracted from the sample by using specialized tip.

Conductive AFM is a variation of AFM used in this thesis to measure the local conductivity in polymer films. A voltage is applied on a tip (ElectriCont-G, Budget Sensors) coated with platinum. The current flowing through the loop formed by the tip and conductive samples is recorded simultaneously with the topography of the samples. Therefore, a correlation between surface spatial features and conductivity can be obtained.

The platinum coated on the tip has a high work function, which facilitates hole injection into the polymer material. The polymer thin film is deposited on an Al coated silicon substrate, thus the Pt/polymer/Al forms a good band alignment for the electrons to flow from the Al into the probe, and for holes to flow from the probe into the samples. This is why a negative voltage is always applied on the sample holder. To ensure a good contact between the sample holder and Al electrode, a silver paste is used to connect the Al with the metal sample holder.

Since the voltage induces a high electrical field at the tip contact point with sample surface, the tip degrades with time due to the accumulation of OH<sup>-</sup> ion formed from the ionized water and contaminants on the sample's surface. The degradation of the tip will cause low conductivity and low resolution on morphology measurements after a long period.

In tapping mode AFM, the cantilever is oscillating up and down at a frequency near cantilever resonance. The oscillation amplitude is in the range of 100nm to 200nm. A feedback servo is used to control the height of the cantilever above the sample so that the tip is "tapping" the surface at a constant force. Tapping mode can reduce the damage to the surface and tip compared to contact mode. A Dimension 3100 V (Digital Instruments) is used for the AFM images in this thesis.

Compared with SEM, AFM gives more detailed information and a real 3D morphology and topographic information of the surface. SEM shows a two-dimensional image of the sample without the surface roughness range. Meanwhile, for low-conductivity samples like the polymer and quantum dot thin films in this thesis, charging can still happen and cause low image contrasts or even damage on thin polymer films. In contrast, AFM can be performed in atmosphere without vacuum or

special sample preparation procedures like metal sputtering for low-conductivity material in SEM. But an AFM scan is generally much slower than an SEM scan and subject to image drifting for large area scans.

#### **2.4.7 Film Thickness Measurements**

There are two instruments that we used to measure film thicknesses: Dektak II surface profilometer or tapping mode AFM. To prepare samples for thickness measurements, the thin films are scratched by a sharp blade to create a clean step on the film. The film thickness is estimated by measuring the step depth by profilometry or tapping mode AFM.

The Dektak II surface profilometer measures a step by drags a diamond tipped stylus across the measuring surface. The surface roughness causes the stylus to move up and down, which is measured and recorded electrically. The measurement has a height range of 10 nm to 66 $\mu$ m, and a resolution of 10nm.

Tapping mode AFM can give more accuracy and higher resolution (1 nm) for films with a low thickness. For thicknesses below 50 nm, tapping mode AFM is used for thickness measurements in this thesis. The details of tapping mode AFM measurements are introduced above in Section 2.4.6.

#### **2.4.8 Device PIV Characterization**

The most basic and important test on a LED is the power-current-voltage scan. The device efficiency is calculated based on this information. A computer-interfaced Newport power meter (818-SL/CM silicon detector) and a Keithley 236 source-measure unit, combined with a 2 inch integrating sphere form the luminance-current-voltage measurement system. Figure 2 -9 shows the basic setup.

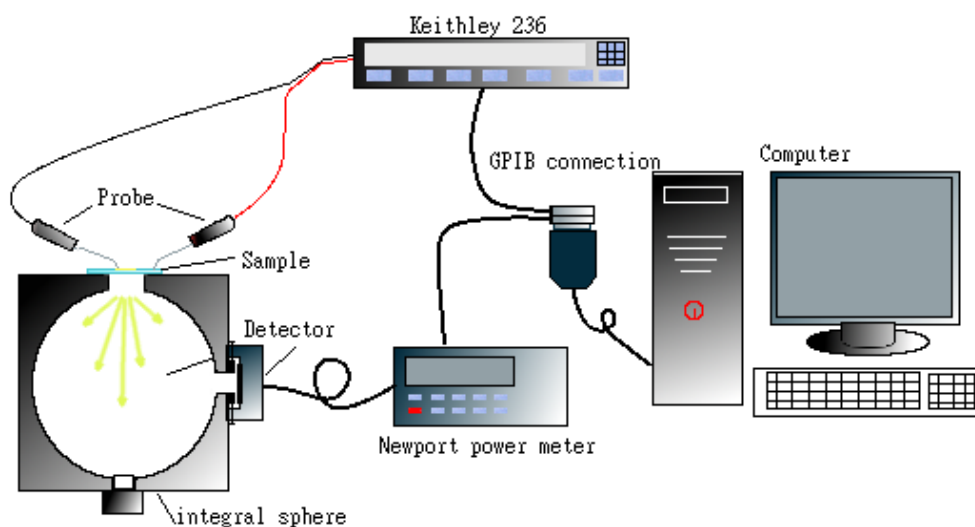


Figure 2-9: Power-current-voltage measurement setup configuration.

Current-voltage generally follows a power law in semiconductor materials. To obtain information about the conductivity mechanisms in organic thin films, the IV curve is plotted in log-log scale. Log-log scale can convert the power law into simple linear relationships, and the power is given by the slope of the fit to identify the transport mechanisms. A slope  $n=1$  suggests an ohmic conduction, while  $n=2$  is characteristic of a space-charge limited conduction in organic materials and  $n>2$  is characteristic of trap-limited conduction [17].

The output power of the device is measured by integrating the total output intensity through a calibrated integrating sphere. To calibrate the integrating sphere, a known efficiency white LED is put on the entrance port and the power is measured by the Newport detector (silicon for visible and germanium for near IR). The power readout is converted into external quantum efficiency by:

$$EQE = \frac{n_{photon}}{n_{electron}} = \frac{power/E_{photon}}{I/q} \quad (2-6)$$

where  $E_{photon}$  is the known photon energy  $hc/\lambda$  in which we use the fluorescence peak wavelength  $\lambda_{peak}$  for calculation,  $I$  is the current and  $q$  is the electron charge. The measured efficiency is compared with the known device efficiency to obtain the integrating sphere collecting coefficient. Besides the external quantum efficiency, current luminance efficiency is also a very important parameter since it reflects the brightness of the light source to the human eye. The human eye has a sensitivity curve spectrum shown in Figure 2-10, and it is also known as luminosity function.

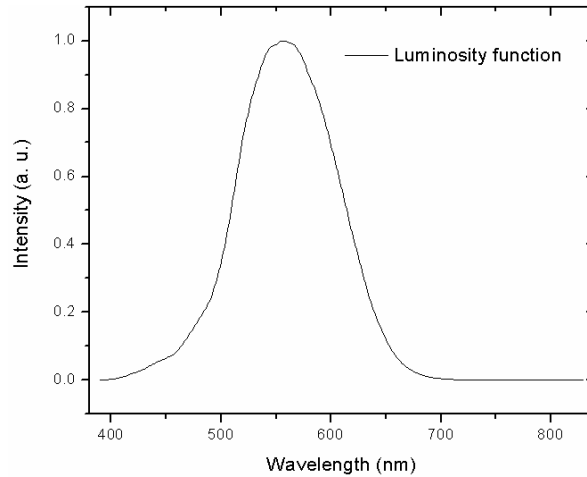


Figure 2-10: Standard luminosity function [18].

The light source brightness, luminance, is quantified by the unit candela (cd). To convert the output power (W) into luminance (cd), the following equation is used [19]:

$$I_v = \frac{683.002}{2\pi} P_{out} \int_{380}^{780} \overline{EL(\lambda)} \times \overline{E_{photon}(\lambda)} \times \overline{y(\lambda)} d\lambda \quad (2-7)$$

where  $I_v$  is luminance in cd,  $P_{out}$  is the output power in W obtained from the integrating sphere,  $\overline{y(\lambda)}$  is the standard luminosity function and  $EL(\lambda)$  is the measured electroluminescence spectrum,  $E_{photon}(\lambda)$  is the photon energy at each wavelength, and  $\overline{EL(\lambda) \times E_{photon}(\lambda)}$  means the multiplied result is area-normalized so that  $\int_{380}^{780} \overline{EL(\lambda) \times E_{photon}(\lambda)} d\lambda = 1$ .  $\overline{EL(\lambda) \times E_{photon}(\lambda)}$  reflects the spectral power distribution.

A current efficiency in cd/A is determined by:

$$\eta_{current} = \frac{I_v}{I} \quad (2-8)$$

and power efficiency in lumens/Watt is determined as:

$$\eta_{power} = \frac{2\pi I_v}{VI} \quad (2-9)$$

where  $V$  is the voltage applied. Power efficiency is more considered in industry since it reflects the power consumption of the LED at a given brightness.

#### 2.4.9 Mobility Measurements

Organic materials and solution processed thin films generally have a much smaller carrier mobility compared with crystalline semiconductors. As such, characterizing the carrier mobility is of significant importance for device engineering, to achieve high efficiency and to understand underlying physics in these materials. Mobility is the speed of charge carrier in a material under unit electric field. It reflects how fast the electron can move around under any driving force. Defect states in semiconductor materials can reduce carrier mobility by causing scattering or trapping of electrons.

For inorganic crystalline material, their large mobilities are generally measured by Hall Effect and conductivity measurements. These techniques are not suitable and

sensitive enough for low-mobility materials. As such, other techniques are exploited for these low mobility materials, including time of flight [20], [21], steady-state trap-free space-charge limited current (steady-state TF-SCLC method) [22], FET method [23], [24], transient EL[25], [26], and charge extraction by linearly increasing voltage (CELIV) [27]–[29]. In this thesis, time of flight and CELIV methods have been used to measure the electron and hole mobilities in quantum dot thin films with different ligand exchange treatments.

#### **2.4.9.1 Time-of-flight**

Time-of-flight is the most common and simple technique for mobility measurements in small organic molecules and polymer thin films [30]–[32]. In time of flight measurement, the thin film is fabricated between two electrodes, one of which is transparent. Figure 2-11 demonstrates the measurement setup schematics. During the measurement, a pulsed laser is used to excite the material through the transparent electrode. The photo-generated carriers located near the transparent electrode will start to drift towards the opposite electrode under the driving electric field. The applied voltage dependence needs to be measured carefully. The transparent electrode is held at a positive potential with respect to the ground for hole-mobility measurements, while the negative potential is held for the transparent electrode for electron mobility measurements. The drifting carriers result in a current equal to  $NeV/d$ , where  $N$  is the number of charge carriers in the material,  $e$  is the elementary charge,  $d$  is the film thickness, and  $V$  is the velocity. When the sample is first excited, a current spike is created due to the large density of carriers. Then, a relatively stable constant current will be measured as the photo-generated carriers travel through the material. Finally,

the current will rapidly decrease to zero as the photo-generated carriers all reach the opposite electrode.

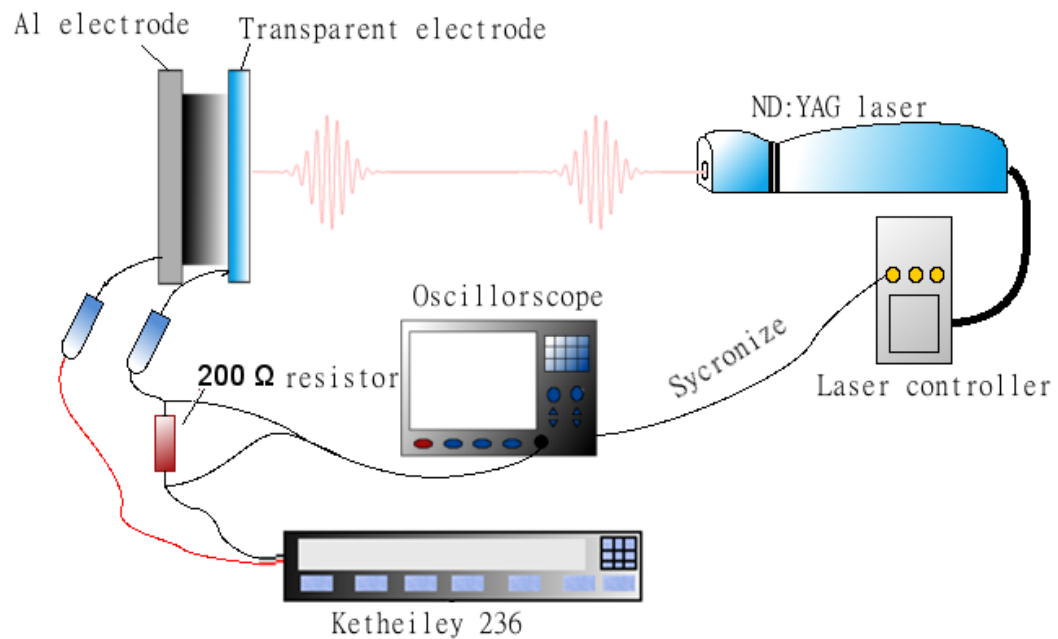


Figure 2-11: Time-of-flight setup configuration

To clearly identify the transit time  $t$ , the excitation laser pulse needs to have a width shorter than the transit time and the absorption depth should be smaller than the thickness of the sample. Therefore thick samples (prepared in the range from 2~5  $\mu\text{m}$ ) are generally used for time of flight measurements. When the material is not dispersive, a clear cusp can be seen from the current decay curve as in Figure 2-12(a). In contrast, for dispersive materials, a definite cusp cannot be observed in the transit

current plots. In this case, according to Scher-Montroll theory, the transit time  $t$  can be determined from the double logarithmic plot as in Figure 2-12(b).

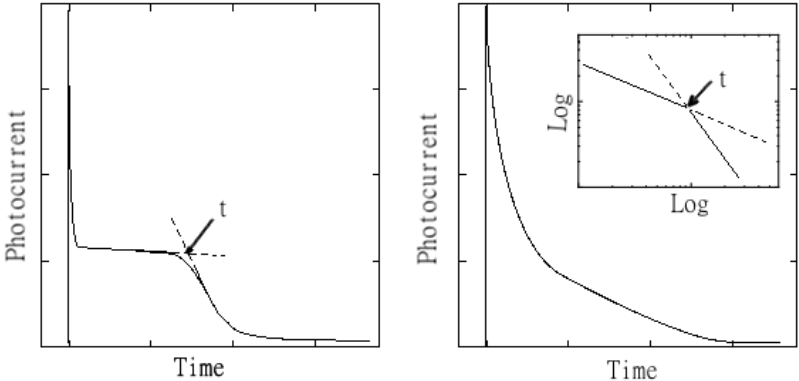


Figure 2-12: Transit current profile in time of flight measurement. (a) Non-dispersive time of flight measurement current decay curve. (b) Dispersive current decay curve. The inset shows the logarithmic plot and transit time  $t$  determined by the slope transit.

With the transit time  $t$  the mobility can be calculated as:

$$\mu = \frac{d^2}{Vt} \tag{2-10}$$

where  $V$  is the constant voltage applied on the sample,  $d$  is the sample thickness measured by profilometer [33].

In this thesis, the 532 nm second-harmonic of a Brilliant Q-switched Nd:YAG laser (Quantel) with 5 ns pulses is used to excite the samples from the ITO side, while a reverse-bias is applied on the sample to extract the photo-generated minority carriers (electrons) to transport through the whole thickness and be collected at Al contact. The transient current is recorded by the voltage drop across a 200 Ohms resistive load by a digital oscilloscope (Agilent 54621A).

### 2.4.9.2 Charge extraction by linearly increasing voltage (CELIV)

Charge extraction by linearly increasing voltage (CELIV) is a measurement technique for majority carrier density and mobility. Comparing with TOF, CELIV does not require a transparent electrode and ultrashort laser pulse. Meanwhile, the sample does not need to be optically thick thus simplifying the sample fabrication.

CELIV is a method based on equilibrium charge carrier extraction. In CELIV, a triangular voltage with a linearly increasing edge is applied to the sample. As the depletion depth increases, the extracted equilibrium charge form a current of: [28]

$$j(t) = \frac{\varepsilon\varepsilon_0 A}{d} + \frac{\sigma}{\mu} \left(1 - \frac{l(t)}{d}\right) \left(\frac{\mu A t}{d} - \frac{\sigma}{2\varepsilon\varepsilon_0 d} l^2(t)\right) \quad (2-11)$$

(Detailed derivation and symbol meanings can be found in ref [28].) Figure 2-13 gives the typical measurement result from CELIV, the conductivity and mobility can be calculated based on the current intensity  $j(0)$  and transient current maximum delay time  $t_{\max}$  and  $\Delta j/j(0)$ . The conductivities can be calculated directly from the CELIV measurements using:

$$\sigma = \frac{3}{2} \frac{d\Delta j}{t_{\max} A} \quad (2-12)$$

and the hole mobility is calculated according to :

$$\mu_h = \frac{2d^2}{3A t_{\max}^2 (1 + 0.36 \frac{\Delta j}{j(0)})} \quad (2-13)$$

where  $d$  is the sample thickness,  $A$  is the voltage-increase slope. The parameters  $t_{\max}$ ,  $\Delta j$  and  $j(0)$  are obtained directly from the CELIV measurements as shown in Figure 2-13. A linearly-increasing bias is applied by a function generator (Agilent 33220A) 20MHz on the sample and the transient currents are measured by the voltage drop across a 200 Ohms resistive load by a digital oscilloscope (Agilent 54621A).

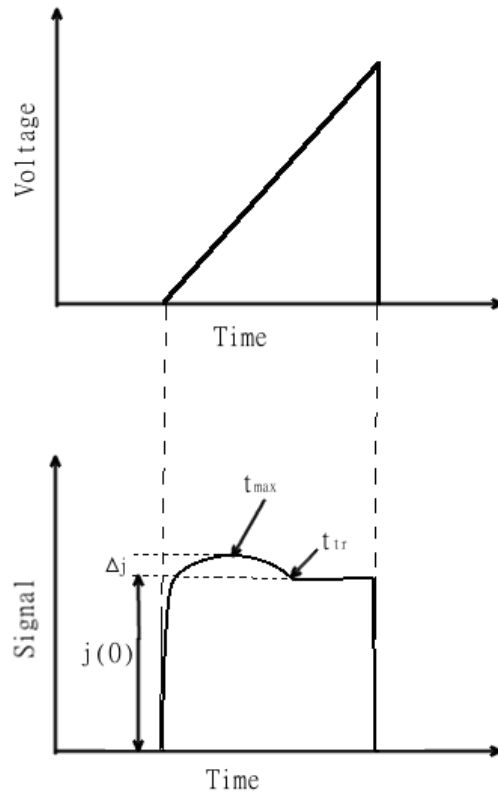


Figure 2-13: CELIV applied voltage and the correspondingly measured current.

## REFERENCES

- [1] T.-W. Lee, J. Hwang, and S.-Y. Min, “Highly efficient hybrid inorganic-organic light-emitting diodes by using air-stable metal oxides and a thick emitting layer,” *ChemSusChem*, vol. 3, no. 9, pp. 1021–3, Sep. 2010.
- [2] X. Ma, F. Xu, J. Benavides, and S. G. Cloutier, “High performance hybrid near-infrared LEDs using benzenedithiol cross-linked PbS colloidal nanocrystals,” *Org. Electron.*, vol. 13, no. 3, pp. 525–531, Mar. 2012.
- [3] M. A. Hines and G. D. Scholes, “Colloidal PbS Nanocrystals with Size-Tunable Near-Infrared Emission: Observation of Post-Synthesis Self-Narrowing of the Particle Size Distribution,” *Adv. Mater.*, vol. 15, no. 21, pp. 1844–1849, Nov. 2003.
- [4] Y. Yin and a P. Alivisatos, “Colloidal nanocrystal synthesis and the organic-inorganic interface,” *Nature*, vol. 437, no. 7059, pp. 664–70, Sep. 2005.
- [5] S. Cloutier, *Advanced Photonic Sciences*, no. 1. InTech, 2012, pp. 178–196.
- [6] I. Moreels, K. Lambert, D. Smeets, D. De Muynck, T. Nollet, J. C. Martins, F. Vanhaecke, A. Vantomme, C. Delerue, G. Allan, and Z. Hens, “Size-dependent optical properties of colloidal PbS quantum dots,” *ACS Nano*, vol. 3, no. 10, pp. 3023–30, Oct. 2009.
- [7] H. Hiramatsu and F. E. Osterloh, “A Simple Large-Scale Synthesis of Nearly Monodisperse Gold and Silver Nanoparticles with Adjustable Sizes and with Exchangeable Surfactants,” *Chem. Mater.*, vol. 16, no. 13, pp. 2509–2511, Jun. 2004.
- [8] H. J. Bolink, E. Coronado, J. Orozco, and M. Sessolo, “Efficient Polymer Light-Emitting Diode Using Air-Stable Metal Oxides as Electrodes,” *Adv. Mater.*, vol. 21, no. 1, pp. 79–82, Jan. 2009.
- [9] F. Croce, G. B. Appetecchi, L. Persi, and B. Scrosati, “Nanocomposite polymer electrolytes for lithium batteries,” vol. 394, no. 6692, pp. 456–458, Jul. 1998.
- [10] Z. Yu, Q. Zhang, L. Li, Q. Chen, X. Niu, J. Liu, and Q. Pei, “Highly flexible silver nanowire electrodes for shape-memory polymer light-emitting diodes,” *Adv. Mater.*, vol. 23, no. 5, pp. 664–8, Feb. 2011.

- [11] N. Li, S. Oida, G. S. Tulevski, S.-J. Han, J. B. Hannon, D. K. Sadana, and T.-C. Chen, "Efficient and bright organic light-emitting diodes on single-layer graphene electrodes.," *Nat. Commun.*, vol. 4, p. 2294, Jan. 2013.
- [12] A. J. A. B. Seeley, "Light-emitting diodes from polyfluorenes: characterisation and stability of performance," Department of Physics, 2003.
- [13] J. Hwang, F. Amy, and A. Kahn, "Spectroscopic study on sputtered PEDOT·PSS: Role of surface PSS layer," *Org. Electron.*, vol. 7, no. 5, pp. 387–396, 2006.
- [14] V. Choong, Y. Park, Y. Gao, T. Wehrmeister, K. Müllen, B. R. Hsieh, and C. W. Tang, "Dramatic photoluminescence quenching of phenylene vinylene oligomer thin films upon submonolayer Ca deposition," *Appl. Phys. Lett.*, vol. 69, no. 10, p. 1492, Sep. 1996.
- [15] H. Becker and S. Burns, "Effect of metal films on the photoluminescence and electroluminescence of conjugated polymers," *Phys. Rev. B*, vol. 56, no. 4, pp. 1893–1905, 1997.
- [16] J. Goldstein, D. E. Newbury, D. C. Joy, C. E. Lyman, P. Echlin, E. Lifshin, L. Sawyer, and J. R. Michael, *Scanning Electron Microscopy and X-ray Microanalysis: Third Edition*. Springer, 2007, p. 690.
- [17] Y. Kim and C.-S. Ha, *Advances in organic light emitting devices*. Trans Tech Publications, 2008.
- [18] D. B. Judd, "Report of U.S. Secretariat Committee on Colorimetry and Artificial Daylight.," *Twelfth Session of the CIE, Stockholm (vol. 1, pp. 11)*, 1951. [Online]. Available: <http://www.cvrl.org/lumindex.htm>.
- [19] V. Bulović, Y. Fink, and P. O. Anikeeva, "Physical properties and design of light-emitting devices based on organic materials and nanoparticles," Massachusetts Institute of Technology, 2009.
- [20] J. Mort and D. M. Pai, "Photoconductivity and related phenomena," p. 502, 1976.
- [21] M. A. Lampert and P. Mark, *Current injection in solids*. Academic Press, 1970, p. 351.
- [22] Z. An, J. Yu, S. C. Jones, S. Barlow, S. Yoo, B. Domercq, P. Prins, L. D. A. Siebbeles, B. Kippelen, and S. R. Marder, "High Electron Mobility in Room-

- Temperature Discotic Liquid-Crystalline Perylene Diimides,” *Adv. Mater.*, vol. 17, no. 21, pp. 2580–2583, Nov. 2005.
- [23] D. V Talapin and C. B. Murray, “PbSe nanocrystal solids for n- and p-channel thin film field-effect transistors,” *Science*, vol. 310, no. 5745, pp. 86–9, Oct. 2005.
- [24] L. M. Andersson, *Electronic Transport in Polymeric Solar Cells and Transistors*, no. 1142. 2007.
- [25] M. Redecker, H. Bässler, and H. H. Hörhold, “Determination of the Hole Mobility in Organic Light-Emitting Diodes via Transient Absorption,” *J. Phys. Chem. B*, vol. 101, no. 38, pp. 7398–7403, Sep. 1997.
- [26] T. C. Wong, J. Kovac, C. S. Lee, L. S. Hung, and S. T. Lee, “Transient electroluminescence measurements on electron-mobility of N-arylbenzimidazoles,” *Chem. Phys. Lett.*, vol. 334, no. 1–3, pp. 61–64, Feb. 2001.
- [27] G. Juška, M. Viliūnas, K. Arlauskas, N. Nekrašas, N. Wyrsh, and L. Feitknecht, “Hole drift mobility in  $\mu\text{c-Si:H}$ ,” *J. Appl. Phys.*, vol. 89, no. 9, p. 4971, 2001.
- [28] G. Juska, K. Arlauskas, M. Viliunas, and J. Kocka, “Extraction current transients: new method of study of charge transport in microcrystalline silicon,” *Phys. Rev. Lett.*, vol. 84, no. 21, pp. 4946–9, May 2000.
- [29] J. Tang, K. W. Kemp, S. Hoogland, K. S. Jeong, H. Liu, L. Levina, M. Furukawa, X. Wang, R. Debnath, D. Cha, K. W. Chou, A. Fischer, A. Amassian, J. B. Asbury, and E. H. Sargent, “Colloidal-quantum-dot photovoltaics using atomic-ligand passivation,” *Nat. Mater.*, vol. 10, no. 10, pp. 765–71, Oct. 2011.
- [30] S. Naka, H. Okada, H. Onnagawa, Y. Yamaguchi, and T. Tsutsui, “Carrier transport properties of organic materials for EL device operation,” *Synth. Met.*, vol. 111, pp. 331–333, 2000.
- [31] A. P. Kulkarni, C. J. Tonzola, A. Babel, and S. A. Jenekhe, “Electron Transport Materials for Organic Light-Emitting Diodes,” *Chem. Mater.*, vol. 16, no. 23, pp. 4556–4573, Nov. 2004.
- [32] B. K. Yap, R. Xia, M. Campoy-Quiles, P. N. Stavrinou, and D. D. C. Bradley, “Simultaneous optimization of charge-carrier mobility and optical gain in semiconducting polymer films,” *Nat. Mater.*, vol. 7, no. 5, pp. 376–80, 2008.

- [33] S. Tiwari and N. C. Greenham, "Charge mobility measurement techniques in organic semiconductors," *Opt. Quantum Electron.*, vol. 41, no. 2, pp. 69–89, 2009.

## Chapter 3

### SOLVENT AND BAKING EFFECT ON POLYMER MORPHOLOGY AND PLED PERFORMANCE

#### 3.1 Solvent and Baking Effect on Phase Separation in Polymer Blend

Polymer light emitting devices (PLEDs) are steadily attracting more and more interest both from academia and industry. Despite the successful commercialization of small molecule organic light emitting device (OLED), PLEDs still remain a much less mature technology compared to OLEDs. Many fundamental issues at the molecular-scale are still waiting to be resolved before the successfully building stable high-performance PLEDs.

Due to the difficulties in fabricating multilayered structure using solution processed polymer materials, bulk heterojunction structure processed by spin coating polymer blend solutions is the most commonly-used strategy for polymer optoelectronic devices[1]–[3]. In the bulk heterojunction films formed by polymer blend, electron- and hole-transporting material result in thin films with optimized electrical properties compared to the homopolymer devices. In polymer blend systems, long polymer chains do not gain enough entropy to yield a negative free energy of mixing, thus mixing does not happen spontaneously [4]. Therefore, if enough time is given for the immiscible polymer blend system to reach equilibrium, the polymer would demix and form separated phases of individual polymers. In a polymer blend bulk heterojunction device, electrons transport through the electron-transporting polymer rich domains and holes transport through hole-transporting

polymer rich domains due to the better alignment with the corresponding electrodes respectively. Therefore, blend system with electron transporting domains and hole transporting domains can help carrier balance in devices. Controlling the interface and phase separation in polymer blend structure is of critical important for polymer blend based optoelectronic devices. The interface between hole- and electron-transporting polymers is the place where excitons form in a polymer LED structure. But after exciton formation, with in the diffusion length of 10 nm [9], [5], if the exciton meet another interface before their radiative recombination, the potential difference at the heterojunction interface yields a high probability of excitons breaking into separated electrons and holes. A tradeoff therefore needs to be considered for the domain sizes in phase separation. (It generally requires the domain size to be bigger than 10nm for exciton to have enough time to recombine before reaching another interface).

During the spin-coating process, the solvent evaporates much faster than the time needed to reach completely thermodynamic equilibrium. The extent of phase separation in blend thin film structures thus depends on such factors as polymer blend ratio, polymer molecular weight, solvent properties, substrate surface energy, and different solubility of homopolymers in common solvents. Among these factors, solvent vapor pressure is the easiest way of controlling phase separation and has been widely investigated for use in optoelectronics devices [6], [7]. For solvents like chloroform and tetrahydrofuran (THF) with low vapor pressure, they evaporate very fast during thin film formation in the spin-coating process, thus the domains of individual polymer only have a short time to grow before all the polymers are solidified in their fixed position. This results in small domain size and low phase separation of the two polymers. In contrast, for solvent like toluene and p-xylene

whose vapor pressures are high, they offers a longer time for polymer domain to develop before film solidification, resulting in large domain size and high phase separation in the blend structure. The inset in Figure 3-1 shows the morphology of polymer blend thin films spin-coated from toluene and chloroform solution respectively. Different degrees of phase separation in blend thin film can be beneficial for different applications [7]–[10]. For smaller domain sizes, the large polymer heterojunction interface provides more opportunity for exciton dissociation before recombines radiatively. This configuration is favorable for photovoltaic applications in which the excitons need to quickly convert into charged carriers and be collected through photocurrent. In contrast, large domain size is more suitable for LED applications because the excitons can have enough time to recombine and emit photons before dissociating at another domain's interface. Figure 3-1 shows the PL quenching in polymer blend compared with pristine F8BT due to the efficient exciton dissociation at the heterojunctions in the polymer blend. Comparing Figure 3-1 (a) and (b), the smaller domains in chloroform samples result in stronger exciton quenching than the larger domains obtained from toluene solution. For this reason, chloroform with low vapor pressure is generally used for polymer solar cell fabrication since it can provide rich interfaces for exciton dissociation[1], [11], [12], and solvents like toluene and p-xylene with high vapor pressure are generally used for polymer LED fabrication because they offer large domain sizes for the excitons to recombine in the exciton-acceptor domains [13], [14].

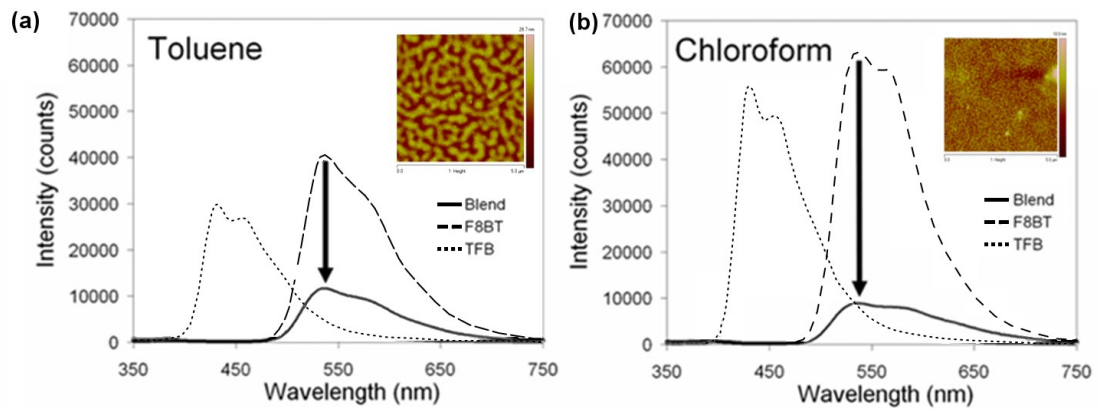


Figure 3-1: Blended TFB-F8BT polyfluorene-based type-II heterostructures using different solvents. (a) Fluorescence emission from pure TFB, pure F8BT, and 1:1 ratio TFB:F8BT blended films obtained from toluene solution. (b) Same measurements obtained from chloroform solution. The insets show AFM images of the domain structures in blended films [13], [15].

Figure 3-2 shows the PL and EL of a polymer LED device fabricated from TFB and F8BT blend toluene solution. The inset gives the blend thin film phase separation observed using confocal fluorescence measurements.

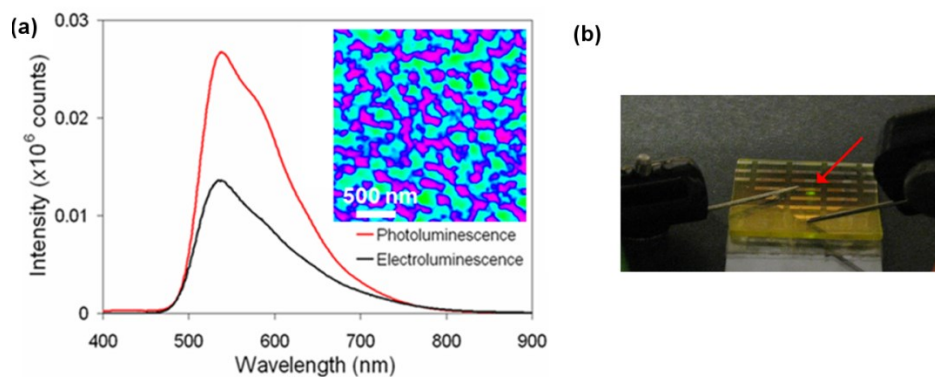


Figure 3-2: Bulk heterojunction polymer LED demonstration. (a) Polymer LED device EL and PL, the insets shows confocal fluorescence images of the domain structures in blended films. (b) Green-emitting PLED in operation [13], [16].

Beside the solvent effect, post-spin coating annealing can also alter the film morphology by providing external energy for the polymer to relax and reach equilibrium. Thus, annealing can greatly increase the domain size as shown in Figure 3-3 which compares the polymer blend film morphology before and after annealing in air at 100 °C.

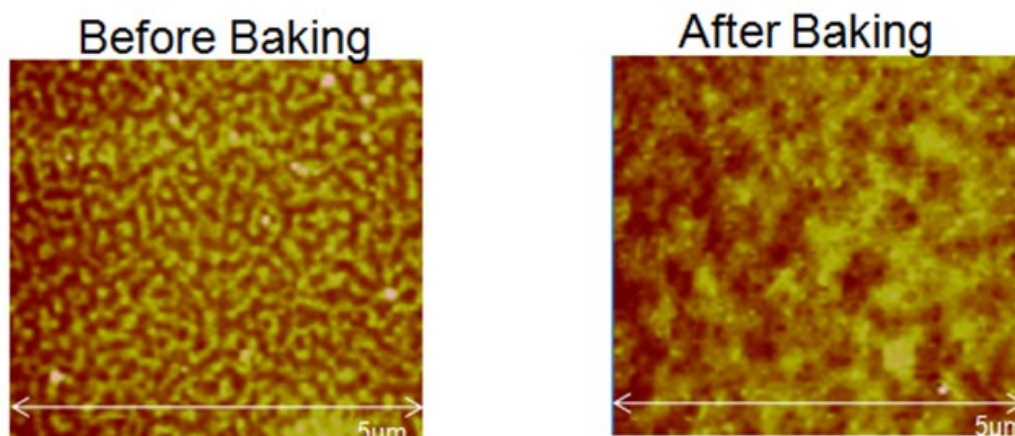


Figure 3-3: Comparison of the polymer blend film morphology before and after annealing in air at 100 °C measured under AFM.

### 3.2 Solvent and Baking Effect on Polymer Crystalline Structure in Thin Film

Many reports have investigated the solvent- and process-dependent PLED performance to the phase-separation in blend PLEDs [6]. However, another crucial aspect that also greatly affects polymer LED performance is the polymer chain alignment and morphology in the polymer thin film. We investigated that this aspect can be also greatly affected by different solvent property and fabrication processes.

It is well established the electrical and optical property of the PLEDs origin from the  $\pi$ -conjugation in the polymer chains. Therefore, changes in polymer chain alignment and morphology will have dramatic consequences on the delocalized electron state and the carrier transport properties in the polymer. In this section, we use photoluminescence (PL), electroluminescence (EL), current-voltage (IV) and conductive AFM (C-AFM) techniques to investigate the chain morphology effects on polymer thin film transport properties at the submicron scale and demonstrate how it can be controlled by using different solvent and through annealing.

Two different solvents were used in our experiment: toluene and chloroform. Toluene is an aromatic solvent with a benzene ring, while chloroform is a non-aromatic solvent as shown in the molecular structures in Figure 3-4. Therefore, it should be expected that different function group in the polymer chain will have different interaction energy with those two solvents [17]. To avoid the phase separation effect on the electrical and optical property of polymer thin film and device structure and only focus on the polymer chain crystalline and alignment, we use a mono-polymer LED structure. F8BT [poly(9,9'-dioctylfluorene-co-benzothiadiazole)] is used as the light-emitting polymer. To make the PLED devices, glass substrate was first covered by a sputtered ITO layer, which offers a  $50\Omega/\square$  resistance. A layer of PEDOT:PSS (Clevios P VP AI 4083, H.C. Starck Inc.) was spin-coated at 3000 rpm speed and 90s time duration on top of ITO as a hole injection layer. F8BT powder (American Dye Source, Inc.) was dissolved in each solvent in the concentration of 14mg/ml, spin (2000rpm, 60s) on PEDOT:PSS layer as carrier transporting layer and light emitting layer as well. A 60nm layer Al was finally evaporated on top as cathode. Figure 3.5 gives the whole device configuration.

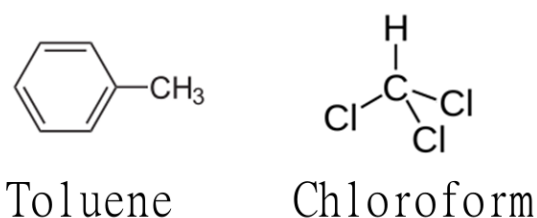


Figure 3.4: Molecular structures of the two solvents investigated in this thesis: toluene and chloroform

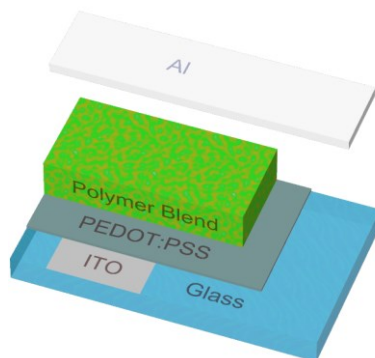


Figure 3.5: Polymer blend LED device configuration.

Figure 3-6 shows the photo-luminescence from polymer in solution and in solid state thin films spin-coated from toluene and chloroform solution respectively. In solution, the polymer chains are more isolated from each other, thus the PL peak is dominated by exciton emission from single polymer chains. In toluene, it is expected that the polymer backbone formed by benzene rings can be dissolved better in this aromatic solvent. The backbone forms a shell and leaves the alkyl side chain point inward as sketched in Figure 3-7 (a). The strong chain deformation in such solvent leads to a higher internal energy, which is the reason for the blue shift shown in toluene solution comparing with chloroform solution as in Figure 3-6. In chloroform solution, the alkyl side chains are better dissolved in the solvent, resulting in more extended chain morphology in solution. Therefore, the PL peak from chloroform-based polymer solutions is red-shifted. During spin coating process, solvent evaporate gradually, leaving the polymer chains aggregate together. The aggregation is indicated by the more pronounced PL peak shoulder, which is believed to be the excimer formed in aggregated polymer chains [18]. For the thin films measured right after spin-

coating, the similar PL spectral shape shows that the two solvents give same extent of aggregation after forming the solid state thin film.

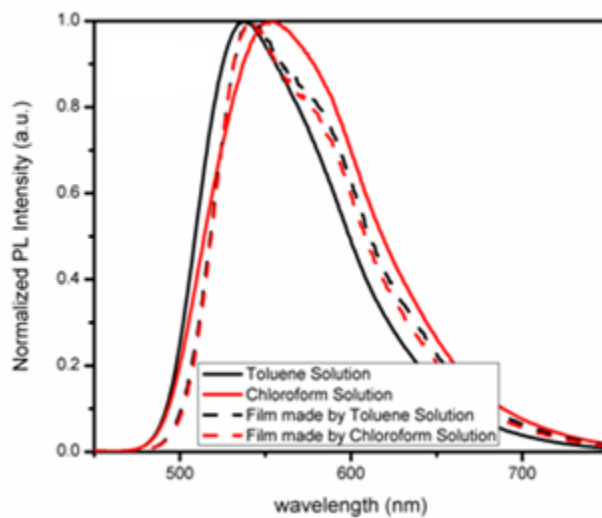


Figure 3-6: Normalized PL intensity for polymer in solution and solid state thin film made by spin coating, no baking was applied [15].

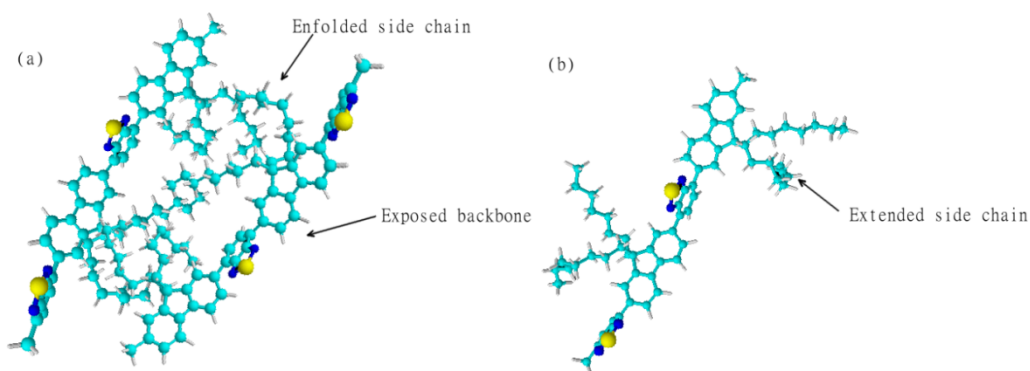


Figure 3-7: Polymer chain morphology in different solvent. (a) In aromatic solvent, the F8BT aromatic polymer backbone wrap the side chain inwards (b) The extended side chain and twisted backbone of F8BT polymer conformation in nonaromatic solvent. (The molecular structures were drawn in ChemSketch, this figure is inspired by ref [17].)

However, despite of the similar photo-luminescence peaks, the different IV curves in Figure 3-8 (a) and the dramatic current increase after baking indicate that polymer chains form different alignment morphologies in these thin films. For toluene, although the polymer chain was more aggregated in solution, the conjugated backbone is left extended, so electrons can transport more easily through this network, explaining the better transport in toluene thin film. For chloroform-based thin films, the network formed by non-conjugated side chains results in low device current. Furthermore, baking process gives extra energy for the polymer chain to re-align and form domains with ordered crystalline structure. After baking, the EL peak shifted to longer wavelength as in Figure 3-8 (b), which is a sign of better conjugation. The current increases for both backed chloroform and toluene samples in Figure 3-8(a). The red shift is more phenomenal for toluene sample with the backbone connected in

the polymer network, likely due to a better chain alignment and conjugation compared to chloroform-based samples, as should be expected after baking.

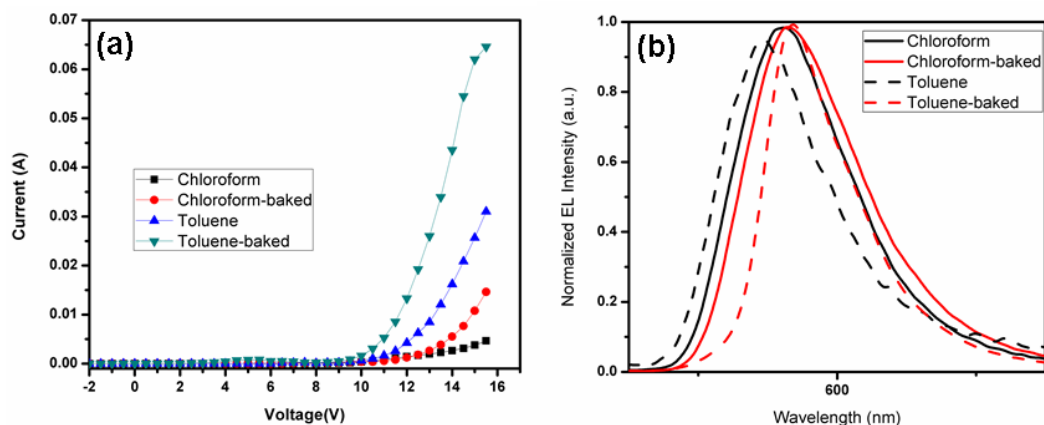


Figure 3-8: Device performance comparison under different fabrication conditions. (a) The IV curves from devices made using the two solvents and measured before and after baking respectively. (b) The EL spectra from these four samples [15].

The local transport properties were further examined by conductive (C-) AFM. It is shown in Figure 3-9 that only baked toluene thin films form conductive channels under a relatively lower bias. Small domains of high conductivities form in the thin film, explaining a better electron transport in baked toluene samples. Under the same bias, other samples did not show conductive channel formation in the thin film.

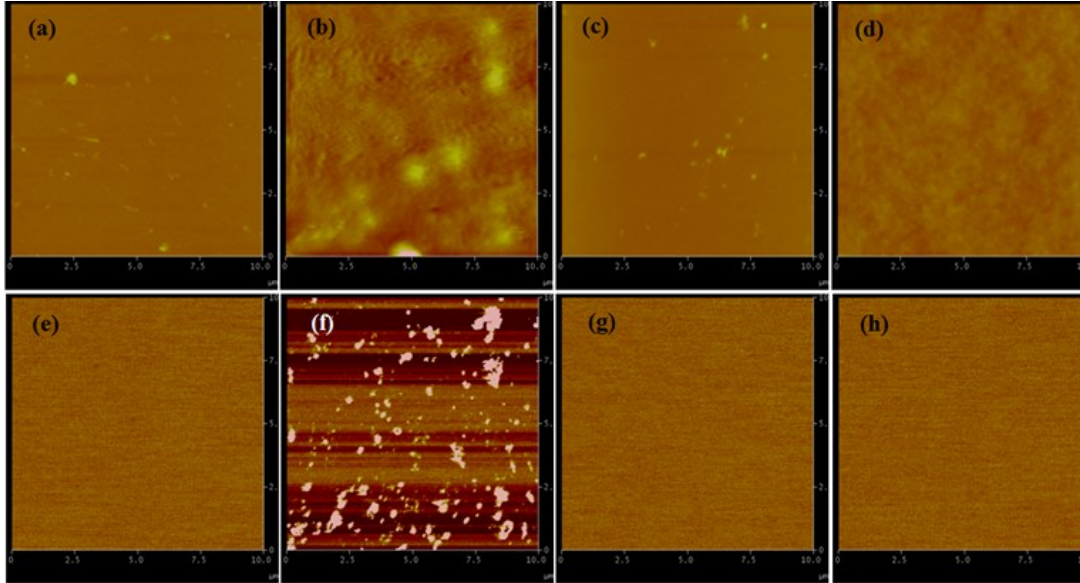


Figure 3-9: C-AFM data for the four samples in the experiment. The top row are the topological images and the bottom row are the conductance images. From left to right, (a)(e) are from toluene thin film, (b)(f) are from toluene thin film after baking, (c)(g) are from chloroform thin film, and (d)(h) are from chloroform thin film after baking [15].

Besides the transport properties, device output power is also an important parameter to improve device performances. Figure 3-10 shows the output power of the same four samples in Figure 3-8. Due to the fact that only one polymer is used, device brightness does not depend strongly on the solvent used, as in the case of blend LEDs formed by phase separation. However it is clear in Figure 3-10 that baking can greatly improve the device brightness.

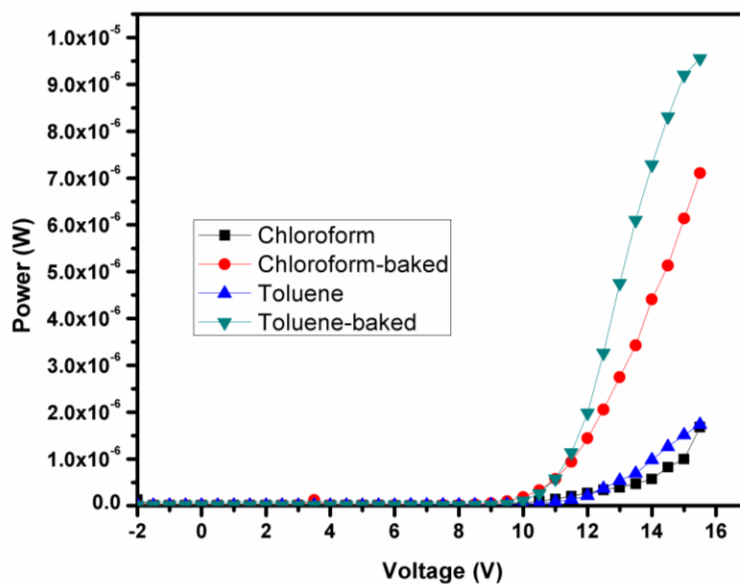


Figure 3-10: Output power from devices made from the two solvents before and after baking respectively [15].

As discussed above, baking provides extra energy for polymer chains to realign and form domains with ordered crystalline structure. These crystalline domains can be observed under confocal fluorescence microscopy due to their stronger emission intensity. Figure 3-11 shows confocal fluorescence images of the four thin films. The crystalline domains with much stronger emission can be observed clearly after baking for both toluene- and chloroform-based samples. The stronger enhancement in toluene samples is consistent with the better conjugation seen in the previously discussed electronic property characterization, and it can be explained by the fact that the polymer backbone is more favorably dissolved in toluene.

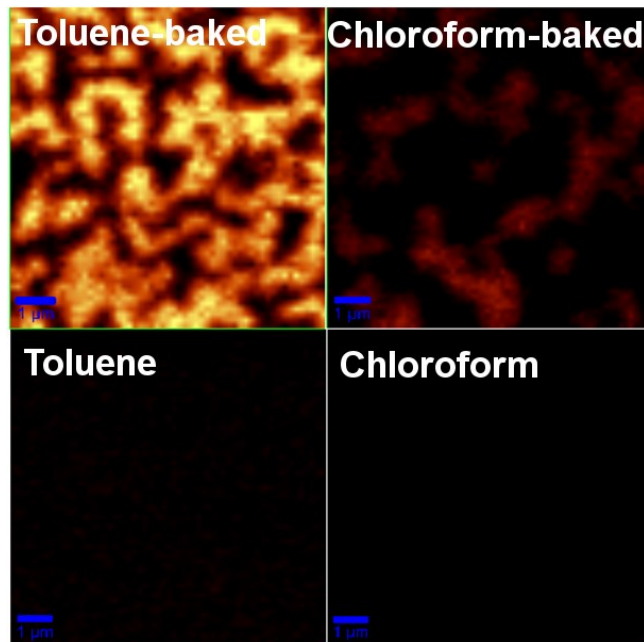


Figure 3-11: Confocal fluorescent microscopy images for the four samples in the experiment. (a)(e) toluene thin film, (b)(f) toluene after baking, (c)(g) chloroform thin film, and (d)(h) from chloroform after baking. Each scan area is  $10 \times 10 \mu\text{m}$  [15].

We further proved the formation of conductive channels and crystalline domains in blend thin films fabricated from toluene solution with post annealing. Figure 3-12 (a) shows the conductive AFM for toluene blend thin film before and after baking. In polymer blend, baking not only increased the domain size in polymer thin film, but also creates highly-conductive channels in the current image in Figure 3-12 (d). Meanwhile, domains of strong fluorescence are observed in the confocal fluorescence measurements in Figure 3-13.

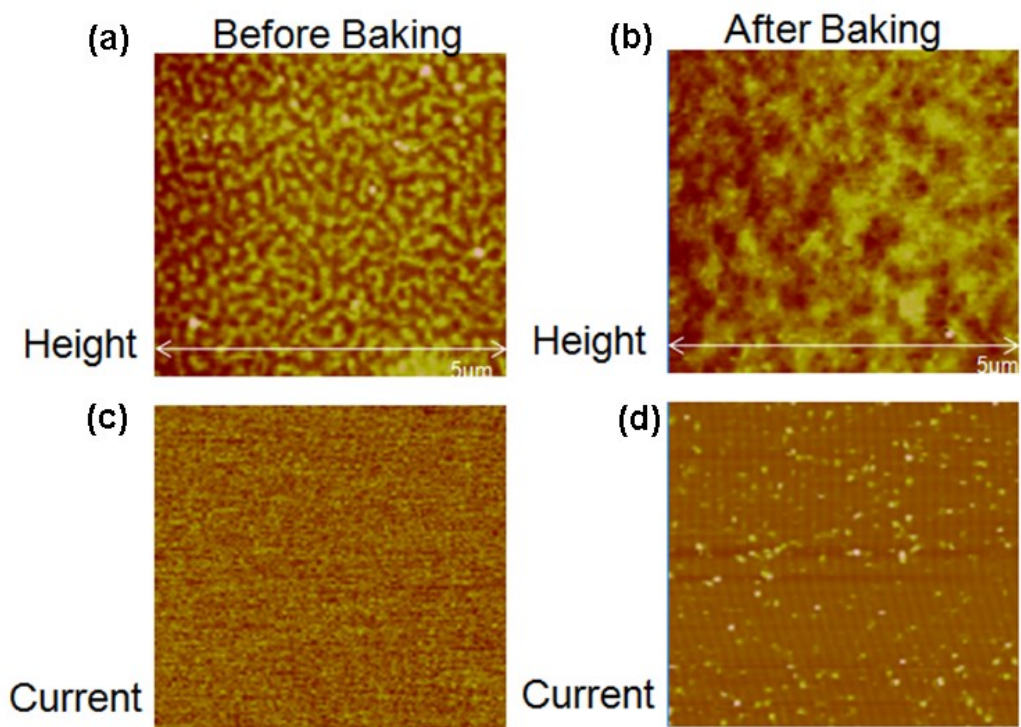


Figure 3-12: Conductive AFM measurements on polymer blend thin films fabricated from toluene solution. (a) and (c) are height and current of thin film before baking, (b) and (d) are height and current of thin film after baking [15].

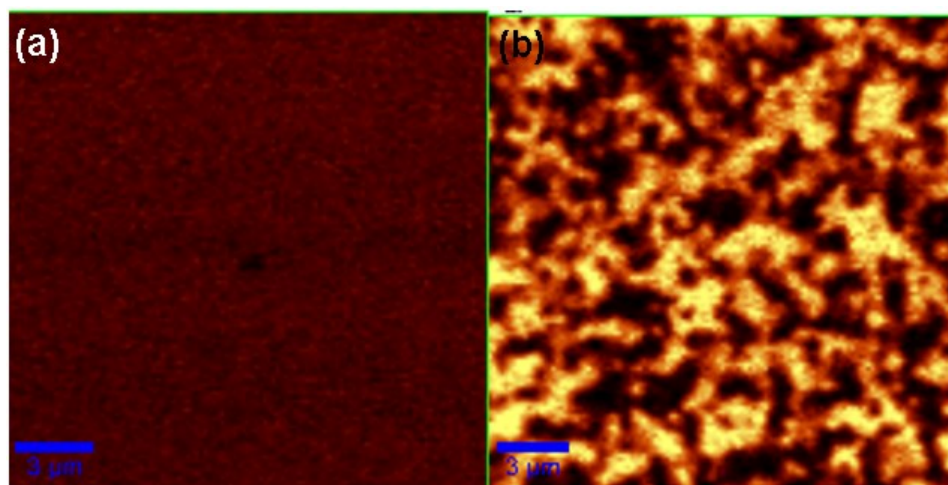


Figure 3-13: Confocal fluorescence of polymer blend thin film fabricated from toluene solution before and after baking.

### 3.3 Conclusion

This chapter provides a very important guideline on choosing the solvent and using a baking process for polymer LED fabrication. The solvents not only control the phase separation in polymer blend system by their vapor pressure, but the molecular structure also plays an important factor in forming conjugated polymer chain morphology. Aromatic solvent can favorably dissolve the polymer backbone instead of its side chain, thus facilitate the formation of backbone network which offers better transport and fluorescent property. Both the PL and EL spectra changes for polymer solution and device samples are consistent. C-AFM further confirmed the high conductive channel formation in baked toluene device.

## REFERENCES

- [1] J. Schmidtke, R. Friend, and C. Silva, "Tuning Interfacial Charge-Transfer Excitons at Polymer-Polymer Heterojunctions under Hydrostatic Pressure," *Phys. Rev. Lett.*, vol. 100, no. 15, p. 157401, Apr. 2008.
- [2] A. C. Morteani, A. S. Dhoot, J.-S. Kim, C. Silva, N. C. Greenham, C. Murphy, E. Moons, S. Ciná, J. H. Burroughes, and R. H. Friend, "Barrier-Free Electron-Hole Capture in Polymer Blend Heterojunction Light-Emitting Diodes," *Adv. Mater.*, vol. 15, no. 20, pp. 1708–1712, Oct. 2003.
- [3] Z.-L. Li, H.-F. Meng, S.-F. Horng, C.-S. Hsu, L.-C. Chen, and S.-M. Chang, "Strong red emission in heterojunctions of conjugated polymer blends," *Appl. Phys. Lett.*, vol. 84, no. 24, p. 4944, 2004.
- [4] F. S. Bates, "Polymer-polymer phase behavior.," *Science*, vol. 251, no. 4996, pp. 898–905, Feb. 1991.
- [5] J. Kim, "Electrical degradation of triarylamine-based light-emitting polymer diodes monitored by micro-Raman spectroscopy," *Chem. Phys. Lett.*, vol. 386, no. 1–3, pp. 2–7, 2004.
- [6] Y. Xia and R. H. Friend, "Phase Separation of Polyfluorene-Based Blend Films and Its Influence on Device Operations," *Adv. Mater.*, vol. 18, no. 11, pp. 1371–1376, 2006.
- [7] J.-S. Kim, P. K. H. Ho, C. E. Murphy, and R. H. Friend, "Phase Separation in Polyfluorene-Based Conjugated Polymer Blends: Lateral and Vertical Analysis of Blend Spin-Cast Thin Films," *Macromolecules*, vol. 37, no. 8, pp. 2861–2871, 2004.
- [8] N. Corcoran, a. C. Arias, J. S. Kim, J. D. MacKenzie, and R. H. Friend, "Increased efficiency in vertically segregated thin-film conjugated polymer blends for light-emitting diodes," *Appl. Phys. Lett.*, vol. 82, no. 2, p. 299, 2003.
- [9] Y. Xia and R. H. Friend, "Polymer bilayer structure via inkjet printing," *Appl. Phys. Lett.*, vol. 88, no. 16, p. 163508, 2006.

- [10] A. C. Arias, J. D. MacKenzie, R. Stevenson, J. J. M. Halls, M. Inbasekaran, E. P. Woo, D. Richards, and R. H. Friend, "Photovoltaic Performance and Morphology of Polyfluorene Blends: A Combined Microscopic and Photovoltaic Investigation," *Macromolecules*, vol. 34, no. 17, pp. 6005–6013, Aug. 2001.
- [11] C. R. McNeill, H. Frohne, J. L. Holdsworth, and P. C. Dastoor, "Near-Field Scanning Photocurrent Measurements of Polyfluorene Blend Devices: Directly Correlating Morphology with Current Generation," *Nano Lett.*, vol. 4, no. 12, pp. 2503–2507, Dec. 2004.
- [12] D. C. Coffey and D. S. Ginger, "Time-resolved electrostatic force microscopy of polymer solar cells.," *Nat. Mater.*, vol. 5, no. 9, pp. 735–40, 2006.
- [13] S. Cloutier, *Advanced Photonic Sciences*, no. 1. InTech, 2012, pp. 178–196.
- [14] E. Moons, "Conjugated polymer blends: linking film morphology to performance of light emitting diodes and photodiodes," *J. Phys. Condens. Matter*, vol. 14, no. 47, pp. 12235–12260, Dec. 2002.
- [15] X. Ma, F. Xu, and S. G. Cloutier, "Solvent and Baking Effect on Polymer Morphology and PLED Device Performance," in *Frontiers in Optics / Laser Science 2010*, 2010, p. LMA5.
- [16] X. Ma, F. Xu, and S. G. Cloutier, "High-Performance 1550 nm Polymer-Based LEDs on Silicon using Hybrid Polyfluorene-Based Type-II Heterojunctions," in *7th Inter. Conference on Group-IV Photonics*, 2010, p. WA2.
- [17] Y. Shi, J. Liu, and Y. Yang, "Device performance and polymer morphology in polymer light emitting diodes: The control of thin film morphology and device quantum efficiency," *J. Appl. Phys.*, vol. 87, no. 9, p. 4254, 2000.
- [18] R. Jakubiak, C. J. Collison, W. C. Wan, L. J. Rothberg, and B. R. Hsieh, "Aggregation Quenching of Luminescence in Electroluminescent Conjugated Polymers," *J. Phys. Chem. A*, vol. 103, no. 14, pp. 2394–2398, Apr. 1999.

## Chapter 4

### QUANTUM DOT LIGAND EXCHANGE EFFECT IN POLYMER AND QUANTUM DOT HYBRID STRUCTURE

#### 4.1 Introduction

Colloidal semiconductor quantum dots and  $\pi$ -conjugated organic polymers are two material systems allowing low-cost solution-based processing. As such, they have generated a tremendous interest for both the scientific and industrial research communities. The lowest band edge transition in colloidal quantum dots can be easily controlled by adjusting the synthesis conditions, offering large tunability [1]. Today, well-controlled synthesis procedures can provide quantum dots with uniform sizes, narrow emission peaks and high fluorescence quantum yields [2]. Recently, the cross-linking of colloidal dots using shorter molecular ligands further improved the transport properties and the stability of self-assembled nanocrystalline films [3], [4], allowing their integration into optoelectronic device structures. Short dithiol ligand exchange is a simple one step chemical treatment on solid state thin film to remove the long-chain ligand on quantum dot surface. The long-chain ligand used during quantum dot synthesis can control growth kinetics, allow for stable colloidal dispersions, and passivate surface states through the reaction process. However, the presence of these non-conductive long ligand chains create large barriers for carrier transport in quantum dot formed thin films, limiting their application for optoelectronic devices. Short thiolated molecule can exchange these long oleic acids due to the stronger bonding energy of thiolate comparing with carboxylic acid. The two thiol end of the short molecule can cross-link neighbor quantum dot, thus reduce the QD to QD spaces

as shown in Figure 4-1. Small quantum dot space facilitates carrier hopping between quantum dots, resulting in highly conductive thin films for optoelectronic applications. However, the cross-linking of quantum dots generally reduces the photoluminescence quantum yield of quantum dot films by introducing doping and defect states as well as exciton dissociation between coupled quantum dots [5]. On the other hand,  $\pi$ -conjugated fluorescent organic polymers offer high fluorescence efficiency, large oscillator strength [6], and good carrier transport properties. Combining colloidal quantum dots with  $\pi$ -conjugated polymers can provide hybrid structures with enhanced functionalities. Using polymers with properly aligned HOMO and LUMO levels, hybrid quantum dot-based heterostructures have shown increased performances for both solar cells [7] and light emitting diodes [8], [9]. In this chapter, the quantum dot ligand exchanges on glass and on semiconductor polymer are both analyzed.

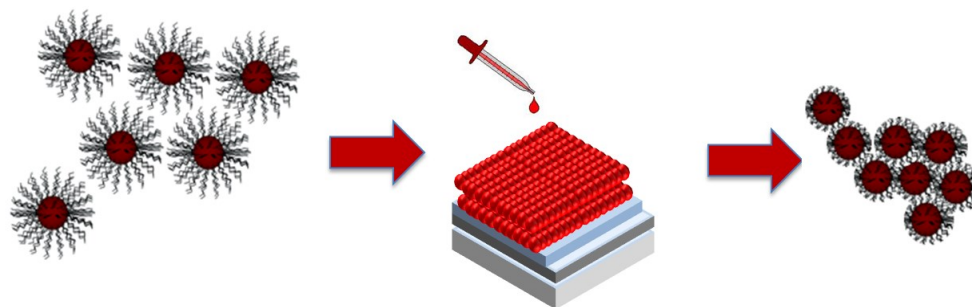


Figure 4-1: Schematic demonstration of ligand exchange process.

## **4.2 Absorption and Dielectric Constant Change on Cross-Linked Quantum Dot Thin Film**

### **4.2.1 Experiment**

Acetonitrile is used as the solvent for small molecule ligands. The 1,3-benzenedithiol (BDT, 99%, Sigmaaldrich) and 1,2-ethanedithiol (EDT, 98% Sigmaaldrich) are measured using micropipette, and 0.01M concentration are made for the ligand exchange. The PbS quantum dots are dissolved in hexane at a weight concentration of 14  $\mu$ M for the step by step spin-coating process. The quantum dot solution concentration was obtained from the absorption measurements using Beer's law ( $A=c\times\varepsilon\times l$ ), where A is absorption coefficient, c is molar concentration,  $\varepsilon$  is the molar extinction coefficient [10] and l is the sample's path length). The quantum dot is first spin-coated on glass at 2000 rpm for 30 seconds, and then several drops of the dithiol small molecule acetonitrile solution are dropped to fully cover the substrate. The small molecule ligand solution is left on the substrate for 30 seconds to enable the exchange process before spin-coating for 30 seconds again at 2000rpm. Finally the sample is raised with hexane during spinning to wash away any excess of PbS nanocrystals and ligand residues.

### **4.2.2 Result and Discussion**

For the 1050nm emission quantum dot used, the 1.22 eV absorption peak in Figure 4-2 (a) yields a quantum dot diameter of 3.4 nm by calculating from equation 2-2, which matches well with TEM measured average size in Figure 4-2 (b).

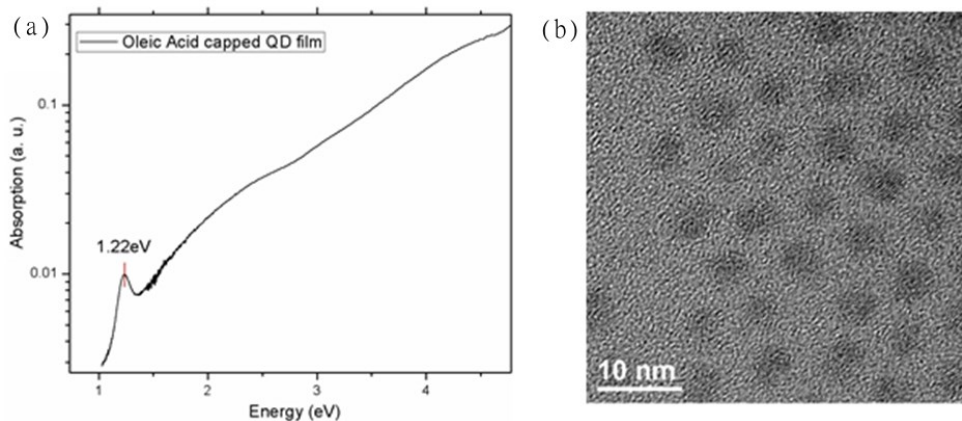


Figure 4-2: Quantum dot size determination through absorption peak. (a) Oleic Acid capped quantum dot film absorption. (b) TEM imaging of the quantum dots.

The reduced quantum dot space is confirmed by TEM of quantum dot capped with Oleic Acid, BDT and EDT in Figure 4-3. Comparing with Figure 4-3 (b) and (c), the quantum dot gap for BDT cross-linked sample is slightly larger than EDT cross-linked sample due to their longer molecule length.

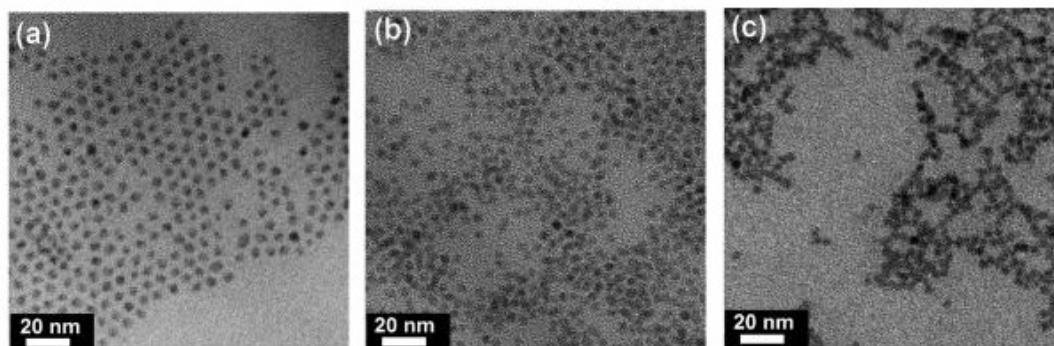


Figure 4-3: TEM image of quantum dot capped with (a) Oleic Acid, (b) BDT and (c) EDT [11].

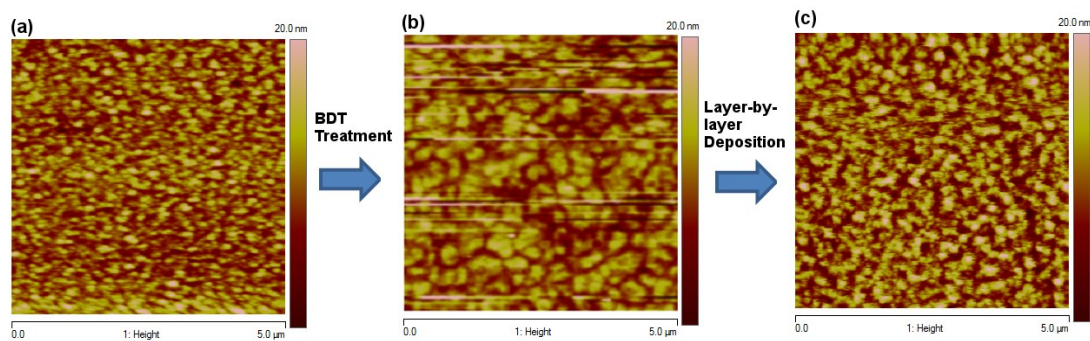


Figure 4-4: AFM image of as deposited OA capped quantum dot thin film (a), BDT treated single-layer quantum dot thin film (b) and BDT treated quantum dot thin film after 3 circle of layer-by-layer deposition.

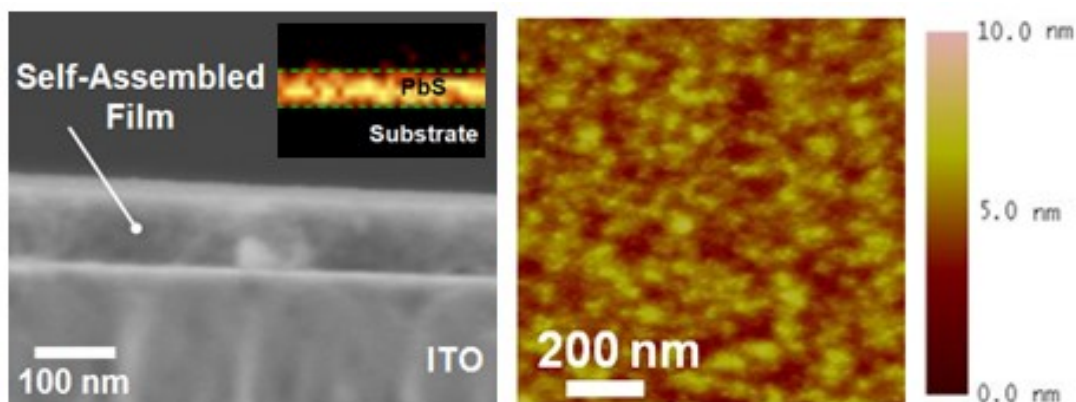


Figure 4-5: Cross-linked quantum dot thin film morphology. (a) Cross-section SEM of layer-by-layer dithiol ligand exchanged thin film, the inset shows the cross-section confocal Raman spectroscopy on PbS thin film. (b) AFM of the dithiol ligand exchanged thin film top morphology [12].

In each treated steps, the ligand exchange can results in cracks due to the significant volume contraction when the bulky oleic acid was replaced by short dithiol molecule. Figure 4-4 (b) clearly demonstrated the cracks after one layer ligand exchange. However, the small cracks can be gradually filled by the following layer deposition during the layer-by-layer ligand exchange process as in Figure 4-4 (c),

resulting in a pin-hole free and compact nanocrystalline thin film. Figure 4-5 demonstrated the high quality compact quantum dot thin film fabricated from the layer-by-layer dithiol ligand exchange procedure.

Besides the reduced quantum dot space after ligand exchange from an oleic acid to a short dithiol linker, the optical absorption from the treated quantum dot films is increased significantly as given in Figure 4-6. This absorption increase after ligand exchange stems mostly from a higher dielectric constant refractive index in the denser quantum dot films [3]. Using effective medium approximation to simulate the absorption cross section spectra and the oscillator strength dependence on the inter-dot separation, we find an excellent match for films of pristine oleic acid-capped over the whole spectrum, pointing to a dielectric constant of 1.65 for the un-treated film. For the dithiol-treated films, the model still agrees relatively well with the measurements and points to dielectric constants around 2.52 for EDT- and 2.43 for BDT-treated quantum dot films.

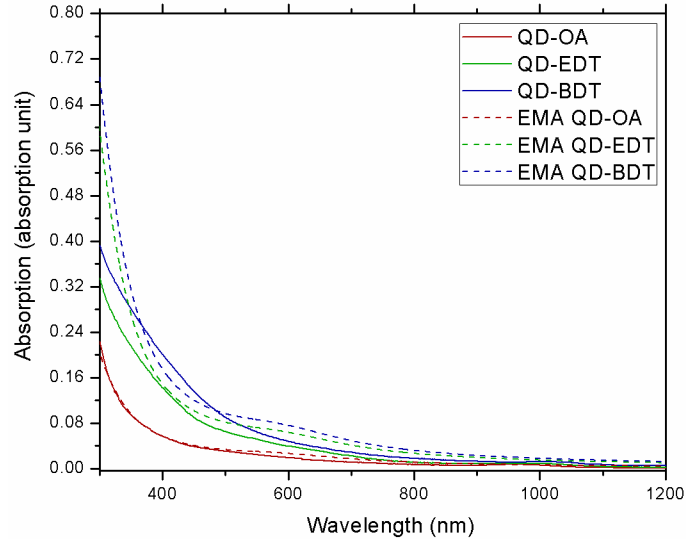


Figure 4-6: Measured and effective medium approximation (EMA) simulated absorption spectra for oleic acid (OA), ethanedithiol (EDT) and benzenedithiol (BDT)-capped quantum dot films.

The three component effective medium approximation (EMA) used to calculate the permittivity of the quantum dot films is given as following [13]:

$$\epsilon_{eff} = \frac{f\epsilon_c A_c \rho^3 + f\epsilon_s A_s (1-\rho^3) + \epsilon_m (1-f)}{f A_c \rho^3 + f A_s (1-\rho^3) + 1-f} \quad (4-1)$$

where  $\epsilon_c$ ,  $\epsilon_s$  are the permittivities of the bulk core material and shell material respectively,  $\epsilon_m$  is for the surrounding media between quantum dots,  $f$  is the filling factor of quantum dots in the film,  $A_c = 3\epsilon_s B$ ,  $A_s = (\epsilon_c + 2\epsilon_s)B$ ,  $\rho = \frac{r_c}{r_s}$ ,  $r_c$  and  $r_s$  are the radii of core and shell. Here,  $r_c = 1.7\text{nm}$  for the quantum dot core, and  $B$  is given by:

$$B = \frac{3\epsilon_m}{(\epsilon_s + 2\epsilon_m)(2\epsilon_s + \epsilon_c) - 2(\epsilon_s - \epsilon_m)(\epsilon_s - \epsilon_c)\rho^3} \quad (4-2)$$

Using bulk PbS permittivity from ref [14] for  $\epsilon_c$ ,  $f = 0.64$  due to a random close packing [15], while the space between quantum dots are considered to be filled with ligand molecules so that  $\epsilon_s = \epsilon_m$  is used in the model. The parameters used for oleic acid (OA), ethanedithiol (EDT) and benzenedithiol (BDT)-treated quantum dot films in the EMA model are summarized in Table 4-1. From the effective permittivity, the absorption spectrum can be reproduced by  $\alpha \cdot l = \frac{4\pi\kappa_{eff}}{\lambda_0} \cdot l$ , where  $\kappa_{eff}$  is the imaginary part of effective refractive index and  $l$  is the film thicknesses, which values are measured by AFM and given in Table 4-1. Figure 4-6 gives the EMA estimated absorption compared with the experimental results. Clearly, the EMA predictions agree well with the experiment for pristine oleic acid-encapsulated quantum dot films. However, discrepancies can be observed at short wavelengths for EDT- and BDT-treated films, possibly due to other interactions like inter-dot coupling of higher excitonic states or introduction of defect states after ligand exchange [3]. However, a decent match can still be obtained between 400~650nm, covering the fluorescence of the polymer. Effective refractive indexes of the films as estimated by EMA are also given in Table 4-1.

Table 4-1: Parameters used in the EMA model.

	$\epsilon_s = \epsilon_m$	$r_s$ (nm) ( $r_c$ +ligand)	$l$ ( nm)	$n_{eff}$ (@405nm)	$\kappa_{eff}$ (@405nm)
QD-OA	2.2	3.0	35	1.65	0.05
QD-EDT	2.9	1.82	14	2.52	0.23
QD-BDT	2.9	1.9	20	2.43	0.21

### 4.3 Quantum Dot Cross-Linked On Polymer

For quantum dot exchange on polymer substrate, the blue-fluorescence polyfluorene TFB is used here. The TFB is a typical p-type hole-transporting material used in polymer LEDs [16] and some hybrid quantum dot-based LEDs [8], [9]. Two orthogonal solvents are used to form this hybrid bi-layer structure. First, the TFB polymer is dissolved in toluene (6mg/ml) and spin-coated on a glass substrate at 2000 rpm for 60s. The following quantum dot deposition is the same as in the above section. Figure 4-7 gives the sample configuration and BDT and EDT ligands used for the quantum dot layer cross-linking atop the polymer film.

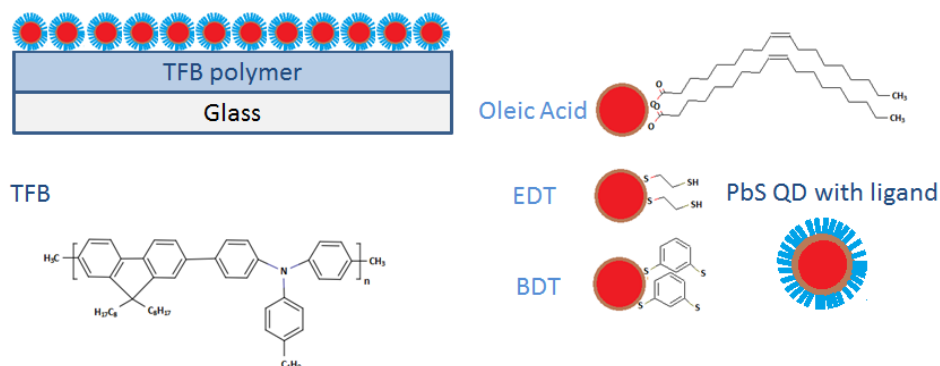


Figure 4-7: Hybrid bi-layer device schematics and the molecular structure of the TFB polymer and oleic acid, ethanedithiol (EDT) and benzenedithiol (BDT) quantum dot ligands.

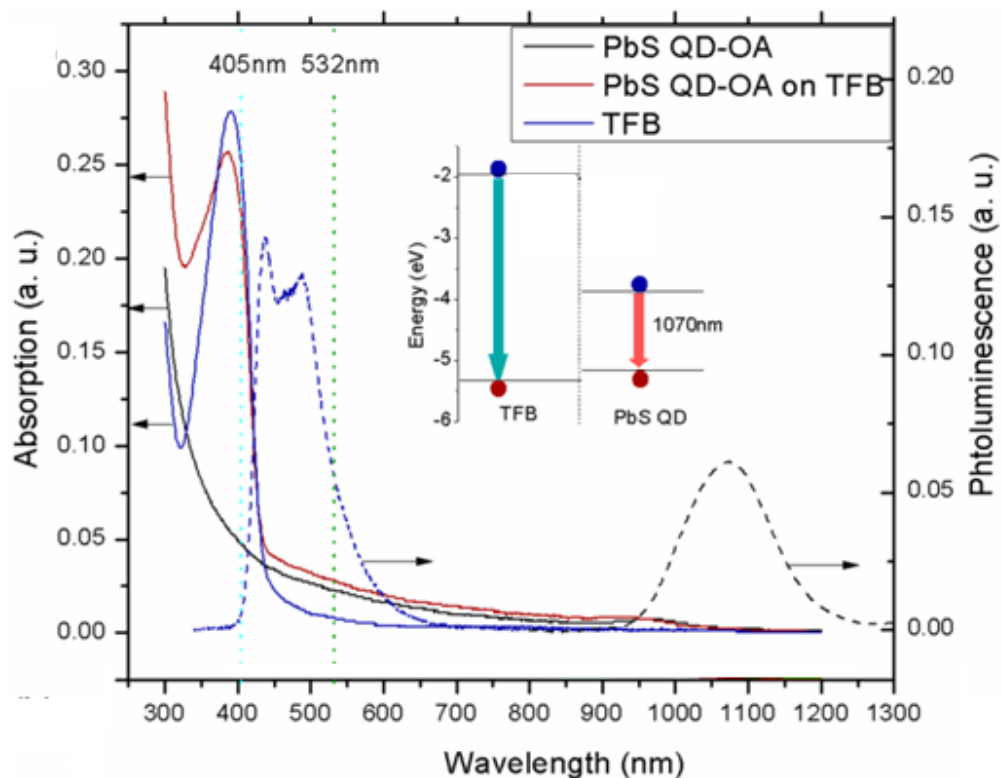


Figure 4-8: Absorption (—) and fluorescence (---) of the hybrid polymer-nanocrystal structure and for stand-alone polymer and quantum dot films. The inset shows the type-I heterojunction alignment for the hybrid polymer and quantum dot bi-layer structure based on known LUMO and HOMO levels for the TFB polymer [17] and for 3.4 nm PbS quantum dot [18].

The film thicknesses are all measured by contact mode AFM. The quantum dot TEM image is recorded on JEM 2010F instrument operating at 200 KeV. The photoluminescence are performed using a Jobin-Yvon iHR320 triple-grating spectrometer equipped with a Symphony thermoelectric-cooled InGaAs detector collect the near-infrared emission and a Synapse silicon CCD array for the visible. The excitation is performed using a CW 405 nm laser diode and a frequency-stabilized CW laser at 532 nm (TORUS from Laser-Quantum, Inc.). Both laser powers are carefully

attenuated to low levels so that no photobleaching or photo-induced damage can be sustained during the measurements. Absorption measurements are performed on a UV-VIS-NIR spectrophotometer (UV-3600, Shimadzu).

The hybrid bi-layer heterostructure shows an absorption spectrum combining the contributions from both the polymer and quantum dot layers in Figure 4-8.

Firstly, as a control experiment, the possible effect of all the following chemicals (hexane, acetonitrile, BDT and EDT) on the polymer layer were verified by looking at the fluorescence intensity and AFM measurements with and without exposure to these solutions. After washing the polymer film by any of these chemicals, no change whatsoever in polymer film thickness can be measured. Only very small changes in fluorescence intensity can be seen for EDT, acetonitrile and hexane, but a 30% reduced fluorescence is observed for BDT washed polymer film as seen in Figure 4-9.

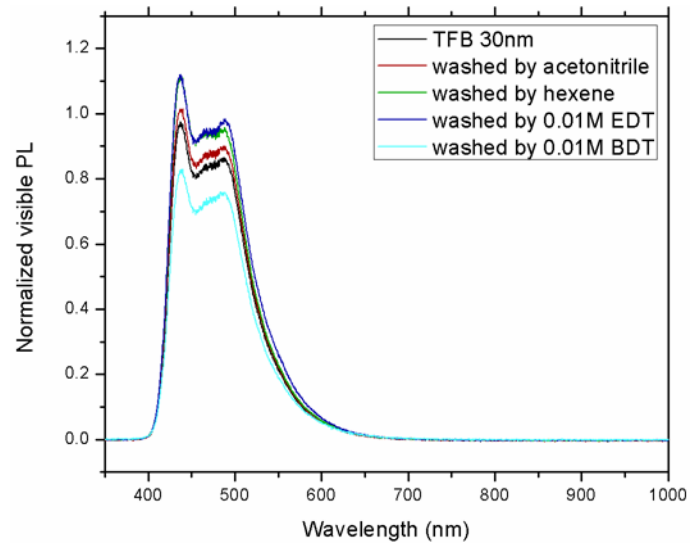


Figure 4-9: Fluorescence of 30 nm-thick TFB polymer films with and without exposure to acetonitrile, hexane, EDT and freshly-prepared BDT solutions.

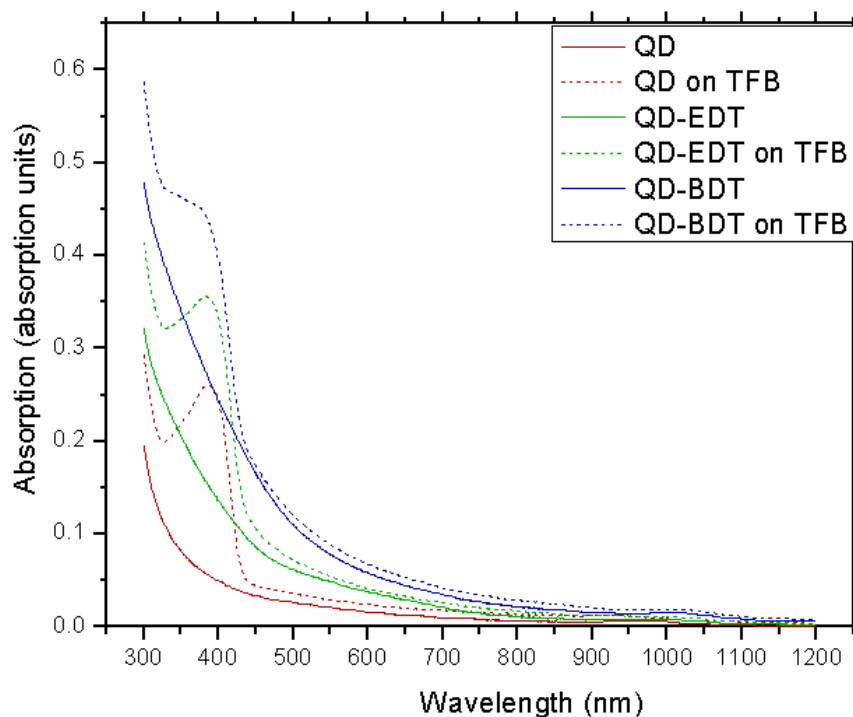


Figure 4-10: Absorption spectra for oleic acid (OA), ethanedithiol (EDT) and benzenedithiol (BDT)-treated quantum dots films by themselves and atop a TFB polymer film.

Figure 4-11 describes the polymer fluorescence and quantum dot emission in the oleic acid capped quantum dot/polymer hybrid bi-layer structure compared with the stand-alone polymer and quantum dot films. In Figure 4-11 (a), the sample is illuminated by a 405nm laser, which is close to the absorption peak of the TFB; and in Figure 4-11 (b), it shows the infrared quantum dot emission in the hybrid and control samples under 532 nm excitation, for which the polymer is not excited due to its higher transition energy. In Figure 4-11 (b) hybrid samples show a near-IR emission closely resemble the quantum dot control samples, consistent with a previous report that no charge separation occurs at a type-I polymer/quantum dot interface[19] . Thus,

we can conclude that there is no strong quantum dot fluorescence quenching happening due to exciton dissociation in this hybrid type-I structure. However, it can be observed in Figure 4-11 (a) that both the polymer and the quantum dot fluorescence are quenched for the hybrid bi-layer compared to the control samples when they are excited under 405 nm. Since the possibility of strong exciton dissociation has been previously ruled-out, it can be shown that this near-IR emission quenching is due to the reduced laser light absorption in the hybrid structure. In fact, the films absorptions given in Figure 4-8 have already demonstrated that the total absorption of the hybrid sample is lower than the sum of individual quantum dot film and polymer film. Indeed, we used a multilayer plane-wave model [20] to calculate the polymer and PbS layer absorption changes in the hybrid structure compared to the control samples on glass slides. The simulation results are shown as dotted lines in Figure 4-11 and present the expected fluorescence attributed to the absorption change in the hybrid sample configuration. In Figure 4-11 (a), the calculated polymer and quantum dot fluorescence intensities show a relatively good match with the experimental results for the un-treated hybrid sample, as such, the fluorescence intensity changes for polymer and quantum dot in the un-treated hybrid structure comparing with polymer or quantum dot monolayer thin films respectively are mostly due to change of absorption in the multilayer structure, but not because of charge separation, charge transfer or material quantum yield changes.

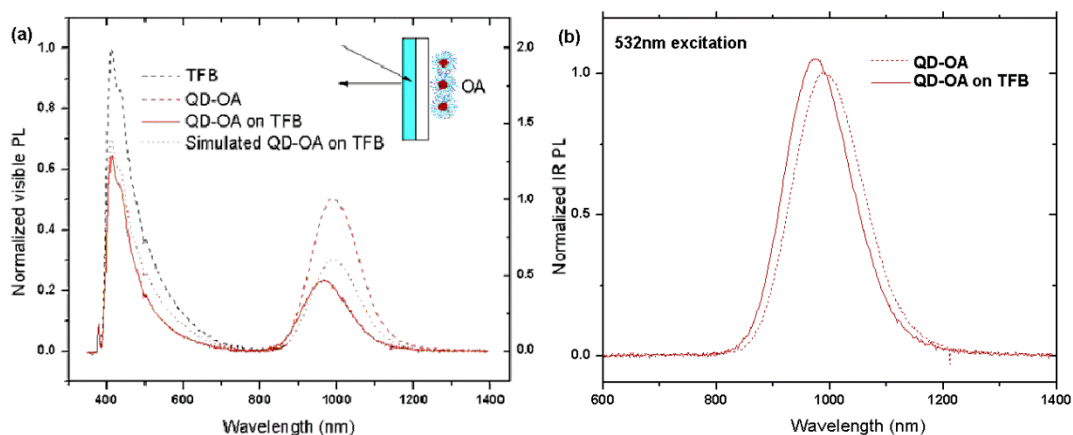


Figure 4-11: Polymer and quantum dot fluorescence under 405nm excitation (a) and 532nm excitation (b) for pristine oleic acid (OA)-capped samples. The inset shows the measurement configuration.

On the other hand, for shorter dithiol ligand-treated dots, a significantly enhanced near-IR emission is observed when comparing with both the control samples and the theoretical model based on absorption. The modelling results can still match with the polymer fluorescent quenching as seen in Figure 4-12 (a) and (c). To understand the mechanism behind the phenomenal quantum dot enhancement, the samples are also examined under 532nm excitation. As can be seen in Figure 4-12 (b) and (d), the high quantum dot enhancements exclude the possibility of energy transfer from polymer to quantum dot, due to the fact that the polymer is not excited under 532nm laser. As given in Figure 4-8, at 532nm, the absorption of hybrid sample is the same as thin films of quantum dot alone, therefore, the enhanced quantum dot fluorescent cannot be attributed to any addition absorption in the hybrid structure. Despite the fact that the hexane quantum dot solution does not dissolve the polyfluorene polymer, it can induce swelling of the polymer chain and cause them to

envelope the adjacent quantum dot. Therefore after ligand exchange, the enveloped polymer can efficiently passivate the quantum dot surface while maintaining their close coupling as indicated by the redshift of quantum dot PL peak in Figure 4-12 (b) and (d) compared with Figure 4-11 (b).

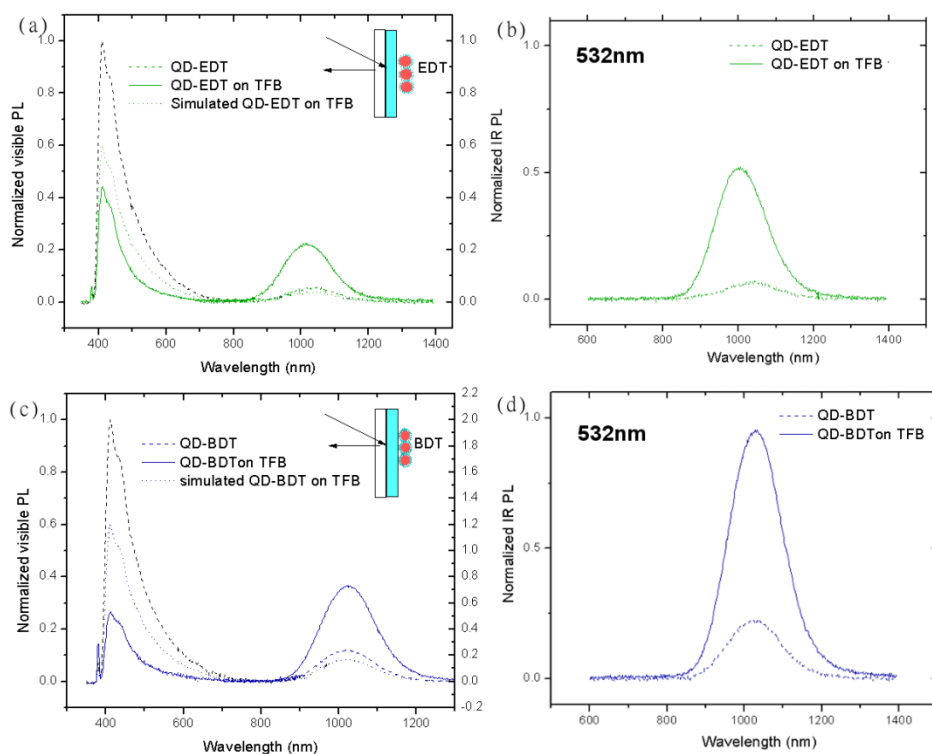


Figure 4-12: Polymer and quantum dot fluorescence for EDT treated samples under 405nm excitation (a) and 532nm excitation (b), and for BDT treated sample under 405nm excitation (c) and 532nm excitation (d). The insets show the measurement configurations.

#### **4.4 Conclusion**

In conclusion, we report large cross-linked quantum dot fluorescence enhancement by depositing them on a blue polyfluorene polymer layer. These boosted fluorescent quantum yield after dithiol exchange are attributed to increased surface state passivation due to the envelopment of underneath polymer chain on quantum dots. A multilayer plane wave absorption model is used to analyze the absorption changes in the hybrid structures. Good agreements are found for the polymer fluorescence quenching and OA-capped quantum dot fluorescence measurements. This large near-infrared emission enhancement can be highly beneficial for improving hybrid polymer-nanocrystal light emitting devices. Therefore, short ligand quantum dot cross-linking on polymer opens an efficient path for improving quantum dot emission while maintaining their good charge transport property after ligand exchange, pointing to a new design scheme for hybrid optoelectronic devices such as LEDs, photodiodes, and solar cells.

## REFERENCES

- [1] G. Schmid, *Nanoparticles: From Theory to Application*. Wiley-VCH, 2010, p. 533.
- [2] M. A. Hines and G. D. Scholes, “Colloidal PbS Nanocrystals with Size-Tunable Near-Infrared Emission: Observation of Post-Synthesis Self-Narrowing of the Particle Size Distribution,” *Adv. Mater.*, vol. 15, no. 21, pp. 1844–1849, Nov. 2003.
- [3] J. M. Luther, M. Law, Q. Song, C. L. Perkins, M. C. Beard, and A. J. Nozik, “Structural, optical, and electrical properties of self-assembled films of PbSe nanocrystals treated with 1,2-ethanedithiol,” *ACS Nano*, vol. 2, no. 2, pp. 271–80, Feb. 2008.
- [4] J. P. Clifford, G. Konstantatos, K. W. Johnston, S. Hoogland, L. Levina, and E. H. Sargent, “Fast, sensitive and spectrally tuneable colloidal-quantum-dot photodetectors,” *Nat. Nanotechnol.*, vol. 4, no. 1, pp. 40–4, Jan. 2009.
- [5] J. J. Choi, J. Luria, B.-R. Hyun, A. C. Bartnik, L. Sun, Y.-F. Lim, J. a Marohn, F. W. Wise, and T. Hanrath, “Photogenerated exciton dissociation in highly coupled lead salt nanocrystal assemblies,” *Nano Lett.*, vol. 10, no. 5, pp. 1805–11, May 2010.
- [6] Q. Zhang, T. Atay, J. R. Tischler, M. S. Bradley, V. Bulović, and a V Nurmikko, “Highly efficient resonant coupling of optical excitations in hybrid organic/inorganic semiconductor nanostructures. support information,” *Nat. Nanotechnol.*, vol. 2, no. 9, pp. 555–9, Sep. 2007.
- [7] C. Piliago, M. Manca, and R. Kroon, “Charge separation dynamics in narrow band gap polymer/PbS nanocrystal blend for efficient hybrid solar cells,” *J. Mater. ...*, no. 207890, 2012.
- [8] X. Ma, F. Xu, J. Benavides, and S. G. Cloutier, “High performance hybrid near-infrared LEDs using benzenedithiol cross-linked PbS colloidal nanocrystals,” *Org. Electron.*, vol. 13, no. 3, pp. 525–531, Mar. 2012.

- [9] T.-H. Kim, K. Cho, E. K. Lee, S. J. Lee, J. Chae, J. W. Kim, D. H. Kim, J. Kwon, G. Amaratunga, S. Y. Lee, B. L. Choi, Y. Kuk, J. M. Kim, and K. Kim, "Full-colour quantum dot displays fabricated by transfer printing," *Nat. Photonics*, vol. 5, no. 3, pp. 176–182, Feb. 2011.
- [10] I. Moreels, K. Lambert, D. Smeets, D. De Muynck, T. Nollet, J. C. Martins, F. Vanhaecke, A. Vantomme, C. Delerue, G. Allan, and Z. Hens, "Size-dependent optical properties of colloidal PbS quantum dots.," *ACS Nano*, vol. 3, no. 10, pp. 3023–30, Oct. 2009.
- [11] F. Xu, X. Ma, C. R. Haughn, J. Benavides, M. F. Doty, and S. G. Cloutier, "Efficient exciton funneling in cascaded PbS quantum dot superstructures.," *ACS Nano*, vol. 5, no. 12, pp. 9950–7, Dec. 2011.
- [12] S. Cloutier, *Advanced Photonic Sciences*, no. 1. InTech, 2012, pp. 178–196.
- [13] J. Spanier and I. Herman, "Use of hybrid phenomenological and statistical effective-medium theories of dielectric functions to model the infrared reflectance of porous SiC films," *Phys. Rev. B*, vol. 61, no. 15, pp. 437–450, 2000.
- [14] H. Kanazawa and S. Adachi, "Optical properties of PbS," *J. Appl. Phys.*, vol. 83, no. 11, p. 5997, 1998.
- [15] R. Zallen, *The Physics of Amorphous Solids (Wiley Classics Library)*. Wiley-VCH, 1998, p. 318.
- [16] J.-S. Kim, P. K. H. Ho, C. E. Murphy, and R. H. Friend, "Phase Separation in Polyfluorene-Based Conjugated Polymer Blends: Lateral and Vertical Analysis of Blend Spin-Cast Thin Films," *Macromolecules*, vol. 37, no. 8, pp. 2861–2871, Apr. 2004.
- [17] M. Sykora, A. Y. Kuposov, J. A. McGuire, R. K. Schulze, O. Tretiak, J. M. Pietryga, and V. I. Klimov, "Effect of air exposure on surface properties, electronic structure, and carrier relaxation in PbSe nanocrystals.," *ACS Nano*, vol. 4, no. 4, pp. 2021–34, Apr. 2010.
- [18] R. J. Ellingson, M. C. Beard, J. C. Johnson, P. Yu, O. I. Micic, A. J. Nozik, A. Shabaev, and A. L. Efros, "Highly efficient multiple exciton generation in colloidal PbSe and PbS quantum dots.," *Nano Lett.*, vol. 5, no. 5, pp. 865–71, May 2005.

- [19] A. Gocalińska, M. Saba, F. Quochi, M. Marceddu, K. Szendrei, J. Gao, M. a. Loi, M. Yarema, R. Seyrkammer, W. Heiss, A. Mura, and G. Bongiovanni, "Size-Dependent Electron Transfer from Colloidal PbS Nanocrystals to Fullerene," *J. Phys. Chem. Lett.*, vol. 1, no. 7, pp. 1149–1154, Apr. 2010.
- [20] N. J. Tao, "Measurement of Single Molecule Conductance: Benzenedithiol and Benzenedimethanethiol," *Nano Lett.*, vol. 4, no. 2, pp. 267–271, Feb. 2004.

## Chapter 5

### HIGH PERFORMANCE HYBRID NEAR-INFRARED LEDES USING PBS COLLOIDAL NANOCRYSTALS

#### 5.1 Quantum Dot LED Structure Review

Despite of the many successful high performance CdSe (CdS or ZnS) core (shell) visible quantum dot LED structures [1]–[3], the performance and device structure are still very limited for infrared quantum dot device mainly due to their lower stability and the long ligands used during synthesis process. The long ligand molecules around the infrared quantum dot offers quantum dot good stability in organic solvent, however would hamper the carrier transport through quantum dot layer. Therefore, multilayered quantum dot structure used in CdSe quantum dot LEDs cannot be easily adapted into infrared quantum dot device. Two strategies that were used for infrared quantum dot LEDs are (1) quantum dot dispersed in polymer matrix[4] and (2) quantum dot monolayer between organic hole- and electron-transporting layers [5], [6].

Figure 5-1 demonstrates the two configurations used in previous infrared QD-LED reports:

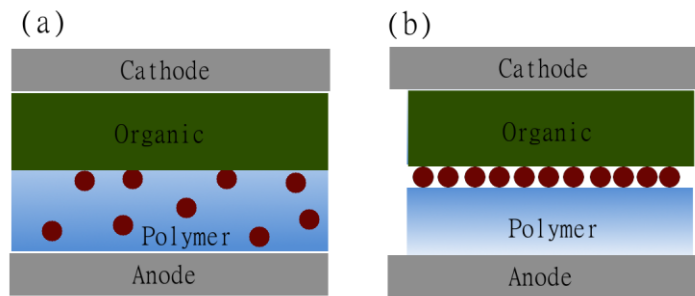


Figure 5-1: Device configurations in previous near-IR quantum dot LEDs.

Given the fact that quantum dots and polymers can be dissolved in the same solvent, the most obvious approach to make quantum dot and polymer hybrid device is to mix them prior to solution spin-coating. This approach uses polymer and organic molecule as the carrier transporting materials to overcome the bad conductive properties of long ligand-capped quantum dots [7]. The quantum dots dispersed uniformly in the polymer matrix can fluoresce by either carrier injection from the polymer matrix or exciton energy transfer from the host polymer's fluorescence. This last approach offers a simple and convenient way to achieve near-IR electroluminescence.

However, in previous report which using mono-polymer as the host material, because the polymer generally only offers good transport for one kind of carriers, either holes or electrons, imbalanced carrier injection into the quantum dot region results in low IR emission [4]. But in our electron transport and hole transport polymer blend host material based quantum dot and polymer hybrid structure, it is noticed that this configuration still suffers from fundamental drawbacks that limit the device performance. In quantum dot and polymer blend hybrid structure, not only the

quantum dot is non-conductive, but the incorporation of nanoparticle in polymer thin film can also disturb the polymer chain alignment in the thin film, hampering the transport property of the blend thin film and resulting in device with a low conductivity and a high turn on voltage. Section 5.2 gives the detailed investigations of the influences on polymer chain alignment caused by quantum dot incorporation.

The other early approach is shown in Figure 5-1 (b), where a monolayer of quantum dot is sandwiched by a polymer hole-transporting layer and a small molecule electron-transporting layer. This structure proposed by Bawendi's group uses vertical phase separation to locate the quantum dot on top of polymer during a single spin-coating process. The following electron-transporting organic layer is deposited using thermal evaporation method. Due to the low-conductivity nature of quantum dots, a careful control of the quantum dot concentration is required to produce only monolayer of quantum dots because stacked multilayers of quantum dots can significantly reduce the carrier transport and reduce the device performances. The low incorporation of quantum dot limits the device's infrared output power. Meanwhile, a large portion of visible emission is observed from the device, causing the waste of injected carrier into visible emission rather than infrared emission from quantum dots [8].

## **5.2 Polymer/Quantum Dot Blend Hybrid Structure and Its Limitations**

While blend structure offers the most affordable method for hybrid device fabrication, in our quantum dot and polymer hybrid structure, we investigated the effect of incorporation of quantum dot in polymer thin film on polymer blend morphology and polymer chain alignment morphology.

To balance the carrier injection into quantum dot in the polymer matrix, we use an electron and hole blend polymer as the matrix material for quantum dot. TFB and F8BT are dissolved in toluene at a concentration of 24mg/ml respectively. Then the two solutions are mixed at 1:1 volume ratio to yield a polymer blend solution. Following the polymer solution mixture, a 6mg/ml quantum dot solution is added with the same volume as the polymer mixture solution, resulting in a final solution with a weight concentration of 6mg/ml: 6mg/ml: 3mg/ml for TFB: F8BT: quantum dot. The total blend solution is spin-coated on the PEDOT:PSS hole injection layer, and an Al cathode is deposited on top. Figure 5-2(a) shows the band alignment of the materials in device. Electrons are injected into quantum dot through the F8BT component in the polymer matrix, and holes are injected into quantum dot through the TFB hole transport polymer in the matrix. From this configuration, it is clear that only the quantum dot located at (or within exciton diffusion length from) the electron and hole transport polymer interface can effectively accept both electron and hole to emit. Assuming the quantum dots are distributed homogeneously in the polymer matrix, a large portion of quantum dot deep inside of each mono-polymer phase would therefore be inactive. Moreover, the incorporated quantum dot can have detrimental effect on the device and polymer host material transport property. As in figure 5-2 (b), the device current level is low due to reduced thin film conductivity, and the device turn on voltage is above 5V.

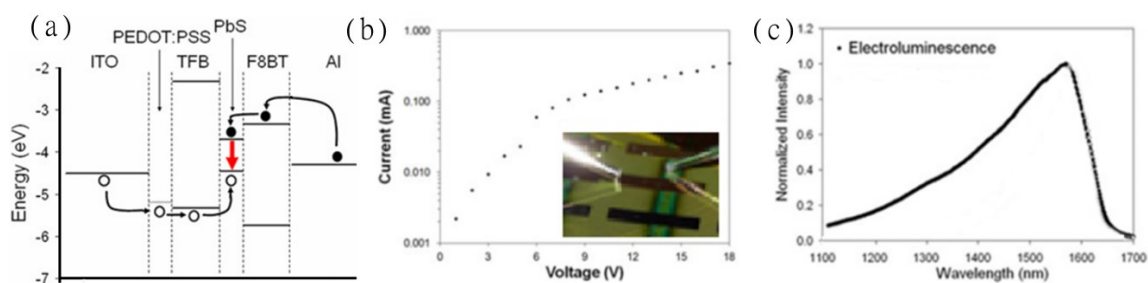


Figure 5-2: (a) Energy diagram for the materials used in the blend hybrid multilayered LED, (b) the I-V characteristics of blend hybrid device, and (c) the device electroluminescence [9].

To verify the consequences of the PbS quantum dots incorporation, we used confocal fluorescence mapping of blended TFB:F8BT films with and without the colloidal quantum dots. The visible emission intensity maps (collected with a silicon detector) shown in Figure 5-3 reveal the domain structure for the blended films with and without quantum dots. The bright regions indicate highly ordered fluorescent polymer domains. With colloidal dots, Figure 5-3(b) shows significantly smaller ordered crystalline phase compared with the same blended film without near-infrared colloidal quantum dots impregnation (Fig. 5-3a).

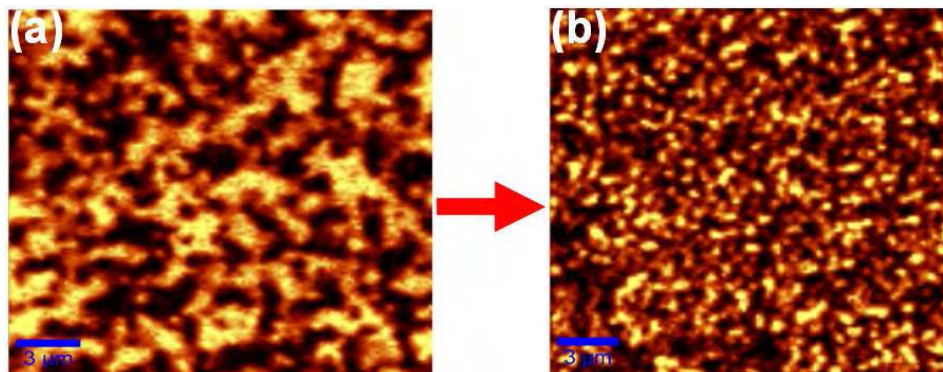


Figure 5-3: The consequences of quantum-dot incorporation on blended polyfluorene-based film structures. Confocal fluorescence mapping of the domain structure for the same toluene blended TFB:F8BT (a) without PbS quantum dots and (b) impregnated with PbS quantum dots. The scale bars are 3  $\mu\text{m}$  [9].

As discussed in chapter 3, polymers thin films are known to consist of crystalline domains surrounded by amorphous chains. From Figure 5-3, incorporation of quantum dot reduces the degree of crystallinity and the organization of in polymer thin film.

In an electrospun polymer nanofiber with nanoparticle incorporation, we further proved the consequences of nanoparticle on the polymers chain alignment. Using a split collector during the electrospinning, it is possible to align those polymer fibers across the collector gap as shown in Figure 5-4 (a). However, the incorporation of inert silica nanoparticles inside the polymer fibers disrupts this orientational ordering and yields a randomized polycrystalline structure such as shown in Figure 5-4 (b). Indeed, the dichroic ratio of the hybrid fiber decreases as nanoparticle concentration increases. The dichroic ratio of the electrospun nanofiber is measured

by its interaction with circular polarized light and defined as the ratio of parallel and perpendicular configuration absorption:

$$DR = \frac{A_{\parallel}}{A_{\perp}} = \frac{\ln\left(\frac{I_0}{I}\right)_{\parallel}}{\ln\left(\frac{I_0}{I}\right)_{\perp}} \quad (5-1)$$

where  $A$  is the absorption measured for orthogonal parallel and perpendicular polarizations with respect to the fibers axis and is defined as the ratio of incident and transmitted intensities for both polarizations.

As for the pristine electrospun nanofiber, the well aligned polymer chain in the fiber axis resulting in stronger absorption in parallel light component, therefore a high dichroic ratio. Upon the addition of nanoparticles, a significantly reduced dichroic ratio is observed, indicating that the introduction of nanoparticle perturbs the orientational ordering of polymer crystalline domains[10]. As being investigated in chapter 3, the reduced crystalline phase can have very detrimental consequences on the optoelectronic properties of the polyfluorene-based device architectures incorporated with high concentrations of quantum dots.

Based on these results, we conclude that incorporation of nanoparticle in polymer thin film can disturb the polymer chain alignment in the thin film, hampering the transport property of the blend thin film and causing low conductivity and a high turn on voltage for device based on blend configuration.

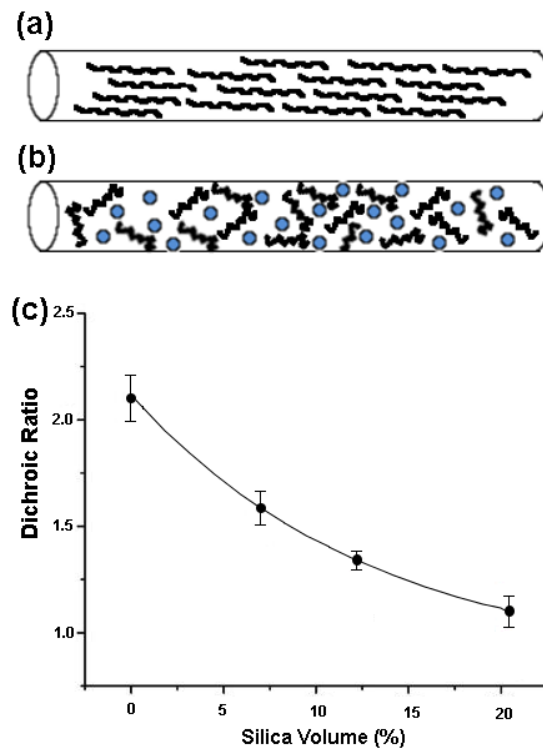


Figure 5-4: Nanoparticle incorporation reduces polymer chain arrangement in electron-spun nanofibers. Schematic (not drawn to scale) showing oriented crystallite arrangement within the fibers without nanoparticles (a) and with nanoparticles (b). The white spaces between the polymer crystallites represent regions of amorphous polymer domains. (c) Dichroic ratio dependence on the silica volume density. [10]

### 5.3 Bi-Layer Polymer/Quantum Dot Hybrid LED with Ligand Exchange Quantum Dot Solid Thin Films

#### 5.3.1 Introduction

The synthesis of exotic lead-chalcogenide nanostructures and their self-assembly into more complex monolayers (2D) and nanocrystalline film structures (3D) has created an entirely new paradigm in low-cost and high-performance optoelectronic materials research, largely due to the facile solution-based processing

and the large versatility of these structures [11]–[13]. Recently, the dithiol-based ligand-exchange has enabled high-quality self-assembled PbS and PbSe lead-chalcogenide nanocrystalline film structures [14]. In this ligand-exchange process, short cross-linking molecules producing strong thiolate group on each end are used to replace the oleate capping group around colloidal nanocrystals to achieve the cross-linking of the nanocrystals into films. High structural quality and excellent electronic transport properties have propelled these self-assembled nanocrystalline lead-chalcogenide film structures to the forefront of cutting-edge research in the area of low-cost photovoltaic and photodetector platforms [15]–[19]. Meanwhile, close-packed and cross-linked CdSe-based nanocrystalline film structures have significantly improved the performances of hybrid light-emitting diodes (LEDs) for the visible [20]–[22]. However, very few reports have explored the potential use of dithiol-treated lead-chalcogenide nanocrystalline films for near-infrared light emitting diodes (LEDs) architectures. Due to the long oleate capping ligands keeping lead-chalcogenide nanocrystals stable in solution, previously proposed hybrid near-infrared LED structures mostly relied on nanocrystals embedded within a polymer host matrix [4], [23], or on a monolayer of nanocrystals sandwiched between organic carrier-transporting layers [6]. In these structures, the low density of nanocrystals and the significant carriers and exciton losses to visible residual emission from the organic layers severely limit the performances of those near-infrared LEDs [6], [23]. Therefore, introducing highly conductive cross-linked lead-chalcogenide quantum dot into hybrid device structure becomes a promising approach for near-IR LED application.

In this report, we apply a 1,3-benzenedithiol (BDT) cross-linking treatment to achieve an all-solution, robust, and versatile pathway to produce hybrid polymer-nanocrystal multilayered-heterostructure LEDs with high near-infrared emission and no residual visible emission. In our multilayered device architecture summarized in Figure 5-5, the electron-transporting layer consists of a 100 nm-thick self-assembled PbS nanocrystalline film cross-linked by BDT ligand-exchange treatment that was deposited on top of a hole-transporting polymer, TFB, film. The nanocrystalline film structure is fabricated using layer-by-layer deposition and ligand exchange treatment to achieve superior structural quality and good charge-transport properties. As we show, the resulting nanocrystalline film provides an efficient electron-transporting and light-emitting structure. In contrast, we observed that another popular dithiol molecule 1,2-ethanedithiol (EDT) leads to poor LED efficiencies in the same device structure. Finally, examining the conductivities and hole mobilities of these dithiol-treated PbS nanocrystalline films provides a deeper understanding of the intricacies associated with those two popular yet complex self-assembly processes using EDT [15], [17] and BDT [14], [16], [19] linkers.

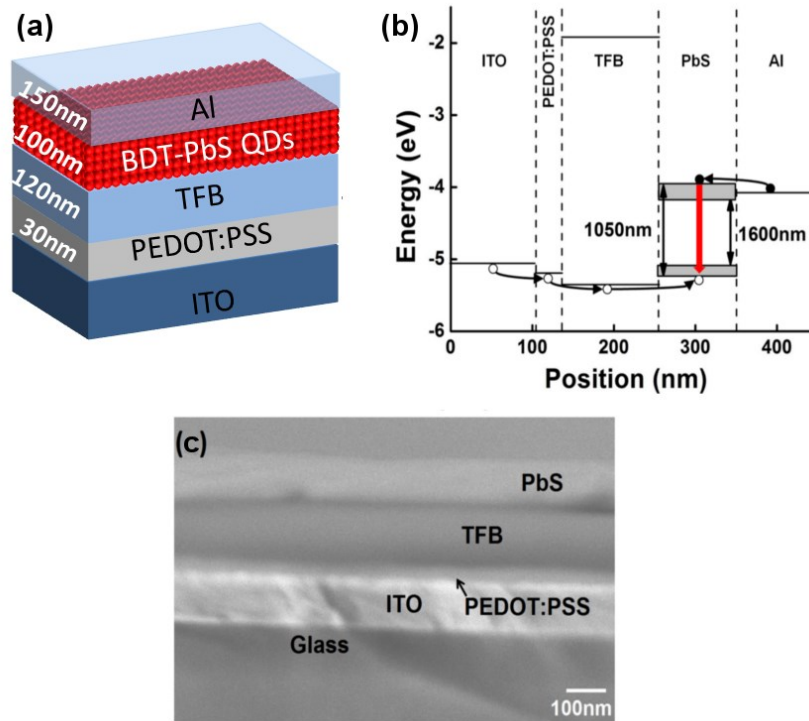


Figure 5-5: Multi-layered polymer/quantum dot hybrid device structure. (a) Schematic demonstration of device configuration. (b) Energy diagram for the hybrid multilayered LED. The HOMO and LUMO levels for the TFB are obtained from Ref. [24]. The band edges for PbS nanocrystals are obtained from Ref. [25]. (c) Cross-sectional SEM image of device without the top aluminum contact. [26]

### 5.3.2 Material and Methods

The PbS nanocrystals used in this paper are synthesized using the method pioneered by Hines et al [27]. The near-infrared LED device consists of a multilayered structure using indium-tin-oxide (ITO) as the anode, poly(3,4-ethylenedioxythiophene):poly(styrenesulphonate) (or PEDOT:PSS) as the hole injection layer, poly(2,7-(9,9-di-n-octylfluorene)-alt-(1,4-phenylene-((4-sec-

butylphenyl)imino)-1,4-phenylene)) (or TFB) as the hole transporting layer, cross-linked PbS nanocrystals as electron transporting and light emitting layer, and aluminum (Al) as the cathode. To prepare the samples, the ITO substrate ( $R_s=15-25$  ohms, Delta Technologies) is first pre-patterned by photolithography followed by a wet-etching in 20% hydrochloric acid solution. The substrate is then sequentially cleaned in de-ionized water, acetone, and isopropanol ultrasonic baths each for 15 min. The hole-injection layer of PEDOT:PSS (CLEVIOS™ P VP Al 4083) is spin-coated on top of the ITO substrate at 3000 rpm for 90 seconds and then annealed at 135°C for 30 minutes in air. The layer of TFB (American Dye Source, Inc.) is spin-coated atop the PEDOT:PSS film using toluene solutions with different TFB concentrations (8 mg•ml<sup>-1</sup>, 12 mg•ml<sup>-1</sup> and 16 mg•ml<sup>-1</sup>) for thickness optimization. After annealing at 150°C for 10 min in a nitrogen-purged oven, the TFB film thickness is measured to be  $60 \pm 15$  nm,  $90 \pm 15$  nm and  $120 \pm 15$  nm respectively for the three concentrations used. Subsequently, a layer-by-layer spin-coating of hexane-based colloidal solutions of PbS nanocrystals (about 10 mg•ml<sup>-1</sup> concentrations) is processed directly atop the TFB. The deposition of each layer of nanocrystals includes 3 steps: 1) spin-coating of the colloidal nanocrystals solution at 2000 rpm for 30 seconds, 2) Deposition of several drops of the 1,3-benzenedithiol (BDT) acetonitrile solution (0.02 M) to fully cover the substrate, wait for 30 seconds to enable the exchange process before spin-coating for 30 seconds at 2000rpm, 3) Rinsing the sample with hexane during spinning to wash away any excess of PbS nanocrystals and BDT residues. Devices with 2, 4, 6, and 8 layers (with roughly 25 nm per layer) of nanocrystals were produced using this method to investigate the optimal electron-transporting layer's thickness. Finally, a 150 nm-thick Al cathode is deposited through a shadow mask by

e-beam evaporation at a rate of  $1 \text{ \AA}\cdot\text{s}^{-1}$ . No further treatment and/or encapsulation is performed on the devices. To avoid trapping states formation at the contact between Al and nanocrystals after long term air exposure [28], all devices are tested within two hours after fabrication, and no current-drop is observed in this time scale.

The TEM images are obtained using a JEM 2010F instrument operating at 200 KeV. The SEM images are obtained using a JSM-7400F field-emission SEM instrument operating at an acceleration voltage of 3 kV. Photoluminescence (PL) and electroluminescence (EL) spectra are recorded using a Jobin-Yvon iHR320 triple-grating spectrometer equipped with a Symphony thermoelectric-cooled InGaAs CCD array for the near-infrared and a Synapse silicon CCD array for the visible. For photoluminescence excitation, we use a 250 mW frequency-stabilized TORUS (Laser-Quantum, Inc.) laser operating at 532 nm. Electroluminescence excitation is performed using a Keithley 236 source-measure unit. The device power-current-voltage (PIV) device characteristics are recorded by placing the device on the port of an integrating sphere coupled to a Newport IR-818 photodetector. The integrating sphere is carefully calibrated using a lambertian GaInN LED. Absorption measurements are performed on a UV-VIS-NIR spectrometer (UV-3600, Shimadzu) and the near-infrared image of the device's emission is collected by Xenicsxeva near-infrared camera coupled to a  $2\times$  magnifier. For the measurement of conductivity and hole mobility of the PbS nanocrystalline film by CELIV method, the sample consists of a 250 to 350 nm nanocrystalline film fabricated using the layer-by-layer spin-coating method sandwiched directly between ITO and Al contact. A linearly-increasing bias is applied using a function generator (Agilent 33220A) at 20 MHz and the transient currents are measured by recording the voltage drop across a  $200\Omega$

resistive load using a digital oscilloscope (Agilent 54621A). All measurements are performed at room temperature.

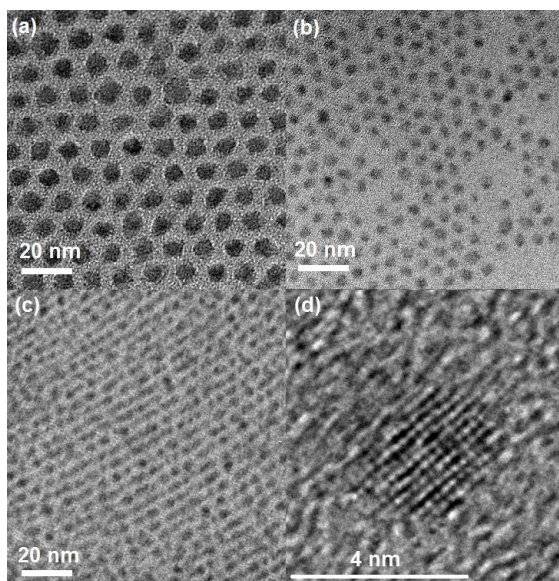


Figure 5-6: TEM images of quantum dots with different sizes. (a) 7nm, (b) 5 nm and (c) 3.5 nm PbS colloidal nanocrystals observed under TEM. (d) Lattice structure of a single 3.5 nm nanocrystal under high-resolution TEM (HRTEM). [26]

### 5.3.3 Hybrid Near-Infrared LED Structure With BDT Linker

As shown in Figure 5-7, a TFB polymer-only device with no nanocrystalline film displays a clear single carrier (hole) trap-limited current regime between 1 and 2 Volts [29], before reaching a quasi space-charge-limited current regime with slope  $m \approx 2.7$ . This single carrier behavior is consistent with the large energy barrier between the HOMO of the TFB and the aluminum cathode for electron injection. For the LED device using the optimized BDT cross-linked nanocrystalline film structure atop the TFB, measurements indicate a high current density at low voltages originating from

the efficient electron injection at the nanocrystal-aluminum junction. As shown in Figure 5-5(b), the good match between the aluminum cathode's work function and the conduction band of the self-assembled nanocrystalline layer offers the convenience of removing additional electron transporting organic and/or low work function metal layers in-between. This precludes additional carrier losses and unwanted visible luminescence, while simplifying the fabrication process and providing better device stability. At the heterojunction between hole-transporting layer and electron-transporting BDT-treated PbS nanocrystalline layer, the low LUMO of the TFB provides a fantastic electron barrier that efficiently confines the electrons within the PbS nanocrystalline film structure and thus prevents any light emission from the polymer layer during device operation.

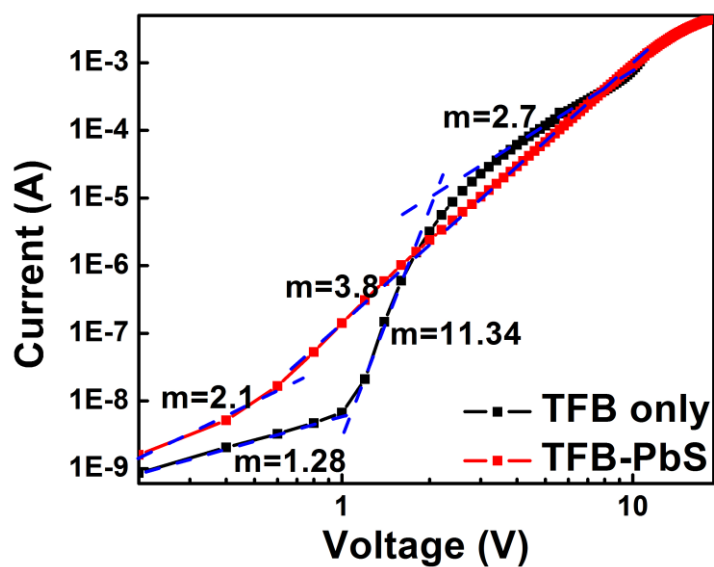


Figure 5-7: Current-voltage characteristics for the hybrid multilayered LED using a BDT-treated nanocrystalline film and for a TFB polymer-only control device. [26]

In Figure 5-8, we display the external quantum efficiency (EQE) and output power measurements for devices with different TFB and nanocrystalline film thicknesses. As shown in Figure 5-8(a), the EQE and output powers of the devices increase along with increasing the thickness of the hole-transporting TFB layer, while keeping the same  $100 \pm 15$  nm nanocrystalline film thickness. This is consistent with the dual role of the TFB layer which consists in: (1) providing an efficient electron barrier to confine the injected electrons at the polymer/nanocrystals interface and favor exciton binding, and (2) limiting the excess hole-current flowing through the entire device structure. However, increasing the polymer layer's thickness also increases the device's turn-on voltage from about 2V for the 60 nm- and 90 nm- thick TFB films to 3.4V for the 120 nm-thick TFB film.

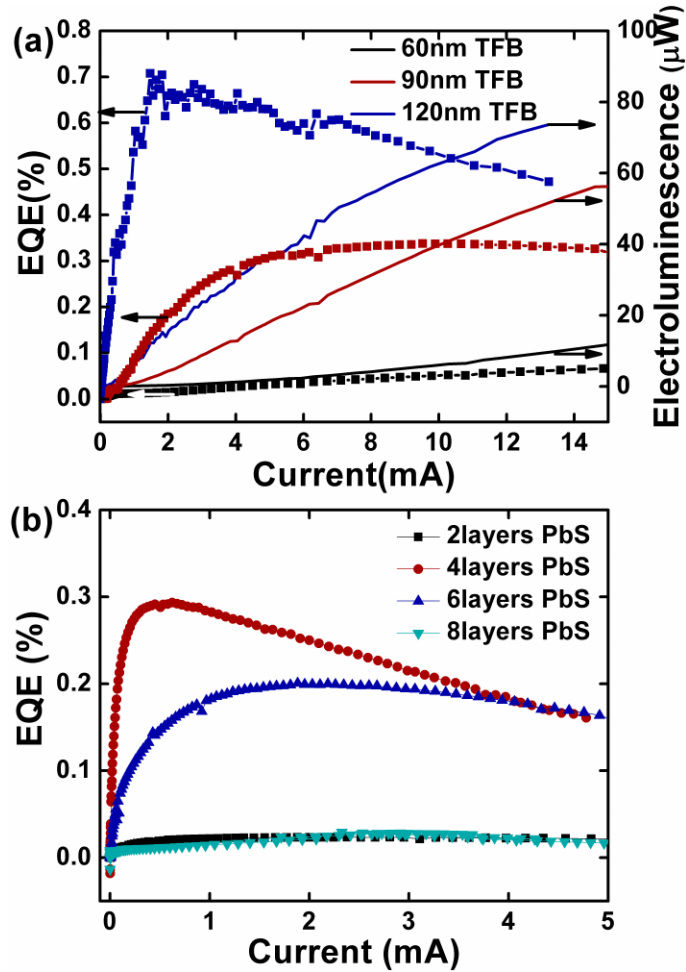


Figure 5-8: Electron and hole transporting layer optimization in hybrid device structures. (a) EQE and emitted power characteristics from samples with different TFB-layer thicknesses. These identical  $100 \pm 15$  nm nanocrystalline film structures all emit at 1050 nm. (b) EQE characteristics from samples with different nanocrystalline film thicknesses using identical 120 nm-thick TFB layer. Each nanocrystal layer is 25 nm-thick. This group of samples operates at 1150 nm. This batch of nanocrystals has a slightly lower photoluminescence efficiency compared with the nanocrystals in (a). [26]

Based on these results, we decided to use a 120 nm-thick TFB layer for the nanocrystalline layer optimization shown in Figure 5-8(b), as it provides the optimal

output powers and EQEs. There, multiple spin-coated layers obtained from the same solution of nanocrystals emitting at 1150 nm were used for comparison. Due to a lower photoluminescent efficiency of the 1150nm emitter nanocrystals, this batch of samples has a lower device EQE than the devices in Figure 5-8(a). With each nanocrystals layer being 25 nm-thick, the EQE peaks with devices using 4 layers of nanocrystalline film ( $100 \pm 15$  nm thick). For thinner nanocrystalline films (2 layers), the active region is too thin and the metal contact quenching leads to lower EQEs. In thicker structures (4 layers), the exciton diffusion to the contact is reduced, which leads to an increase in radiative recombination. Further increasing the thickness of the nanocrystalline film to 6 and 8 layers results in lower EQEs that we attribute to electrons trapping in defect states [30] before reaching the polymer/nanocrystalline film interface, thus reducing the carrier balance in the active region. As shown in Figure 5-8, this all-solution-processed device architecture can produce  $5 \text{ mm}^2$  near-infrared LEDs producing up-to a phenomenal  $74 \mu\text{W}$  output power at 1050nm and EQE's up-to 0.72%. Meanwhile, no residual visible emission from the hole transporting polymer layer is observed, as shown in Figure 5-9(a). Finally, Figure 5-9(b) shows that near-infrared LED architectures operating at different emission wavelengths can be produced using PbS nanocrystals of different sizes, demonstrating the versatility of this approach.

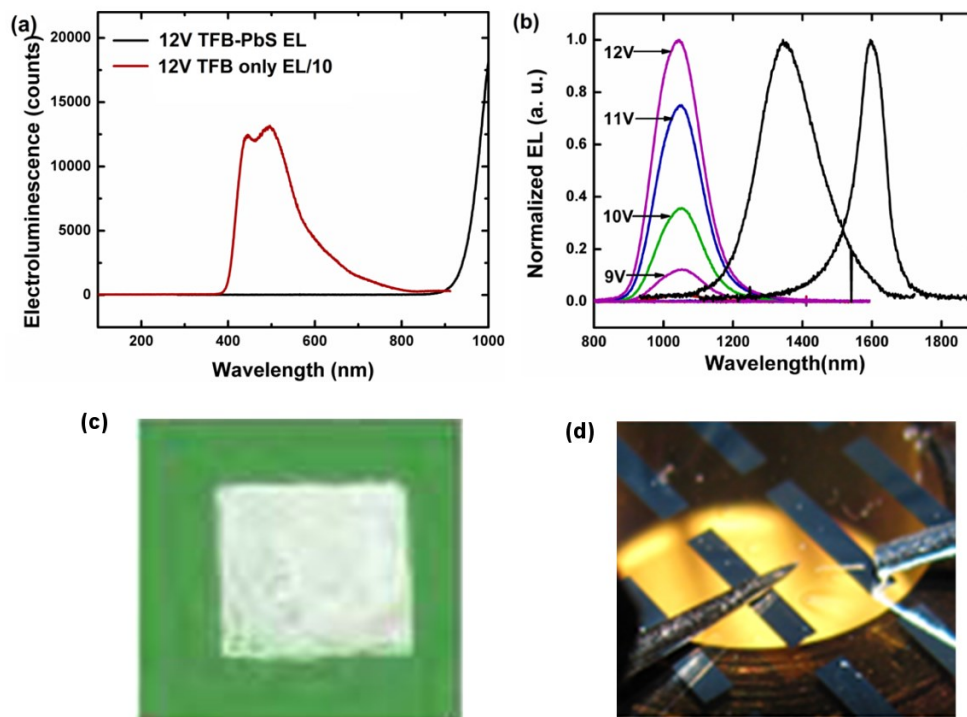


Figure 5-9: Hybrid near-IR device performance demonstration. (a) Visible electroluminescence spectra from a TFB-only LED and a TFB-PbS hybrid LED. While some of the near-infrared emission is seen at the edge of the detection range of silicon CCD array, no TFB emission can be seen from the hybrid LED structure. (b) Normalized electroluminescence spectra for LED structures fabricated from nanocrystalline films using different PbS nanocrystals with emission at 1050, 1350 and 1600 nm respectively. The narrowing shown on the right shoulder of 1600nm spectrum is due to InGaAs detector sensitivity cut-off. (c) The infrared image of the device and (d) the device photograph. [26]

### 5.3.4 EDT Vs. BDT Cross-Link for LED Application

On the choosing of the best dithiol treatment for the LED structure, we noticed significant differences between the nanocrystalline film structures obtained using the BDT-treatment and the more conventional EDT-based cross-linking process. While the EDT treatment is known to work well for photovoltaic devices [15], [17], [31], it

consistently provided us with poor near-infrared LED structures. For example, Figure 5-10 (a) compares the power-voltage device characteristic of three identical devices with EDT-treated, BDT-treated and pristine un-treated nanocrystalline films. It is clear that the electroluminescence is dramatically lower for the EDT-treated film compared with BDT in Figure 5-10 (b). In the absorption and photoluminescence spectra shown in Figure 5-10 (c), the red shifts after both dithiol treatments suggest reduction of quantum confinement and stronger coupling originating from the reduced inter-particle distance following both of these dithiol-based cross-linking treatments [15], [32]. While the three samples have the same number of layers, the photoluminescence is significantly higher for the BDT-treated film compared with EDT, which is consistent with the higher electroluminescence consistently observed from the BDT-treated devices. Estimated using the ratio between the absorption at the excitation wavelength and the photoluminescence intensities, the relative photoluminescence efficiency for un-treated, BDT, EDT-nanocrystalline films is 1, 1.3 and 0.15 respectively. This shows clearly that although both BDT and EDT cross-linking result in nanocrystalline films with better charge transport properties useful for photodetector and photovoltaic applications [15]–[19] than un-treated quantum dot film, the distinct improvements in photo- and electro-luminescence efficiency after BDT treatment suggests a significant reduction of non-radiative recombination pathways that is crucial for light-emitting applications.

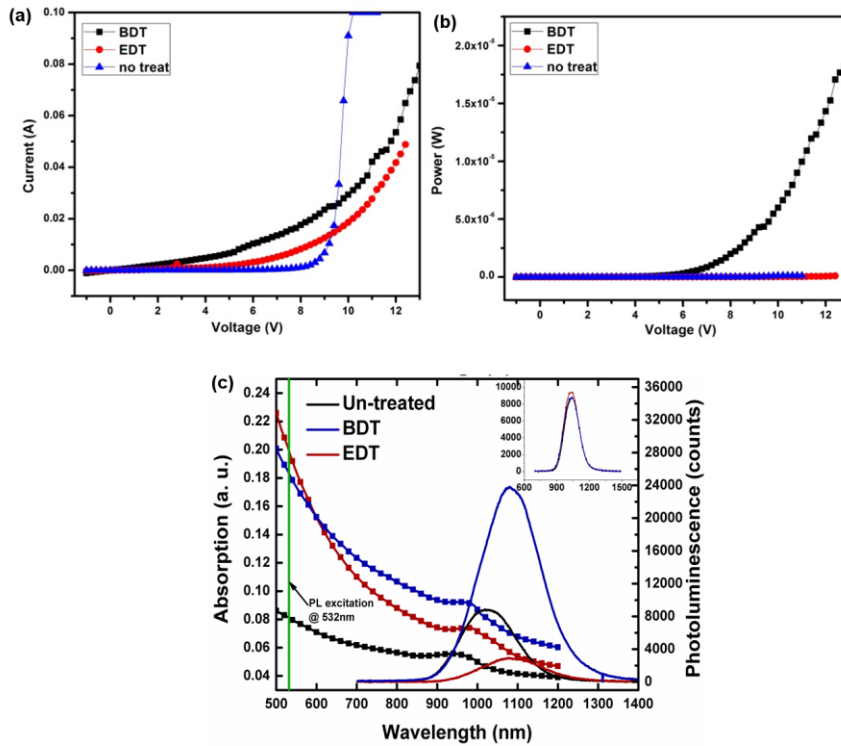


Figure 5-10: Properties comparison for devices with different quantum dots ligands. PIV characteristics for un-treated, BDT- and EDT- treated nanocrystalline device. (a) IV characteristics and (b) Output power-evolution characteristics. (c) shows the thin films absorption and fluorescent spectra under different quantum dot ligand treatment. Inset shows the three thin films before ligand exchanges have comparable fluorescence intensity. [26]

To further understand the different device performance between BDT and EDT treatment, the established charge extraction in linearly increasing voltage (CELIV) and time-of-flight (TOF) methods were used to measure the equilibrium conductivity, hole and electron mobilities.

For CELIV measurements, the samples use a 250~350 nm nanocrystalline films fabricated using the layer-by-layer spin coating method between ITO and Al contacts. A linearly-increasing bias is applied by a function generator (Agilent 33220A) on the sample and the transient currents are measured by the voltage drop across a 200 Ohms resistive load by a digital oscilloscope (Agilent 54621A). The conductivities can be calculated by using [17]:

$$\sigma = \frac{3}{2} \frac{d\Delta j}{t_{\max}A} \quad (5-2)$$

and the hole mobility is calculated according to [17]:

$$\mu_h = \frac{2d^2}{3At_{\max}^2(1+0.36\frac{\Delta j}{j(0)})} \quad (5-3)$$

in the equations,  $d$  is the sample thickness,  $A$  is the voltage-increase slope. The parameters  $t_{\max}$ ,  $\Delta j$  and  $j(0)$  are obtained directly from the CELIV measurements shown in Figure 5-11.

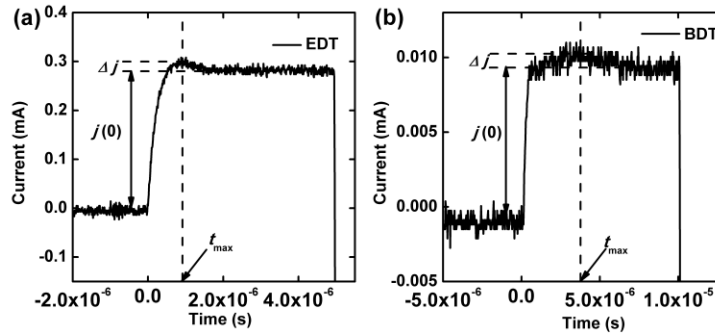


Figure 5-11: CELIV transient currents measurement results. EDT- (a) and BDT- (b) treated films. In (a),  $d = 250\text{nm}$ ,  $A = 400\text{KV/s}$ , and in (b) for BDT sample,  $d = 320\text{nm}$ ,  $A = 300\text{KV/s}$ . [26]

Using the measurement parameters given in Fig. 5-11, we obtain  $1.56 \times 10^{-11} \text{S/m}$  and  $1.1 \times 10^{-3} \text{cm}^2 \text{V}^{-1} \text{s}^{-1}$  for the conductivity and hole mobility in EDT-treated nanocrystalline films and  $3.91 \times 10^{-13} \text{S/m}$  and  $1.4 \times 10^{-4} \text{cm}^2 \text{V}^{-1} \text{s}^{-1}$  with BDT treatment.

For TOF measurements, the samples have the same structure as for the CELIV samples but with a much thicker nanocrystalline layer (1100~1200 nm) formed using more concentrated quantum dot solutions and more spin-coat cycles (>20). The 532 nm second-harmonic of a Brilliant Q-switched Nd:YAG laser (Quantel) with 5 ns pulses is used to excite the samples from the ITO side while a reverse-bias is applied on the sample to extract the photo-generated minority carriers (electrons) to transport through the whole thickness and be collected at Al contact. The transient current is recorded by the voltage drop across a 200 Ohms resistive load by a digital oscilloscope (Agilent 54621A). The electron mobility can be directly obtained as [18]:

$$\mu_e = \frac{d^2}{V\tau} \quad (5-4)$$

where  $d$  is the sample thickness,  $V$  the applied voltage on the film,  $\tau$  the transit time obtained from the measurements shown in Figure 5-12. There, we can observe a shorter transit time for the BDT-treated samples. After inclusion of the different voltages (15 Volts for the EDT-treated film and 27 Volts for the BDT-treated film) and film thicknesses (1200nm for EDT-treated film and 1100nm for the BDT-treated film), into calculation, the resulting electron mobility obtained for the BDT-treated nanocrystalline films is  $5.6 \times 10^{-3} \text{cm}^2 \text{V}^{-1} \text{s}^{-1}$ , compared with  $3.3 \times 10^{-3} \text{cm}^2 \text{V}^{-1} \text{s}^{-1}$  for the EDT-treated film.

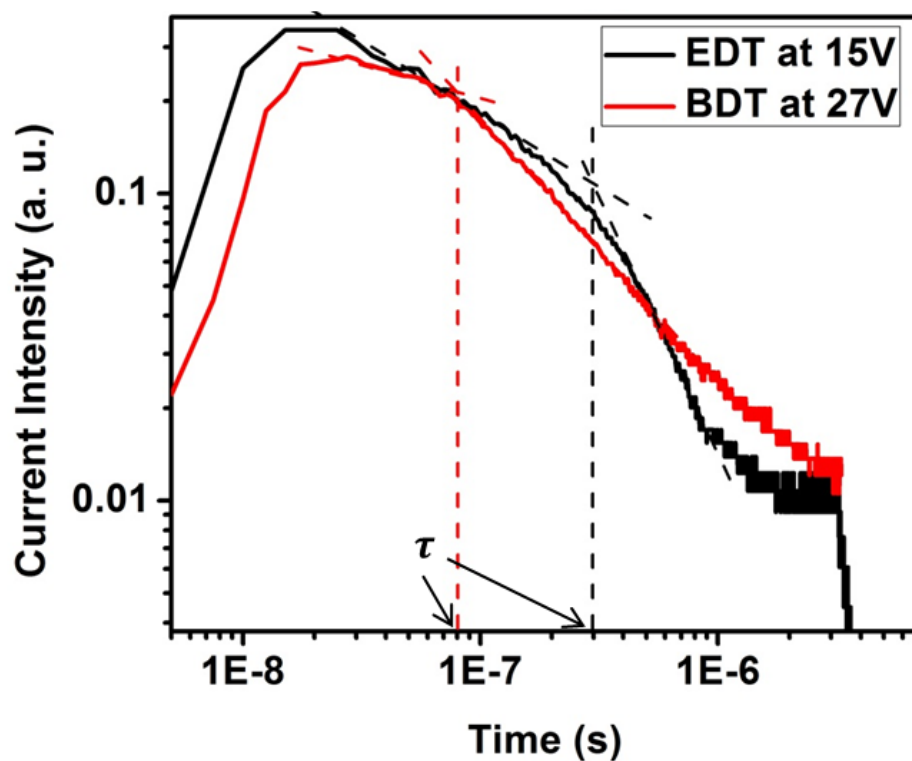


Figure 5-12: TOF transient current measurements for EDT- and BDT-treated films. Because of the large DC hole current, the voltage applied on the EDT-treated sample can only go to 15V before it breaks. For the BDT-treated sample, no clear slope transit point was observed below 27V. This difference in voltage is accounted-for in Equation (5-4) [9].

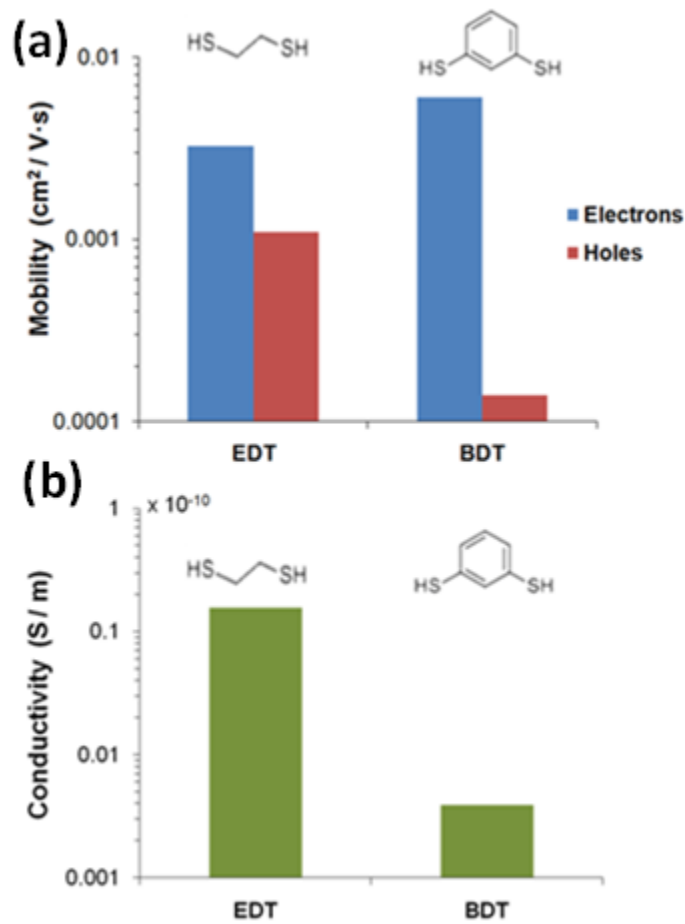


Figure 5-13: Summary of electronic properties of EDT and BDT cross-linked quantum dot thin films. (a) the electron and hole mobility comparison, (b) conductivity comparison. [9]

Table 5-1: Comparison of the conductivity, hole- and electron mobilities for EDT- and BDT- treated nanocrystalline films

	Conductivity (S/m)	Hole mobility (cm <sup>2</sup> V <sup>-1</sup> s <sup>-1</sup> )	Electron mobility (cm <sup>2</sup> V <sup>-1</sup> s <sup>-1</sup> )
EDT	1.56×10 <sup>-11</sup>	1.2×10 <sup>-3</sup>	3.3×10 <sup>-3</sup>
BDT	3.91×10 <sup>-13</sup>	1.7×10 <sup>-4</sup>	5.6×10 <sup>-3</sup>

Figure 5-13 and Table 5-1 summarized the results above, it appears that: (1) a lower free-carrier density for the BDT-treated films due to a much lower doping concentration and a good surface passivation significantly reduce Auger recombination and other non-radiative processes, (2) when we use the cross-linked nanocrystalline film as the ETL due to its higher electron mobility than hole mobility, a much lower hole mobility in BDT than in EDT nanocrystalline film provides a good mobility barrier that confines hole at the heterojunction interface and favors exciton binding, and (3) meanwhile, a good electron mobility for the BDT-treated films improves the electron injection when use it as the ETL, these combined factors explain the significantly better performances for our BDT-treated LED structures.

#### **5.4 Conclusion**

We report an all solution-based processing method producing efficient hybrid polymer-nanocrystal multilayered heterostructures for light-emission in the near-infrared (1050-1600 nm), using a carefully-controlled layer-by-layer BDT cross-linking nanocrystal treatment. After optimization of the hole- and electron-transporting layers thicknesses to 120 and 100 nm respectively, we obtain near-infrared LEDs with EQEs of 0.72% and up-to 74  $\mu$ W output power at 1050nm. The high near-IR emission and no residual visible emission of this device architecture are achieved by using a thick cross-linked nanocrystalline film acting both as the electron-transporting layer and the electroluminescent material. As we show, the good performances of this BDT-treated LED structure compared with the more conventional EDT treatment can be explained by the different surface passivations, doping levels and carrier mobilities resulting from the BDT and EDT treatments. This facile, robust, low-temperature and substrate-independent all solution-processed LED

architecture provides a scalable method of producing near-infrared LEDs allowing integration on flexible substrates and amorphous silicon active matrix backplanes [33]. In the future, this LED architecture could be potentially used for flexible and/or reconfigurable integrated opto-electronics, biological imaging and sensing, and lab-on-a-chip platforms [34]. Meanwhile, this approach could also be extended to PbSe colloidal nanocrystal to further extend the LED operation further in the near- and mid-infrared ranges. Finally, the large refractive index of these self-assembled nanocrystalline films also offers the possibility of incorporating electroluminescent structures onto silicon substrates or within more complex device architectures.

## REFERENCES

- [1] Q. Sun, Y. A. Wang, L. S. Li, D. Wang, T. Zhu, J. Xu, C. Yang, and Y. Li, “Bright, multicoloured light-emitting diodes based on quantum dots,” *Nat. Photonics*, vol. 1, no. 12, pp. 717–722, 2007.
- [2] B. S. Mashford, T.-L. Nguyen, G. J. Wilson, and P. Mulvaney, “All-inorganic quantum-dot light-emitting devices formed via low-cost, wet-chemical processing,” *J. Mater. Chem.*, vol. 20, no. 1, p. 167, 2010.
- [3] B. S. Mashford, M. Stevenson, Z. Popovic, C. Hamilton, Z. Zhou, C. Breen, J. Steckel, V. Bulovic, M. Bawendi, S. Coe-Sullivan, and P. T. Kazlas, “High-efficiency quantum-dot light-emitting devices with enhanced charge injection,” *Nat. Photonics*, vol. 7, no. 5, pp. 407–412, Apr. 2013.
- [4] K. R. Choudhury, D. W. Song, and F. So, “Efficient solution-processed hybrid polymer–nanocrystal near infrared light-emitting devices,” *Org. Electron.*, vol. 11, no. 1, pp. 23–28, Jan. 2010.
- [5] S. Coe-Sullivan, J. S. Steckel, W. K. Woo, M. G. Bawendi, and V. Bulovic, “Large-area ordered quantum-dot monolayers via phase separation during spin-casting,” *Adv. Funct. Mater.*, vol. 15, no. 7, pp. 1117–1124, 2005.
- [6] J. S. Steckel, S. Coe-Sullivan, V. Bulović, and M. G. Bawendi, “1.3 $\mu\text{m}$  to 1.55 $\mu\text{m}$  Tunable Electroluminescence from PbSe Quantum Dots Embedded within an Organic Device,” *Adv. Mater.*, vol. 15, no. 21, pp. 1862–1866, Nov. 2003.
- [7] P. O. Anikeeva, J. E. Halpert, M. G. Bawendi, and V. Bulović, “Electroluminescence from a mixed red-green-blue colloidal quantum dot monolayer,” *Nano Lett.*, vol. 7, no. 8, pp. 2196–200, Aug. 2007.
- [8] S. Coe-Sullivan, W. K. Woo, J. S. Steckel, M. Bawendi, and V. Bulović, “Tuning the performance of hybrid organic/inorganic quantum dot light-emitting devices,” *Org. Electron.*, vol. 4, no. 2–3, pp. 123–130, 2003.
- [9] S. Cloutier, *Advanced Photonic Sciences*, no. 1. InTech, 2012, pp. 178–196.

- [10] N. Sharma, S. J. McKeown, X. Ma, D. J. Pochan, and S. G. Cloutier, "Structure-property correlations in hybrid polymer-nanoparticle electrospun fibers and plasmonic control over their dichroic behavior.," *ACS Nano*, vol. 4, no. 10, pp. 5551–8, Oct. 2010.
- [11] D. V Talapin and C. B. Murray, "PbSe nanocrystal solids for n- and p-channel thin film field-effect transistors.," *Science*, vol. 310, no. 5745, pp. 86–9, Oct. 2005.
- [12] G. Konstantatos, I. Howard, A. Fischer, S. Hoogland, J. Clifford, E. Klem, L. Levina, and E. H. Sargent, "Ultrasensitive solution-cast quantum dot photodetectors.," *Nature*, vol. 442, no. 7099, pp. 180–3, Jul. 2006.
- [13] S. A. McDonald, G. Konstantatos, S. Zhang, P. W. Cyr, E. J. D. Klem, L. Levina, and E. H. Sargent, "Solution-processed PbS quantum dot infrared photodetectors and photovoltaics.," *Nat. Mater.*, vol. 4, no. 2, pp. 138–42, Feb. 2005.
- [14] J. M. Luther, M. Law, Q. Song, C. L. Perkins, M. C. Beard, and A. J. Nozik, "Structural, optical, and electrical properties of self-assembled films of PbSe nanocrystals treated with 1,2-ethanedithiol.," *ACS Nano*, vol. 2, no. 2, pp. 271–80, Feb. 2008.
- [15] G. I. Koleilat, L. Levina, H. Shukla, S. H. Myrskog, S. Hinds, A. G. Pattantyus-Abraham, and E. H. Sargent, "Efficient, stable infrared photovoltaics based on solution-cast colloidal quantum dots.," *ACS Nano*, vol. 2, no. 5, pp. 833–40, May 2008.
- [16] E. J. D. Klem, H. Shukla, S. Hinds, D. D. MacNeil, L. Levina, and E. H. Sargent, "Impact of dithiol treatment and air annealing on the conductivity, mobility, and hole density in PbS colloidal quantum dot solids," *Appl. Phys. Lett.*, vol. 92, no. 21, p. 212105, May 2008.
- [17] J. P. Clifford, G. Konstantatos, K. W. Johnston, S. Hoogland, L. Levina, and E. H. Sargent, "Fast, sensitive and spectrally tuneable colloidal-quantum-dot photodetectors.," *Nat. Nanotechnol.*, vol. 4, no. 1, pp. 40–4, Jan. 2009.
- [18] H. W. Hillhouse and M. C. Beard, "Solar cells from colloidal nanocrystals: Fundamentals, materials, devices, and economics," *Curr. Opin. Colloid Interface Sci.*, vol. 14, no. 4, pp. 245–259, 2009.

- [19] K. Szendrei, W. Gomulya, M. Yarema, W. Heiss, and M. A. Loi, "PbS nanocrystal solar cells with high efficiency and fill factor," *Appl. Phys. Lett.*, vol. 97, no. 20, p. 203501, Nov. 2010.
- [20] K.-S. Cho, E. K. Lee, W.-J. Joo, E. Jang, T.-H. Kim, S. J. Lee, S.-J. Kwon, J. Y. Han, B.-K. Kim, B. L. Choi, and J. M. Kim, "High-performance crosslinked colloidal quantum-dot light-emitting diodes," *Nat. Photonics*, vol. 3, no. 6, pp. 341–345, Jun. 2009.
- [21] W. K. Bae, J. Kwak, J. Lim, D. Lee, M. K. Nam, K. Char, C. Lee, and S. Lee, "Multicolored light-emitting diodes based on all-quantum-dot multilayer films using layer-by-layer assembly method.," *Nano Lett.*, vol. 10, no. 7, pp. 2368–73, Jul. 2010.
- [22] L. Qian, Y. Zheng, J. Xue, and P. Holloway, "Stable and efficient quantum-dot light-emitting diodes based on solution-processed multilayer structures," *Nat. Photonics*, vol. 5, no. September, 2011.
- [23] G. Konstantatos, C. Huang, L. Levina, Z. Lu, and E. H. Sargent, "Efficient Infrared Electroluminescent Devices Using Solution-Processed Colloidal Quantum Dots," *Adv. Funct. Mater.*, vol. 15, no. 11, pp. 1865–1869, Nov. 2005.
- [24] J. Hwang, E.-G. Kim, J. Liu, J.-L. Brédas, A. Duggal, and A. Kahn, "Photoelectron Spectroscopic Study of the Electronic Band Structure of Polyfluorene and Fluorene-Arylamine Copolymers at Interfaces," *J. Phys. Chem. C*, vol. 111, no. 3, pp. 1378–1384, Jan. 2007.
- [25] B.-R. Hyun, Y.-W. Zhong, A. C. Bartnik, L. Sun, H. D. Abruña, F. W. Wise, J. D. Goodreau, J. R. Matthews, T. M. Leslie, and N. F. Borrelli, "Electron injection from colloidal PbS quantum dots into titanium dioxide nanoparticles.," *ACS Nano*, vol. 2, no. 11, pp. 2206–12, Nov. 2008.
- [26] X. Ma, F. Xu, J. Benavides, and S. G. Cloutier, "High performance hybrid near-infrared LEDs using benzenedithiol cross-linked PbS colloidal nanocrystals," *Org. Electron.*, vol. 13, no. 3, pp. 525–531, Mar. 2012.
- [27] M. A. Hines and G. D. Scholes, "Colloidal PbS Nanocrystals with Size-Tunable Near-Infrared Emission: Observation of Post-Synthesis Self-Narrowing of the Particle Size Distribution," *Adv. Mater.*, vol. 15, no. 21, pp. 1844–1849, Nov. 2003.

- [28] J. Tang, X. Wang, L. Brzozowski, D. A. R. Barkhouse, R. Debnath, L. Levina, and E. H. Sargent, "Schottky quantum dot solar cells stable in air under solar illumination.," *Adv. Mater.*, vol. 22, no. 12, pp. 1398–402, Mar. 2010.
- [29] Y. Kim and C.-S. Ha, *Advances in organic light emitting devices*. Trans Tech Publications, 2008.
- [30] G. Sarasqueta, K. R. Choudhury, and F. So, "Effect of Solvent Treatment on Solution-Processed Colloidal PbSe Nanocrystal Infrared Photodetectors," *Chem. Mater.*, vol. 22, no. 11, pp. 3496–3501, Jun. 2010.
- [31] J. M. Luther, M. Law, M. C. Beard, Q. Song, M. O. Reese, R. J. Ellingson, and A. J. Nozik, "Schottky solar cells based on colloidal nanocrystal films.," *Nano Lett.*, vol. 8, no. 10, pp. 3488–92, Oct. 2008.
- [32] J. J. Choi, J. Luria, B.-R. Hyun, A. C. Bartnik, L. Sun, Y.-F. Lim, J. a Marohn, F. W. Wise, and T. Hanrath, "Photogenerated exciton dissociation in highly coupled lead salt nanocrystal assemblies.," *Nano Lett.*, vol. 10, no. 5, pp. 1805–11, May 2010.
- [33] T. Rauch, M. Böberl, S. F. Tedde, J. Fürst, M. V. Kovalenko, G. Hesser, U. Lemmer, W. Heiss, and O. Hayden, "Near-infrared imaging with quantum-dot-sensitized organic photodiodes," *Nat. Photonics*, vol. 3, no. 6, pp. 332–336, May 2009.
- [34] B.-R. Hyun, H. Chen, D. A. Rey, F. W. Wise, and C. A. Batt, "Near-infrared fluorescence imaging with water-soluble lead salt quantum dots.," *J. Phys. Chem. B*, vol. 111, no. 20, pp. 5726–30, May 2007.

## Chapter 6

### HIGH POLYMER-LEDS ENHANCEMENT BY EXCITON-PLASMON COUPLING USING ENCAPSULATED METALLIC NANOPARTICLES

#### 6.1 Introduction

Polymer light emitting diodes (PLEDs) have undergone significant progress in the past two decades [1]. They became more and more attractive for new generations of low-cost novel solid state lighting and flat panel displays due to their unique advantages such as flexibility, large area scalability, high power efficiency and convenient solution based-fabrication process. Many efforts have been invested in improving PLEDs performances and device life-times including the synthesis of novel luminescent materials [2], the use of better multi-layer device architectures [3], [4], and the integration within hybrid organic-inorganic heterostructures [5], [6]. Maintaining their low fabrication cost is a key factor to allow large-scale PLEDs integration and mass-production. In the meantime, the particular properties of surface plasmons (SP) in metallic nanostructures and their interaction with photons and excitons have been gradually unraveled by the tremendous research interests and efforts in this area [7]–[10]. Metallic nano-structures have now been widely used to enhance Raman scattering [7], [8], optical absorption [9], [10] and photoluminescence of fluorescent materials [11]. The phenomenon of SP-enhanced exciton decay rate has also been exploited on organic and inorganic material electroluminescence (EL) [11], offering great promising on improving LED performance [12]–[20].

Surface plasmon modes stem from the collective oscillations of free electrons in metals. It is well understood that flat metal films placed directly atop a fluorescent

material quench excitons by causing exciton dissociation and coupling with the propagating surface plasmon polariton (SPP) mode, which ultimately results in non-radiative thermal loss in the metal film due to a momentum mismatch preventing photon emission [21], [22]. Using GaN quantum wells [11], it was previously demonstrated that two key factors can contribute to switching this metal quenching into phenomenal metal-enhanced luminescence: 1) having a thin spacer layer between the metal film and the luminescent material to prevent exciton dissociation, and 2) using metal nano-structures supporting localized SP modes that can couple with the photon-emission mode [11]. The enhancement is explained by a high electromagnetic density of states  $\rho$  introduced by surface plasmons around the metal structure [23], [24], through which the exciton decay rate is enhanced according to Purcell's theory [25]. Thus, enhanced electroluminescence using noble metal nanoparticles formed by vacuum evaporation and thermal annealing has been successfully observed in GaN-based quantum-well LEDs[12]–[14], Si-based LEDs [15], [16] and small molecule OLEDs [17], [18]. However, the convenient evaporation and annealing method used to create uniform layers with large densities of metallic nanoparticles cannot be easily adapted to polymer-LEDs due to the severe degradation of the conjugated polymers under high annealing temperatures (250 ~ 1000°C) and the device electronic profile changes introduced by noble metal nanoparticles. Indeed, the carrier trapping, defect state and short paths [12], [14], [17] introduced by metallic nanoparticles can be more devastating in the low-mobility ultrathin polymer device structure. Introducing a spacer layer into thin PLED structures without significantly increasing the device resistance or complicating the PLED fabrication process is also a challenge. Chen et al., who have successfully validated the possibility of SP enhancement in PLED

structures, applied a special low temperature pulsed laser anode deposition method to embed silver nanoparticles in a gallium-doped zinc oxide anode layer prior to polymer spin-coating [26]. Besides the stringent requirements on the anode deposition process, a very modest enhancement factor of about 2 was achieved, likely due to the large spatial separation between the SP mode and the exciton formation region in the polymer film [26]. Meanwhile, colloidal metallic nanoparticles allowing facile solution processing were used to achieve SP enhancement on small molecule-based OLEDs by electrostatic absorption into Au nanoparticle layers [19] or through Au nanoparticles blending into a hole-injecting polymer layer [20]. Comparison between their results also confirms that high nanoparticle densities can be significantly beneficial for achieving high SP enhancement [14].

In this chapter, we describe a simple all solution-processed SP-enhanced PLED structure where we can observe a phenomenal 19-fold luminance enhancement and a 51-fold efficiency enhancement factors by using solution synthesized colloidal silver (Ag) nanoparticles encapsulated with a long oleylamine ligand. Compared with gold colloidal nanoparticles, silver nanoparticles offer much higher Q factors, resulting in high fluorescence enhancement due to their lower Joule loss [11], [17], [27], [28]. In contrast with evaporation-formed nanoparticles having bare surfaces that can impact device current flow significantly and thus limit the nanoparticle incorporation density in LEDs, the long oleylamine capping group around these colloidal Ag nanoparticles forms a natural spacer layer around each individual particle, preventing significant carrier trapping and exciton dissociation on the metallic nanoparticles. Large solubility of oleylamine capped Ag nanoparticle in organic solvent enables direct spin-coating of the Ag nanoparticles layer on top of polymer film through the use of orthogonal

solvent. The nanoparticle density can be further adjusted by changing their solution concentration to achieve optimal Ag nanoparticles incorporation. Time resolved photoluminescence (TRPL) measurements confirm the reduced exciton lifetimes following Ag nanoparticles incorporation. We assign the phenomenal enhancement effect seen in our hybrid PLED structure to a large localized SP mode density, close exciton-SP distance, as well as suppressed of cathode quenching in this unique device configuration.

## 6.2 Experimental Method and Device Structure

The silver nanoparticles are synthesized according to the method reported by Hiramatsu et al. [29]. First, 25 mg silver acetate (Ag (OAc)) (Sigma-Aldrich) is dissolved in 1.0 g oleylamine (Sigma-Aldrich) and then the solution is injected quickly into 25 ml refluxing toluene. After 8 hours reaction, the Ag nanoparticles are then collected by methanol precipitation and washed twice with hexane. The Ag nanoparticle solution is finally filtered using 0.2 $\mu$ m syringe filter and dried in fume hood to measure the net mass of nanoparticles obtained, and later re-dissolved in hexane at different concentrations.

The Ag NP-enhanced PLED structure consists of ITO/PEDOT:PSS (30 $\pm$ 15nm)/F8BT:TFB (90 $\pm$ 15nm)/Ag nanoparticles/Al (150 $\pm$ 15nm). The solvent used for each layer: water (PEDOT:PSS), toluene (polymer blend) and hexane (Ag nanoparticles) forming an orthogonal system, to preserve a high-quality multilayer structure during the subsequent spin-coating steps. To prepare the device, the pre-patterned ITO substrate ( $R_s=15-25$  ohms, Delta Technologies) is sequentially cleaned in acetone and isopropanol ultrasonic baths each for 15 min. A hole-injection layer of PEDOT:PSS (CLEVIOS<sup>TM</sup> P VP Al 4083) is spin-coated on top of the ITO substrate

at 3000 rpm for 90 seconds twice to form a uniform layer, then annealed at 135°C for 30 minutes in air. The layer of polymer blend is spin-coated atop the PEDOT:PSS film from toluene solutions of TFB:F8BT (1:1) (12mg/ml wt concentration) (American Dye Source, Inc.). Subsequently, the Ag nanoparticles are spin-coated directly atop the polymer layer from their hexane solution. Different Ag nanoparticle concentrations (1, 3, 5 and 7mg/ml) are used to investigate the influence of the Ag nanoparticles density on device performance. All the solutions used in the fabrication procedure are filtered with 0.2µm syringe filter before spin-coating. The control samples labeled "Normal PLED", "TiO<sub>2</sub> PLED" and "Flat Ag PLED" are prepared following the same procedure except that the Ag nanoparticles layer is not included ("Normal PLED"), is substituted by a TiO<sub>2</sub> nanoparticle (d = 20nm, Dyesol) layer spin-coated from an ethanol solution ("TiO<sub>2</sub> PLED"), or substituted by a 4 nm-thick silver film deposited by e-beam evaporation ("Flat Ag PLED"). Finally, a 150 nm-thick Al cathode is deposited for all devices through a shadow mask by e-beam evaporation at a rate of 1 Å•s<sup>-1</sup>. The dimensions of the devices are 1mm × 5mm.

Diffuse reflectance absorption of these devices is recorded on a Perkin Elmer Lambda 35 UV-VIS Spectrophotometer to measure the absorption peak of the Ag nanoparticles sandwiched between polymer blend and Al films. Steady-state photoluminescence and electroluminescence spectra are recorded using a Jobin-Yvon iHR320 triple-grating spectrometer equipped with a Synapse silicon CCD array. A 337nm UV laser (VSL-337ND-S) is used for photoluminescence excitation, and a Keithley 236 source-measure unit is used as the electroluminescence power source. A computer-interfaced Newport power meter (818-SL/CM silicon detector) and a Keithley 236 source-measure unit, combined with a 2 inch integrating sphere form the

luminance-current-voltage measurement system. TEM images are obtained using a JEM 2010F instrument at an acceleration voltage of 200 keV. SEM images are obtained using a JSM-7400F field-emission SEM instrument operating at an acceleration voltage of 3 kV. Tapping mode AFM images are obtained on a Dimension 3100V (Digital Instruments). For time-resolved photoluminescence (TRPL) measurements, excitation at 400nm excitation is achieved by frequency doubling a Mira-900 laser. The laser pulses are approximately 150 fs in duration and emitted at a repetition rate of 80 MHz. A pulse picker is used to reduce the repetition rate for sample excitation to 151 kHz.. The fluorescence signal is detected using a Perkin-Elmer avalanche photodiode with a PicoHarp time correlated single photon counting system. The spectral bandwidth of the system is 20 nm and the temporal resolution is 300 ps. The time-resolved photoluminescence data are fitted using the FluoFit analysis software from PicoQuant.

### **6.3 Silver Nanoparticle-Enhanced PLED**

Figure 6-1(a) gives the PLED device architecture indicating the Ag nanoparticle layer deposited directly atop the polymer film on the cathode side. Given the band alignment of the device structure shown in Figure 6-1(b), the hole injection barrier from the ITO side is lower than the electron injection barrier from Al to F8BT, resulting in a hole dominated current in this simple polymer LED structure and therefore behaving similarly to a cathode exciton distribution [30]. As such, the Ag nanoparticle layer's location on the cathode side can not only reduce the separation between SP mode and electron-generated exciton region to insure a strong coupling, but it also alleviates Al cathode quenching by preventing the exciton coupling with the cathode SPP mode. Figure 6-1(c) shows the TEM image of the Ag nanoparticles

encapsulated with oleylamine and synthesized in toluene solution. The oleylamine capping group with a molecular length of  $\sim 2.3$  nm [31] offers Ag nanoparticles with a large solubility in organic solvents. For water soluble metal nanoparticles, the hydrophobic surface of the polymer film prevents the formation of a complete nanoparticle coverage due to the de-wetting of aqueous solution on the polymer film surface [32]. By using organic solution, the SEM image in Figure 6-1(d) shows a uniform Ag nanoparticles coverage atop the polymer layer with a much higher nanoparticle density than scattered nanoparticles formed by slow vacuum deposition method [17], [18].

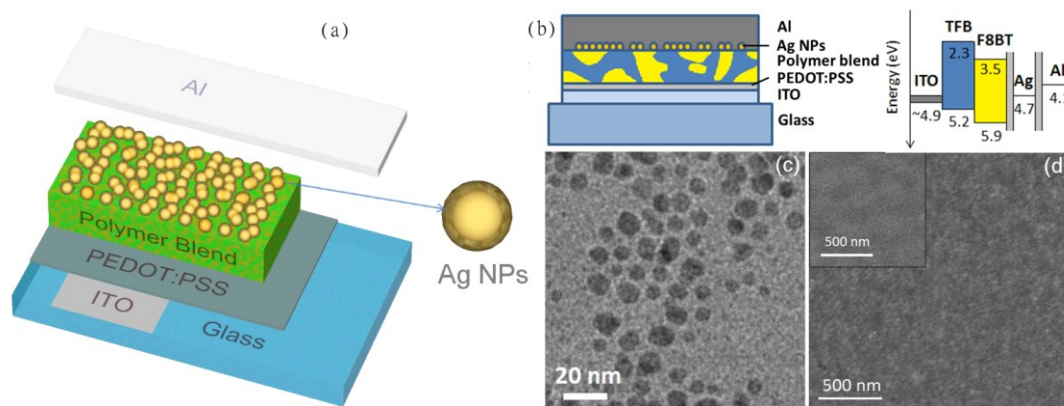


Figure 6-1: Surface plasmon-enhanced polymer LED structure. (a) Schematic of the Ag NP-enhanced PLED device architecture. (b) Energy band diagram of the device structure. (c) TEM image of individual Ag nanoparticles. (d) SEM image of the uniform Ag nanoparticle layer on top of the polymer film. The inset shows the pristine polymer film where the polymer blend phase domain structure can be observed. [33], [34]

In Figure 6-2, the diffused reflectance absorptions from the Ag nanoparticles in the device structures demonstrate that by simply increase the concentration of Ag

nanoparticle solution used for spin-coating, the density of Ag nanoparticles incorporated in the device structure can be increased significantly. Meanwhile, it also shows that the resonance peak of the Ag nanoparticle film is significantly red-shifted compared with the solution, which is consistent with the dipole coupling between neighboring nanoparticles in the densely packed nanoparticle films [35].

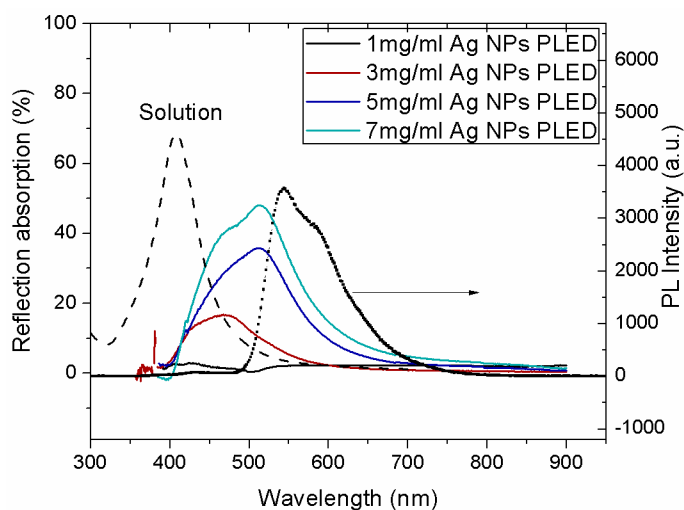


Figure 6-2: Diffused reflectance absorption of colloidal NPs in the device structure and photoluminescence of the F8BT polymer. The dotted line shows the Ag nanoparticles' resonance peak in solution. The solid lines are the diffused reflectance absorptions of the Ag nanoparticles spin-coated from different concentrations of hexane solutions and sandwiched between polymer and Al films. The dotted line shows the photoluminescence spectrum for the F8BT polymer. [34]

To demonstrate the Ag nanoparticle enhancement effect, the LED performance of a group of control devices so-called "Normal PLED", "Flat Ag PLED", "TiO<sub>2</sub> NPs PLED" and "Ag NPs PLED" are compared in Figure 6-3. The "Flat Ag PLED" has a flat 4 nm-thick Ag film evaporated between polymer and Al cathode. With the high

work-function of Ag shown in Figure 6-1(b), the thin Ag film increases the electron injection barrier by 0.6 eV, resulting in a 75% reduction of the current level and a 40% reduction of the overall current efficiency as seen in Figure 6-3 (a) and (b) respectively. Clearly, the PLED performance is significantly impacted with the flat Ag film participating in the current flow and causing electron trapping. In contrast, the current level in the "Ag NPs PLED" is only reduced by 30% compared with the "Normal PLED". However, the "Ag NPs PLED" emission is still 9.5 times stronger than the "Normal PLED", resulting in a 15-fold current-efficiency enhancement at 14V. The current reduction significantly smaller than the luminescence enhancement for the "Ag NPs PLED" indicate that the oleylamine capping layer largely prevents the Ag nanoparticles from causing the severe electron trapping and exciton dissociation such as in "Flat Ag PLED". Meanwhile, unlike the SPP mode in Ag film which results in energy loss, the localized SP mode in Ag nanoparticles can efficiently scatter the coupled energy into photon emission [11]. For the "TiO<sub>2</sub> NPs PLED" control sample, the TiO<sub>2</sub> interlayer creates a rough surface morphology at the polymer Al interface which enhances inhomogeneous local electrical fields and current flow through these hot spot [32], causing the increased current and luminance in "TiO<sub>2</sub> NPs PLED". But the enhancement on luminescence and device efficiency seen with TiO<sub>2</sub> nanoparticles remains significantly smaller than for the Ag nanoparticles in the "Ag NPs PLEDs". The different behaviors between "Ag NPs PLED" and "TiO<sub>2</sub> NPs PLED" here confirm that the enhancement in Ag NPs PLED is not merely due to morphology change at the cathode interface, but closely relates to the Ag nanoparticles' SP mode. Meanwhile, Figure 6-3(c) shows that while the emission intensity is significantly larger, the electroluminescence's spectral shape for the "Ag NPs PLED" remains

nearly identical to the "Normal PLED", and (d) shows the device photos under the same driving voltage.

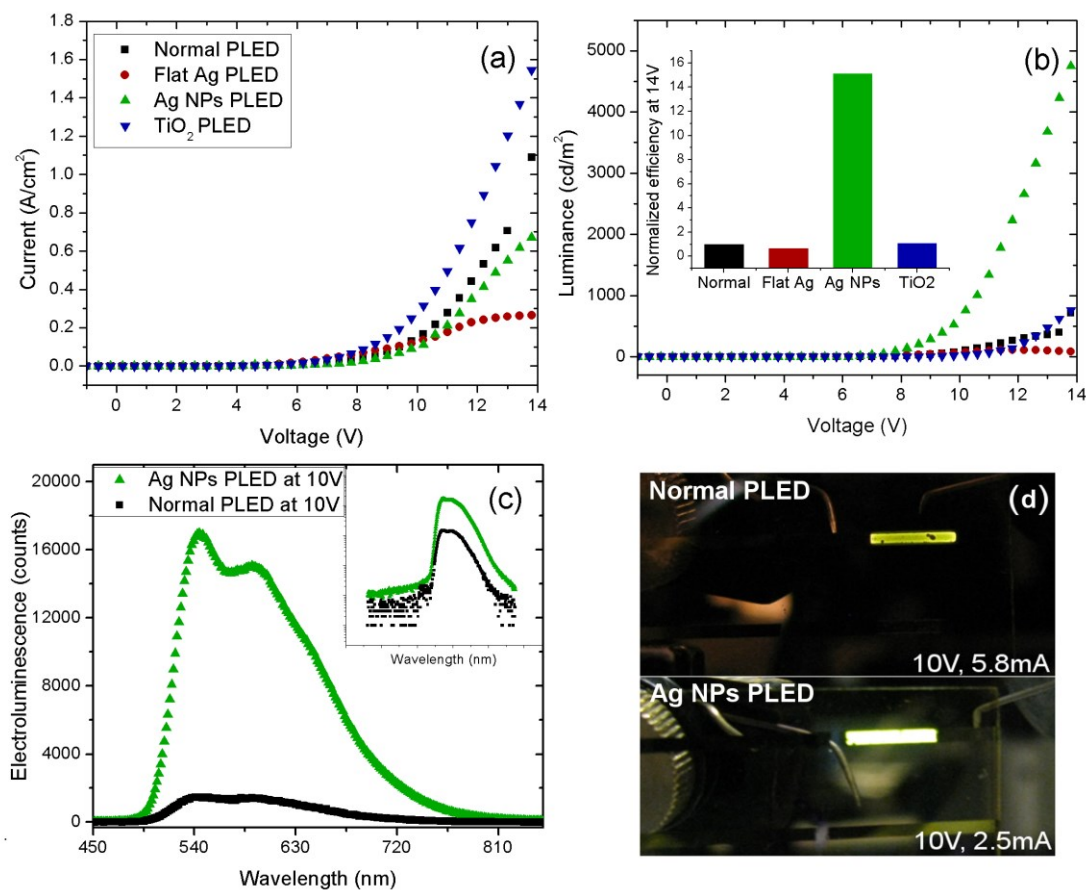


Figure 6-3: Surface plasmon-enhanced polymer LED and control group devices performances comparison. (a) Current-voltage and (b) Luminance-voltage characteristics of the control devices with different materials and structures under the Al cathode. Both TiO<sub>2</sub> and Ag nanoparticles are spin-coated from 5mg/ml solutions. The inset shows the normalized current efficiencies at 14V. (c) Electroluminescence spectra for the Ag NP-enhanced PLED and the Normal PLED at 10V, inset shows the spectra in logarithm scale. (d) Device photos under 10V driving voltage. [33], [34]

The impact of the Ag nanoparticle density on device performances is also interesting. While previous reports have shown that increasing the Ag nanoparticle density can increase the SP enhancement factor on LEDs [18], it is difficult to further increase the Ag nanoparticles density using standard vacuum deposition methods without involving high-temperature annealing and/or causing server carrier trapping [14], [17], [18]. As seen in Figure 6-1(c) and Figure 6-2, the nanoparticle surface density achieved by spin-coating the colloidal Ag nanoparticle solution is much higher than for evaporated nanoparticles and it can be easily adjusted by changing the Ag nanoparticle solution concentration. Figure 6-4 compares the performance of "Ag NPs PLEDs" with different Ag nanoparticle densities. Figure 6-4(a) shows that while Ag concentration increases, the current decreases continuously and undergoes a sharp drop at 7mg/ml devices. The reduced currents are attributed to the low conductivity of the oleylamine capping group, as well as a certain amount of electron- and hole-trapping by the Ag nanoparticle layer. But for the luminance characteristics in Figure 6-4(b) and despite a continuously decreasing current measured for increasing Ag nanoparticle concentrations, the device peak luminance continuously increases up to 3000 cd/m<sup>2</sup> for 5mg/ml Ag NPs device, and then reduces again at 7mg/ml. The resulting current efficiencies given in Figure 6-4(c) show the much higher electroluminescence efficiency for the Ag NPs PLED compared with all the other control samples. For the 7mg/ml Ag NPs device, the device efficiency remains high regardless of the reduced luminescence intensity because of the extended exciton-SP coupling due to the high Ag nanoparticle density. However, the increases Ag nanoparticle concentration begins to affect the current flow through the thicker Ag nanoparticle layer, causing the slight reduction of luminance seen in Figure 6-4(b).

Figure 6-4 (e) summarized the luminance and efficiency peak enhancement factor dependence on Ag nanoparticles concentration.

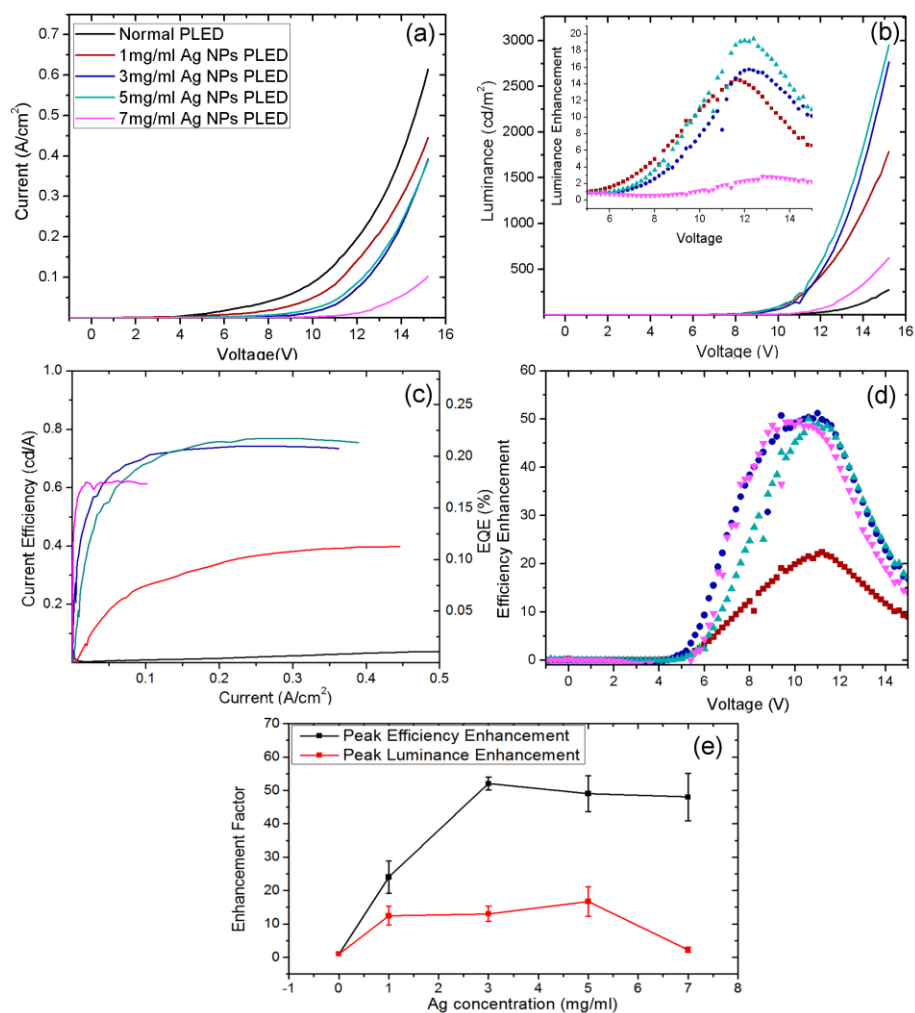


Figure 6-4: Ag nanoparticle density optimization for SP enhanced PLED. (a) Current-voltage characteristics, (b) luminescence-voltage characteristics, (c) efficiency, and (d) luminescence enhancement factor for Ag NPs PLEDs with different densities of Ag nanoparticles incorporated in the device structure and comparison with the normal PLED. (e) summarized Ag NPs concentration dependence of peak enhancement factors. The error bars reflect the standard deviations from 5 devices on one substrate.[34]

AFM imaging further reveals the surface morphology change with increasing Ag nanoparticle density. Figure 6-5(a) shows the pristine polymer film imaging prior to Ag nanoparticle spin-coating, the polymer blend phase separation can be recognized and causes a surface roughness  $R_a$  of 0.88nm. For the 1mg/ml Ag nanoparticle solution, the nanoparticle density is too low to cover the whole surface, forming island area on top of the polymer as seen in Figure 6-5(b). This incomplete surface covering further increases the surface roughness to 1.27nm. However, the film's peak-to-peakbottom  $z$  height of 14.3nm does not exceed twice the Ag nanoparticle diameter, indicating that the Ag nanoparticles predominantly form the monolayer so that no multilayer nanoparticle stack happens at this point. As the Ag concentration increases to 3~5mg/ml, the nanoparticle concentration becomes high enough to form a uniform mono-layer of Ag nanoparticle coverage, where the surface roughness is in fact lower than the 1 mg/ml Ag film due to the formation of a complete Ag nanoparticle coverage. Then, further increasing the Ag nanoparticle concentration to 7mg/ml causes Ag NPs clusters in solution and bi-layered nanoparticles film sections are formed as seen in Figure 6-5 (e), where the surface roughness increases significantly to 1.51 nm and the image  $z$  height reaches 21.1 nm, approximately twice the Ag nanoparticles diameter. Thus, with stacked Ag nanoparticles, the Al cathode is further from the polymer film and the holes and electrons from each side have to hop through the nanoparticle film. The carrier trapping is significantly increased in this situation, explaining the lower current level at 7mg/ml in Figure 6-4(a).

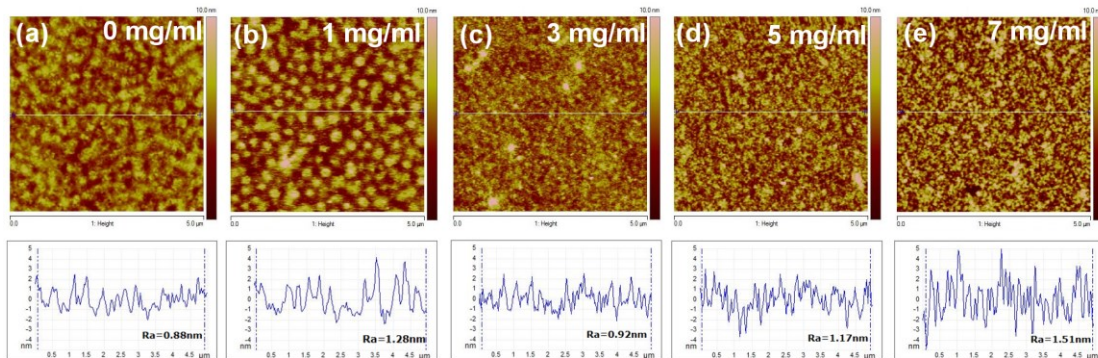


Figure 6-5: AFM images and surface roughness information for Ag nanoparticles spin-coated on polymer film using 0, 1, 3, 5 and 7 mg/ml nanoparticle solutions. [34]

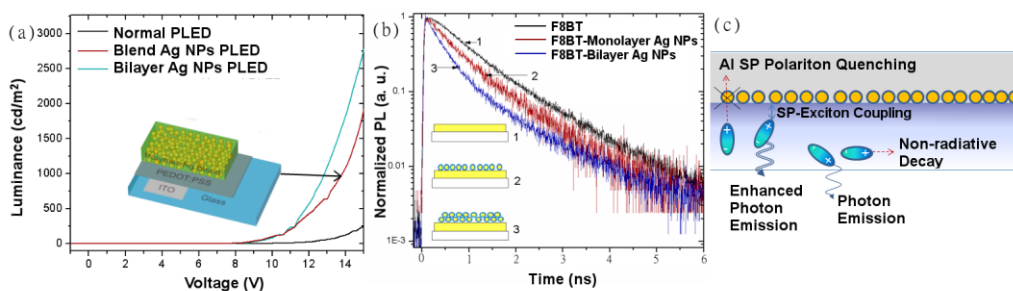


Figure 6-6: (a) Luminance intensity comparison for normal PLED, bilayer Ag NPs PLED and blend Ag NPs PLED. (b) TRPL comparison between a pristine 90nm F8BT film and the same polymer film with monolayer of Ag NPs on top. (c) Demonstration of the SP enhancement mechanism. [33]

Similar enhancement tendencies as the batch in Figure 6-4 are observed from different batches of samples with 3~5mg/ml Ag nanoparticle concentrations. The peak luminance enhancement factor always ranges between 7~19, and the peak efficiency enhancement factor ranges between 10~51 with 3~5mg/ml Ag nanoparticle concentrations. Purcell's theory predictions for a reduced exciton lifetime by coupling

with localized SP mode can be verified using TRPL measurements performed on pure F8BT films with a Ag nanoparticles deposited on top [25]. In Figure 6-6, the decay for the pristine F8BT film demonstrates a mono-exponential decay with an exciton lifetime  $\tau_0$  of  $1.01 \pm 0.02$  ns, falling in the range of previously F8BT exciton lifetime measurements of 0.5~2 ns [36], [37]. Using a 70% quantum yield  $\eta_0$  for F8BT fluorescence [36], the exciton radiative rate is then estimated to be  $k_r = \eta_0/\tau_0 = 0.69 \text{ ns}^{-1}$ . Upon Ag nanoparticle deposition, a bi-exponential decay shows up in the TRPL measurements. Because the F8BT film morphology, and thus the nonradiative loss mechanisms, remain unchanged by the Ag nanoparticle deposition, the appearance of a faster decay component ( $\tau_1$ ) verifies the existence of Purcell enhancement in the presence of the Ag nanoparticles. We measure  $\tau_1$  values of  $0.71 \pm 0.03$  ns and  $0.47 \pm 0.05$  ns when a single and double layer of Ag nanoparticles are placed on top of the F8BT. Using  $k_{sp} = 1/\tau_1$ , the exciton-plasmon coupling rates are estimated to be  $\sim 1.41 \text{ ns}^{-1}$  and  $2.13 \text{ ns}^{-1}$  for samples with one and two layers of Ag nanoparticles, suggesting high Purcell factors  $F_p = k_{sp}/k_r$  of 2.04 and 3.09 respectively. The Purcell surface-plasmon enhancement factor can be generally defined as [27]:

$$F_{SP} = \frac{\eta_{sp}}{\eta_0} = \frac{1+F_p C_{ext}}{1+F_p \eta_0} \quad (6-1)$$

where  $\eta_{sp}$  is the SP-enhanced quantum efficiency and  $C_{ext}$  is the scattering efficiency from localized SP modes into photon emission. As we see, the SP enhancement not only depends on the Purcell factor  $F_p$  but it is also depends on  $\eta_0$  and  $C_{ext}$ . As such, a condition of  $\eta_0 < C_{ext}$  is required to obtain a Purcell surface-plasmon enhancement factor  $F_{SP} > 1$ . Thus the Purcell effect may not contribute to polymer photoluminescence due to the high original F8BT luminescence quantum

yield (70%), but it can show significant enhancement for low efficiency polymer electroluminescence. In fact, many non-radiative exciton decay paths can dominate the electroluminescence process, including electron trap-assistant non-radiative recombination [30], free carrier absorption [38] and cathode metal quenching [21], [22], which are of little consequences in photoluminescence processes. The high enhancement factor observed here in electroluminescence is therefore a result of efficient exciton-SP coupling that competes and dominates over these other non-radiative recombination channels for electroluminescence measurements. This result shows that the surface-plasmon mode can effectively overcome some inherent non-radiative recombination channels in the electroluminescence process and act as a facile method to improve low-cost PLED performances. There is still large space left for colloidal metal nanoparticle size optimization [27] and spacer layer synthesis to further improving polymer-based LEDs.

#### **6.4 Conclusion**

In summary, we demonstrate a surface-plasmon enhanced PLED fabricated using an all solution-based fabrication process. A film of colloidal silver nanoparticles encapsulated with oleylamine is used as the localized surface-plasmon source, which significantly increases PLED luminance (up to 19-fold) and efficiency (up to 51-fold). Here, the oleylamine capping group works as an individual spacer layer to prevent exciton dissociation and significant carrier trapping in the Ag nanoparticles. By placing the Ag nanoparticles directly atop the polymer film on the cathode side, the exciton-plasmon coupling is maximized and the cathode quenching is alleviated. It is seen that high Ag nanoparticle densities lead to higher enhancement factor due to a

higher exciton-plasmon coupling rate. Optimized Ag nanoparticle densities incorporated between the active polymer film and the cathode allow balancing the SP enhancement and the reduced current injection to achieve luminance enhancement factors up-to 19-fold and efficiency enhancement factors up-to 51-fold using only an additional spin-coating. These results suggest that more advanced colloidal Ag nanoparticle design and synthesis offers a tremendous potential for further boosting PLED performances. The facile and low-cost solution processibility offered with this approach could also be easily adapted to other PLED structures for large-scale fabrication of high-performance PLEDs.

## REFERENCES

- [1] K. T. Kamtekar, A. P. Monkman, and M. R. Bryce, "Recent advances in white organic light-emitting materials and devices (WOLEDs).," *Adv. Mater.*, vol. 22, no. 5, pp. 572–82, Feb. 2010.
- [2] S. A. Jenekhe, "Polymer semiconductors: a fast mover with a bright spark.," *Nat. Mater.*, vol. 7, no. 5, pp. 354–5, May 2008.
- [3] X. Gong, S. Wang, D. Moses, G. C. Bazan, and a. J. Heeger, "Multilayer Polymer Light-Emitting Diodes: White-Light Emission with High Efficiency," *Adv. Mater.*, vol. 17, no. 17, pp. 2053–2058, 2005.
- [4] Y. Zhang, F. Huang, Y. Chi, and A. K.-Y. Jen, "Highly Efficient White Polymer Light-Emitting Diodes Based on Nanometer-Scale Control of the Electron Injection Layer Morphology through Solvent Processing," *Adv. Mater.*, vol. 20, no. 8, pp. 1565–1570, Apr. 2008.
- [5] D. Kabra, L. P. Lu, M. H. Song, H. J. Snaith, and R. H. Friend, "Efficient single-layer polymer light-emitting diodes.," *Adv. Mater.*, vol. 22, no. 29, pp. 3194–8, Aug. 2010.
- [6] D. Kabra, M. H. Song, B. Wenger, R. H. Friend, and H. J. Snaith, "High Efficiency Composite Metal Oxide-Polymer Electroluminescent Devices: A Morphological and Material Based Investigation," *Adv. Mater.*, vol. 20, no. 18, pp. 3447–3452, 2008.
- [7] K. A. Willets and R. P. Van Duyne, "Localized surface plasmon resonance spectroscopy and sensing.," *Annu. Rev. Phys. Chem.*, vol. 58, pp. 267–97, Jan. 2007.
- [8] A. Campion and P. Kambhampati, "Surface-enhanced Raman scattering," *Chem. Soc. Rev.*, vol. 27, no. 4, p. 241, 1998.
- [9] S. Pillai, K. R. Catchpole, T. Trupke, and M. A. Green, "Surface plasmon enhanced silicon solar cells," *J. Appl. Phys.*, vol. 101, no. 9, p. 093105, May 2007.

- [10] C.-C. Chang, Y. D. Sharma, Y.-S. Kim, J. A. Bur, R. V. Sheno, S. Krishna, D. Huang, and S.-Y. Lin, "A surface plasmon enhanced infrared photodetector based on InAs quantum dots," *Nano Lett.*, vol. 10, no. 5, pp. 1704–9, May 2010.
- [11] K. Okamoto, I. Niki, A. Shvarts, Y. Narukawa, T. Mukai, and A. Scherer, "Surface-plasmon-enhanced light emitters based on InGaN quantum wells," *Nat. Mater.*, vol. 3, no. 9, pp. 601–5, Sep. 2004.
- [12] M.-K. Kwon, J.-Y. Kim, B.-H. Kim, I.-K. Park, C.-Y. Cho, C. C. Byeon, and S.-J. Park, "Surface-Plasmon-Enhanced Light-Emitting Diodes," *Adv. Mater.*, vol. 20, no. 7, pp. 1253–1257, Apr. 2008.
- [13] D.-M. Yeh, C.-F. Huang, C.-Y. Chen, Y.-C. Lu, and C. C. Yang, "Surface plasmon coupling effect in an InGaN/GaN single-quantum-well light-emitting diode," *Appl. Phys. Lett.*, vol. 91, no. 17, p. 171103, 2007.
- [14] C.-Y. Cho, M.-K. Kwon, S.-J. Lee, S.-H. Han, J.-W. Kang, S.-E. Kang, D.-Y. Lee, and S.-J. Park, "Surface plasmon-enhanced light-emitting diodes using silver nanoparticles embedded in p-GaN," *Nanotechnology*, vol. 21, no. 20, p. 205201, May 2010.
- [15] S. Pillai, K. R. Catchpole, T. Trupke, G. Zhang, J. Zhao, and M. A. Green, "Enhanced emission from Si-based light-emitting diodes using surface plasmons," *Appl. Phys. Lett.*, vol. 88, no. 16, p. 161102, 2006.
- [16] B.-H. Kim, C. Cho, J. Mun, M. Kwon, T.-Y. Park, J. S. Kim, C. C. Byeon, J. Lee, and S. Park, "Enhancement of the External Quantum Efficiency of a Silicon Quantum Dot Light-Emitting Diode by Localized Surface Plasmons," *Adv. Mater.*, vol. 20, no. 16, pp. 3100–3104, Aug. 2008.
- [17] K. Y. Yang, K. C. Choi, and C. W. Ahn, "Surface plasmon-enhanced spontaneous emission rate in an organic light-emitting device structure: Cathode structure for plasmonic application," *Appl. Phys. Lett.*, vol. 94, no. 17, p. 173301, 2009.
- [18] A. Kumar, R. Srivastava, P. Tyagi, D. S. Mehta, and M. N. Kamalasanan, "Efficiency enhancement of organic light emitting diode via surface energy transfer between exciton and surface plasmon," *Org. Electron.*, vol. 13, no. 1, pp. 159–165, Jan. 2012.
- [19] A. Fujiki, T. Uemura, N. Zettsu, M. Akai-Kasaya, A. Saito, and Y. Kuwahara, "Enhanced fluorescence by surface plasmon coupling of Au nanoparticles in an

- organic electroluminescence diode,” *Appl. Phys. Lett.*, vol. 96, no. 4, p. 043307, 2010.
- [20] Y. Xiao, J. P. Yang, P. P. Cheng, J. J. Zhu, Z. Q. Xu, Y. H. Deng, S. T. Lee, Y. Q. Li, and J. X. Tang, “Surface plasmon-enhanced electroluminescence in organic light-emitting diodes incorporating Au nanoparticles,” *Appl. Phys. Lett.*, vol. 100, no. 1, p. 013308, 2012.
- [21] H. Becker, S. Burns, and R. Friend, “Effect of metal films on the photoluminescence and electroluminescence of conjugated polymers,” *Phys. Rev. B*, vol. 56, no. 4, pp. 1893–1905, Jul. 1997.
- [22] V. Choong, Y. Park, Y. Gao, T. Wehrmeister, K. Müllen, B. R. Hsieh, and C. W. Tang, “Dramatic photoluminescence quenching of phenylene vinylene oligomer thin films upon submonolayer Ca deposition,” *Appl. Phys. Lett.*, vol. 69, no. 10, p. 1492, Sep. 1996.
- [23] M. Kuttge, E. Vesseur, A. Koenderink, H. Lezec, H. Atwater, F. García de Abajo, and A. Polman, “Local density of states, spectrum, and far-field interference of surface plasmon polaritons probed by cathodoluminescence,” *Phys. Rev. B*, vol. 79, no. 11, p. 113405, Mar. 2009.
- [24] J. Nelayah, M. Kociak, O. Stéphan, F. J. García de Abajo, M. Tencé, L. Henrard, D. Taverna, I. Pastoriza-Santos, L. M. Liz-Marzán, and C. Colliex, “Mapping surface plasmons on a single metallic nanoparticle,” *Nat. Phys.*, vol. 3, no. 5, pp. 348–353, Apr. 2007.
- [25] E. Purcell, “Spontaneous emission probabilities at radio frequencies,” *Phys. Rev.*, vol. 69, p. 681, 1946.
- [26] S.-H. Chen and J.-Y. Jhong, “Enhanced luminescence efficiency by surface plasmon coupling of Ag nanoparticles in a polymer light-emitting diode,” *Opt. Express*, vol. 19, no. 18, pp. 16843–50, Aug. 2011.
- [27] G. Sun, J. Khurgin, and R. Soref, “Plasmonic light-emission enhancement with isolated metal nanoparticles and their coupled arrays,” *JOSA B*, vol. 25, no. 10, pp. 1748–1755, 2008.
- [28] T. Neal, K. Okamoto, and A. Scherer, “Surface plasmon enhanced emission from dye doped polymer layers,” *Opt. Express*, vol. 13, no. 14, pp. 5522–7, Jul. 2005.

- [29] H. Hiramatsu and F. E. Osterloh, "A Simple Large-Scale Synthesis of Nearly Monodisperse Gold and Silver Nanoparticles with Adjustable Sizes and with Exchangeable Surfactants," *Chem. Mater.*, vol. 16, no. 13, pp. 2509–2511, Jun. 2004.
- [30] M. Kuik, L. J. a. Koster, a. G. Dijkstra, G. a. H. Wetzelaer, and P. W. M. Blom, "Non-radiative recombination losses in polymer light-emitting diodes," *Org. Electron.*, vol. 13, no. 6, pp. 969–974, Mar. 2012.
- [31] M. Chen, Y.-G. Feng, X. Wang, T.-C. Li, J.-Y. Zhang, and D.-J. Qian, "Silver nanoparticles capped by oleylamine: formation, growth, and self-organization.," *Langmuir*, vol. 23, no. 10, pp. 5296–304, May 2007.
- [32] B. Riedel, J. Hauss, M. Aichholz, A. Gall, U. Lemmer, and M. Gerken, "Polymer light emitting diodes containing nanoparticle clusters for improved efficiency," *Org. Electron.*, vol. 11, no. 7, pp. 1172–1175, Jul. 2010.
- [33] X. Ma, J. A. Benavides, C. R. Haughn, F. Xu, M. F. Doty, and S. G. Cloutier, "Colloidal Ag Nanoparticles Enhanced Polymer-LEDs by Exciton-Surface Plasmon Coupling," in *Solid-State and Organic Lighting*, 2013, p. DT2E.5.
- [34] X. Ma, J. Benavides, C. R. Haughn, F. Xu, M. F. Doty, and S. G. Cloutier, "High polymer-LEDs enhancement by exciton–plasmon coupling using encapsulated metallic nanoparticles," *Org. Electron.*, vol. 14, no. 7, pp. 1916–1923, Apr. 2013.
- [35] M. a Mahmoud, A. J. Poncheri, R. L. Phillips, and M. a El-Sayed, "Plasmonic field enhancement of the exciton-exciton annihilation process in a poly(p-phenyleneethynylene) fluorescent polymer by Ag nanocubes.," *J. Am. Chem. Soc.*, vol. 132, no. 8, pp. 2633–41, Mar. 2010.
- [36] J.-S. Kim, L. Lu, P. Sreearunothai, A. Seeley, K.-H. Yim, A. Petrozza, C. E. Murphy, D. Beljonne, J. Cornil, and R. H. Friend, "Optoelectronic and charge transport properties at organic-organic semiconductor interfaces: comparison between polyfluorene-based polymer blend and copolymer.," *J. Am. Chem. Soc.*, vol. 130, no. 39, pp. 13120–31, Oct. 2008.
- [37] S. Cook, H. Ohkita, J. R. Durrant, Y. Kim, J. J. Benson-Smith, J. Nelson, and D. D. C. Bradley, "Singlet exciton transfer and fullerene triplet formation in polymer-fullerene blend films," *Appl. Phys. Lett.*, vol. 89, no. 10, p. 101128, Sep. 2006.

- [38] A. R. Brown, K. Pichler, N. C. Greenham, D. D. C. Bradley, R. H. Friend, and A. B. Holmes, "Optical spectroscopy of triplet excitons and charged excitations in poly(p-phenylenevinylene) light-emitting diodes," *Chem. Phys. Lett.*, vol. 210, no. 1–3, pp. 61–66, Jul. 1993.

## Chapter 7

### CONCLUSIONS AND FUTURE PROSPECTS

Solution processable polymer materials and hybrid light emitting diodes were recently studied due to many key advantages over conventional inorganic LEDs [1]–[4]. They can potentially hold the key for next step development of light emitting diode and applications for displays and light sources. Solution process significantly reduces the fabrication cost by using spin coating from material solution instead of crystal growth under high temperature and high vacuum conditions for conventional inorganic material. The solution processability also makes it possible to fabricate large-area low-cost electronic devices by inkjet printing. Polymer and hybrid material-based devices can also be flexible and compatible with different substrates. For polymer/quantum dot hybrid LEDs, quantum dots offer narrow electroluminescence spectra, leading to more saturated colors from the device [5]. Meanwhile, quantum dot device emission wavelength can be tuned by tailoring the quantum dot size without changing any materials or processes involved in the device structure.

Even with these key advantages, the performance of these novel solution processable material based devices is still limited by their low efficiency, low brightness and lower stability compared with their inorganic counterparts.

In the solution based fabrication process, a key component is the solvent used to mix the active material solution. While the solvent will evaporate during spin-coating, the evaporation rate and solvent property affect the polymer molecular

morphology and packing during the spin coating, and change the final device performance significantly for both polymer blend system and mono-polymer device[6]. In polymer blend system, the phase separation scale is controlled by the solvent evaporation rate resulting in large phase domain size with slowly-evaporating solvents and small domains for fast evaporating solvents. The domain size in polymer thin film further dictates the exciton's behavior in the device. The domain interface can break excitons into delocalized electron and holes. This is why a fast evaporating solvent producing small domains (i.e. rich domain interface for excitons to break) is preferred for solar cell applications. Meanwhile, a slowly-evaporating solvent producing large domains (i.e. less domain interface) is preferred for light emitting application. Besides the phase separation scale, the polymer chain alignment is also determined by solvent properties. Using a mono-polymer device, this dissertation revealed that an aromatic solvent in which the polymer conjugated backbone is more dissolvable can offer devices with better crystalline domains, which yields good charge transport and strong fluorescence [6].

Meanwhile, multilayer structure can be enabled in simple spin coating process by carefully choosing orthogonal solvent system. Indeed, we achieved a true bi-layer device structure using toluene-based polymer layer with hexane-based for quantum dot layer. The hexane solution does not dissolve the polymer layer underneath, but causes swelling of polymer chain at the interface. The swelled polymer chain acts as a good passivation medium to reduce the density of surface defect states created during ligand exchange. Therefore, performing ligand exchange on top of polymer layer creates a quantum dot thin film with high conductive properties and maintains high fluorescence efficiency due to the passivation of surface states.

For colloidal quantum dots, the capping ligand is always used to keep the quantum dots stable and reduce the surface trapping centers. However, different ligand molecules yield quantum dot thin films with different optical and electrical properties [7], [8]. This dissertation studied two commonly used dithiol molecules: ethanedithiol and benzenedithiol on their different impacts on the quantum dot thin film electronic properties. Despite of similar film morphologies achieved with these two dithiol exchange processes, the resulting film conductivities and carrier mobilities are dramatically different. The conjugated benzene ring in benzenedithiol offers the thin film higher electron transporting mobility and a relatively lower hole mobility compared with ethanedithiol. Meanwhile, the doping density is much lower for benzenedithiol treated quantum dot thin film, making them suitable for light emitting device which requires high quality low doping materials that can reduce exciton quenching through mid-bandgap states and/or Auger recombination center in highly doped materials.

In the last part of this dissertation, the potential of using surface plasmons to enhance electroluminescence device performance is demonstrated. By incorporating colloidal silver nanoparticles resonance with F8BT polymer fluorescence, the device performance is boosted dramatically due to the Purcell effect associated with surface plasmon coupling. An optimal incorporation density is achieved to balance the enhancement with charge trapping in the silver nanoparticles.

Organic LEDs for the visible are already positioned to occupy the commercial market for displays in digital devices. Their EQEs can reach 6.3% with stable performances under encapsulation[9], [10]. However, for wavelengths above 1 $\mu$ m, there is a lack of high quantum yield organic molecules or polymer dyes, resulting in

the best reported efficiency only of  $<0.3\%$  [11]. Thus the development of near-IR quantum dots is of significant interest to help fill this vacancy. Compared with the more advanced visible QD-LEDs which have reached EQEs as high as 18% [12], near-IR QD-LEDs are still at an early developmental stage. Near-IR LEDs have a wide range of application including remote controls, night vision displays [5], security systems as well as biosensing & bioimaging platforms [13]. So far, most researchers have focused on material innovation and/or changing the shape and shell of the nanoparticles, but the work on revealing the fundamental physical and electrical property of quantum dot devices and their working mechanisms has only started to attract significant interest. This dissertation first discussed the previous literature the possibilities of applying ligand exchange to improve the near-IR quantum dot thin film transport properties for light emitting application. Performing the ligand exchange on a conjugated polymer layer significantly reduced the deep trap surface state formed by the dangling bonds on quantum dot surface, thus resulting in quantum dot thin film with good transport properties while maintaining a high quantum yields.

The physics and property of novel organic, polymer and quantum dot materials remains unknown, therefore, their device design mostly relies on trial and error processes which are inefficient and involve a lot of labor work. One example of this lack of understanding on device physics model is the debate on the origin of quantum dot electroluminescence in LED structures between direct charge injection and energy transfer from organic carrier transporting layer. This lack of a good device physics model would become the biggest obstacle for further device development and it has already started to raise a lot of attention recently. In the following section, I will discuss several strategies aiming to improve our quantum dot LED performance.

Novel material for device structure innovation: The low electron mobility of quantum dot thin film still limits the use of it as the electron injection layer. Recently, colloidal ZnO and TiO<sub>2</sub> nanoparticle were demonstrated to be good electron-transporting materials for solution processed light emitting devices[12], [14], [15]. Incorporating metallic nanoparticle layers can increase electron injection efficiencies more efficiently than organic layer or cross-linked quantum dot layer. Meanwhile, besides the dithiol molecule used in this dissertation to cross-link quantum dot for device application, other ligand exchange molecules or methods worth further investigation to improve the carrier transport in quantum dot thin films while passivate the surface states.

Deep analysis of band alignment in quantum dot LED structures: An accurate band diagram of the device structure is the key to understand, design and optimize the device property and its performance. Most of the device band diagrams are drawn based on the measurement results from individual component respectively. However, it is suggested from recent study that the QD conduction and valence band can shift upon mixing with polymer matrix[16]. Thus, it is critical to understand quantum dot band structure especially at the quantum dot/organic interface.

Applying surface plasmon coupling to enhance device performance: Localized surface plasmon in metal nanostructure has been shown to enhance quantum dot photoluminescence. This dissertation also demonstrated the significant enhancement of PLEDs' electroluminescence by incorporation silver nanoparticles. In fact, colloidal nanoparticles have already been used on visible quantum dot LED and enhanced the EL intensity by 71% [17]. However, optimized conditions are still not fully

investigated in this field. Meanwhile, it is of interest to see if these mechanisms can be applied to near-IR quantum dot LED.

Exploiting the energy transfer between organic materials and quantum dots: A lot of the quantum dot device structures involve organic material with strong fluorescence. Nevertheless, organic materials remain used mostly as charge transport layers in hybrid optoelectronic device architectures, where their high luminescence efficiency is unexploited. In hybrid quantum dot-based LEDs, high polymer emission residues observed at high driving currents due to the incomplete energy transfer observed between organic material and colloidal quantum dots can significantly alter the color purity of the hybrid LEDs [18]. Therefore, a low quantum yield polymer like poly-TPD is usually chosen to minimize this emission residue [4], [14], [19]. Since both colloidal quantum dots and  $\pi$ -conjugated polymers are strongly luminescent materials, a better understanding and control of the energy transfer between these two material systems is much desired to exploit the full potential that low-cost hybrid heterostructures can offer for light emitting, solar cell and laser applications.

In the last but not the least, device lifetime and stability is an important aspect that determined the application and commercialization of the device: With the development of organic LEDs, their degradation mechanisms become better understood and good encapsulation techniques have been developed. These techniques provide a good platform for quantum dot devices, but a good understanding of quantum dot fluorescence decay and a thorough investigation of device lifetime is still lacking. This step would eventually determine the commercialization and practice application of these novel hybrid material-based devices.

## REFERENCES

- [1] T.-W. Lee, J. Hwang, and S.-Y. Min, "Highly efficient hybrid inorganic-organic light-emitting diodes by using air-stable metal oxides and a thick emitting layer.," *ChemSusChem*, vol. 3, no. 9, pp. 1021–3, Sep. 2010.
- [2] T. Kawase, D. J. Pinner, R. H. Friend, and T. Shimoda, "Grazing emitted light from films of derivative polymer of polyfluorene," *Synth. Met.*, vol. 111–112, pp. 583–586, Jun. 2000.
- [3] T.-W. Lee, O. O. Park, J. Yoon, and J.-J. Kim, "Polymer-Layered Silicate Nanocomposite Light-Emitting Devices," *Adv. Mater.*, vol. 13, no. 3, pp. 211–213, Feb. 2001.
- [4] Z. Tan, F. Zhang, T. Zhu, J. Xu, A. Y. Wang, J. D. Dixon, L. Li, Q. Zhang, S. E. Mohney, and J. Ruzyllo, "Bright and color-saturated emission from blue light-emitting diodes based on solution-processed colloidal nanocrystal quantum dots.," *Nano Lett.*, vol. 7, no. 12, pp. 3803–7, Dec. 2007.
- [5] Y. Shirasaki, G. J. Supran, M. G. Bawendi, and V. Bulović, "Emergence of colloidal quantum-dot light-emitting technologies," *Nat. Photonics*, vol. 7, no. 1, pp. 13–23, Dec. 2012.
- [6] X. Ma, F. Xu, and S. G. Cloutier, "Solvent and Baking Effect on Polymer Morphology and PLED Device Performance," in *Frontiers in Optics / Laser Science 2010*, 2010, p. LMA5.
- [7] X. Ma, F. Xu, and S. G. Cloutier, "Impact of different dithiol treatments on the optoelectronic properties of self-assembled PbS nanocrystalline films ( a ) ( b )," vol. 1, pp. 2–3.
- [8] X. Ma, F. Xu, J. Benavides, and S. G. Cloutier, "High performance hybrid near-infrared LEDs using benzenedithiol cross-linked PbS colloidal nanocrystals," *Org. Electron.*, vol. 13, no. 3, pp. 525–531, Mar. 2012.
- [9] C. Borek, K. Hanson, P. I. Djurovich, M. E. Thompson, K. Aznavour, R. Bau, Y. Sun, S. R. Forrest, J. Brooks, L. Michalski, and J. Brown, "Highly Efficient,

Near-Infrared Electrophosphorescence from a Pt–Metalloporphyrin Complex,” *Angew. Chemie*, vol. 119, no. 7, pp. 1127–1130, Feb. 2007.

- [10] J. R. Sommer, R. T. Farley, K. R. Graham, Y. Yang, J. R. Reynolds, J. Xue, and K. S. Schanze, “Efficient near-infrared polymer and organic light-emitting diodes based on electrophosphorescence from (tetraphenyltetranaphtho[2,3]porphyrin)platinum(II).,” *ACS Appl. Mater. Interfaces*, vol. 1, no. 2, pp. 274–8, Feb. 2009.
- [11] G. Qian, Z. Zhong, M. Luo, D. Yu, Z. Zhang, Z. Y. Wang, and D. Ma, “Simple and Efficient Near-Infrared Organic Chromophores for Light-Emitting Diodes with Single Electroluminescent Emission above 1000 nm,” *Adv. Mater.*, vol. 21, no. 1, pp. 111–116, Jan. 2009.
- [12] B. S. Mashford, M. Stevenson, Z. Popovic, C. Hamilton, Z. Zhou, C. Breen, J. Steckel, V. Bulovic, M. Bawendi, S. Coe-Sullivan, and P. T. Kazlas, “High-efficiency quantum-dot light-emitting devices with enhanced charge injection,” *Nat. Photonics*, vol. 7, no. 5, pp. 407–412, Apr. 2013.
- [13] D. P. Kumar, P. Sharma, S. Brown, G. Walter, S. Santra, and B. Moudgil, “Nanoparticles for bioimaging,” *Adv. Colloid Interface Sci.*, vol. 123, pp. 471–485, 2006.
- [14] L. Qian, Y. Zheng, J. Xue, and P. Holloway, “Stable and efficient quantum-dot light-emitting diodes based on solution-processed multilayer structures,” *Nat. Photonics*, vol. 5, no. September, 2011.
- [15] L. Sun, J. J. Choi, D. Stachnik, A. C. Bartnik, B.-R. Hyun, G. G. Malliaras, T. Hanrath, and F. W. Wise, “Bright infrared quantum-dot light-emitting diodes through inter-dot spacing control,” *Nat. Nanotechnol.*, vol. 7, no. 6, pp. 369–73, Jun. 2012.
- [16] I. H. Campbell and B. K. Crone, “Efficient, visible organic light-emitting diodes utilizing a single polymer layer doped with quantum dots,” *Appl. Phys. Lett.*, vol. 92, no. 4, p. 043303, Jan. 2008.
- [17] T.-H. Kim, K. Cho, E. K. Lee, S. J. Lee, J. Chae, J. W. Kim, D. H. Kim, J. Kwon, G. Amaratunga, S. Y. Lee, B. L. Choi, Y. Kuk, J. M. Kim, and K. Kim, “Full-colour quantum dot displays fabricated by transfer printing,” *Nat. Photonics*, vol. 5, no. 3, pp. 176–182, Feb. 2011.

- [18] S. Coe-Sullivan, W. K. Woo, J. S. Steckel, M. Bawendi, and V. Bulović, “Tuning the performance of hybrid organic/inorganic quantum dot light-emitting devices,” *Org. Electron.*, vol. 4, no. 2–3, pp. 123–130, 2003.
- [19] S. Coe, W. K. Woo, M. G. Bawendi, and V. Bulović, “Electroluminescence from single monolayers of nanocrystals in molecular organic devices,” *Nature*, vol. 420, no. December, pp. 3–6, 2002.

## Appendix A

### CONTRIBUTIONS ASSOCIATED WITH THIS DISSERTATION

#### A.1 Journal Publications

- [1] X. Ma, J. Benavides, C.R. Haughn, F. Xu, M.F. Doty, S.G. Cloutier, High polymer-LEDs enhancement by exciton–plasmon coupling using encapsulated metallic nanoparticles, *Org. Electron.* 14 (2013) 1916–1923.
- [2] S. G. Cloutier, F. Xu, J. Benavides, X. Ma, Interconnected TiO<sub>2</sub> nanowire networks for enhanced PbS/TiO<sub>2</sub> heterojunction solar cells, *J. Nanotechnol.* (2012) 709031–6.
- [3] X. Ma, F. Xu, J. Benavides, S.G. Cloutier, High performance hybrid near-infrared LEDs using benzenedithiol cross-linked PbS colloidal nanocrystals, *Org. Electron.* 13 (2012) 525–531.
- [4] F. Xu, X. Ma, C.R. Haughn, J. Benavides, M.F. Doty, S.G. Cloutier, Efficient exciton funneling in cascaded PbS quantum dot superstructures., *ACS Nano.* 5 (2011) 9950–7.
- [5] F. Xu, X. Ma, L.F. Gerlein, S.G. Cloutier, Designing and building nanowires: directed nanocrystal self-assembly into radically branched and zigzag PbS nanowires., *Nanotechnology.* 22 (2011) 265604.
- [6] N. Sharma, S.J. McKeown, X. Ma, D.J. Pochan, S.G. Cloutier, Structure-Property Correlations in Hybrid Polymer-Nanoparticle Electrospun Fibers and Plasmonic Control over their Dichroic Behavior, in: 2nd Int. Conf. Multifunct. Hybrid Nanomater., Strasbourg, France, 2011: p. B29.
- [7] X. Ma, G.P. Crawford, R.J. Crawford, I. Amimori, S. Žumer, G. Skačej, et al., Nuclear magnetic resonance of pretransitional ordering of liquid crystals in well defined nano-geometries: the utility of the Landau–de Gennes formalism, *Liq. Cryst.* 36 (2009) 1229–1240.
- [8] W. Yin, J. Su, M. Cao, C. Ni, S.G. Cloutier, Z. Huang, et al., In(OH)<sub>3</sub> and In<sub>2</sub>O<sub>3</sub> Micro/Nanostructures: Controllable NaOAc-Assisted Microemulsion Synthesis and Raman Properties, *J. Phys. Chem. C.* 113 (2009) 19493–19499.

## A.2 Conference Publications

- [1] X. Ma, Jaime Benavides, Chelsea Haughn, Fan Xu, Matthew Doty, Sylvain G. Cloutier, Colloidal Ag Nanoparticles Enhanced Polymer-LEDs by Exciton-Surface Plasmon Coupling, Solid State and Organic Lighting, (Optical Society of America, Tucson, AZ, 2013), Paper DT2E.6
- [2] X. Ma, Sylvain G. Cloutier, Hybrid polymer-nanocrystal multilayered architectures for high-performance near-infrared LEDs, International Conference and Exhibition on Lasers, Optics & Photonics, (OMICS group, San Antonio, TX, 2013)
- [3] X. Ma, F. Xu, J. Benavides, and S. G. Cloutier, Hybrid multilayered polymer-nanocrystal heterostructures for high-performance optoelectronic devices, Villa Conference on Optoelectronic Materials and Devices, (Orlando, FL, 2012), Paper F09
- [4] X. Ma, F. Xu, J. Benavides, S.G. Cloutier, Physical Properties of Hybrid Polymer-Nanocrystal Multilayered Architectures for High-Performance Near-Infrared Optoelectronics, in: Energy Mater. Nanotechnol. West, Houston, 2013: p. B13.
- [5] X. Ma, F. Xu, J. Benavides, S.G. Cloutier, Hybrid multilayered polymer-nanocrystal heterostructures for high-performance optoelectronic devices, in: Villa Conf. Optoelectron. Mater. Devices, Orlando, 2012: p. F09.
- [6] X. Ma, F. Xu, J. Benavides, S.G. Cloutier, Hybrid polyfluorene-based nanocomposite superstructures for near-infrared optoelectronics, in: 2011 VCIAN Conf., Las Vegas, 2011: p. Th10.
- [7] F. Xu, J. Benavides, X. Ma, S.G. Cloutier, All solution-based multilayered heterostructures enabling ultra low-cost light-emitting diodes for near-infrared operations, in: Photonics North, Montreal, PQ, 2012: pp. Paper GEN O/P-7-45-3.
- [8] F. Xu, J. Benavides, X. Ma, S.G. Cloutier, Synthesis of mesoporous TiO<sub>2</sub> nanowire film for PbS/TiO<sub>2</sub> heterojunction photovoltaic devices, in: Front. Opt. / Laser Sci., San Jose, CA, 2011: p. FMK6.

- [9] X. Ma, F. Xu, S.G. Cloutier, Impact of different dithiol treatments on the optoelectronic properties of self-assembled PbS nanocrystalline films, in: *Front. Opt. / Laser Sci.* 2011, San Jose, CA, 2011: p. FMK3.
- [10] X. Ma, F. Xu, J. Benavides, S.G. Cloutier, Hybrid Multilayered Heterostructures for High-Performance Near-Infrared LEDs, in: *Front. Opt. / Laser Sci.* 2011, San Jose, CA, 2011: p. FWBB3.
- [11] X. Ma, F. Xu, J. Benavides, S.G. Cloutier, Hybrid Polymer-Nanocrystal Heterostructures for High-Performance Chip-Integrated Near-Infrared LEDs, in: *8th Inter. Conf. Group-IV Photonics*, Ieee, London, UK, 2011: p. P2.16.
- [12] N. Sharma, S.J. McKeown, X. Ma, D.J. Pochan, S.G. Cloutier, Structure-Property Correlations in Hybrid Polymer-Nanoparticle Electrospun Fibers and Plasmonic Control over their Dichroic Behavior, in: *2nd Int. Conf. Multifunct. Hybrid Nanomater.*, Strasbourg, France, 2011: p. B29.
- [13] X. Ma, F. Xu, S.G. Cloutier, Near-Infrared Polymer-based LEDs Using Hybrid Polyfluorene-based Type-II Heterojunctions with PbS Quantum Dots, in: *2nd Int. Conf. Multifunct. Hybrid Nanomater.*, Strasbourg, France, 2011: p. C19.
- [14] X. Ma, F. Xu, J. Benavides, S.G. Cloutier, High-Performance 1550 nm Polymer-based LEDs On Silicon Using Hybrid Polyfluorene-based Type-II Heterojunctions, in: *Front. Opt. / Laser Sci.* 2010, Rochester, NY, 2010: p. FWD2.
- [15] F. Xu, X. Ma, S.G. Cloutier, Efficient Near-infrared Electroluminescence Devices Based On PbS Nanocrystals, in: *Front. Opt. / Laser Sci.* 2010, Rochester, NY, 2010: p. FThAA3.
- [16] X. Ma, F. Xu, S.G. Cloutier, Solvent and Baking Effect on Polymer Morphology and PLED Device Performance, in: *Front. Opt. / Laser Sci.* 2010, Rochester, NY, 2010: p. LMA5.
- [17] X. Ma, F. Xu, S.G. Cloutier, High-Performance 1550 nm Polymer-Based LEDs on Silicon using Hybrid Polyfluorene-Based Type-II Heterojunctions, in: *7th Inter. Conf. Group-IV Photonics*, Ieee, Beijing, China, 2010: p. WA2.